

# **Development and Characterization of Functional Nanocomposites for Thermal and Capacitive Energy Storage Applications**

Thesis Submitted in Partial Fulfillment of the Requirements

for the Award of the Degree of

**DOCTOR OF PHILOSOPHY**

in

**METALLURGICAL AND MATERIALS ENGINEERING**

by

**BALAJI PADYA**

(Roll No. 701625)

Under the supervision of

**Dr. N. Narasaiah**

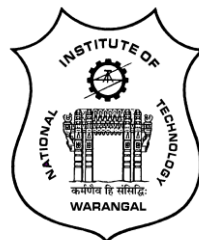
Professor

National Institute of Technology-Warangal,  
Warangal, Telangana State, India

**Dr. P. K. Jain**

Scientist-G

International Advanced Research Centre for  
Powder Metallurgy and New Materials (ARCI)  
Hyderabad, Telangana State, India



**DEPARTMENT OF METALLURGICAL AND MATERIALS ENGINEERING**

**NATIONAL INSTITUTE OF TECHNOLOGY WARANGAL,**

**WARANGAL – 506 004, TELANGANA STATE, INDIA**

**July-2021**

*This Thesis is dedicated to*



**JAWAHAR NAVODAYA VIDYALAYA-WARANGAL**

**DEPARTMENT OF METALLURGICAL AND MATERIALS ENGINEERING**

**NATIONAL INSTITUTE OF TECHNOLOGY**

**WARANGAL – 506 004 (T.S.) INDIA**



**CERTIFICATE**

This is to certify that the work presented in the thesis entitled "***Development and Characterization of Functional Nanocomposites for Thermal and Capacitive Energy Storage Applications***" which is being submitted by **Mr. Balaji Padya (Roll No: 701625)**, is a bonafide work submitted to National Institute of Technology, Warangal in partial fulfillment of the requirements for the award of the degree of **Doctor of Philosophy** in **Metallurgical and Materials Engineering Department**.

To the best of my knowledge, the work incorporated in the thesis has not been submitted to any other university or institute for the award of any other degree or diploma.

**Dr. N. Narasaiah**

Thesis Internal Supervisor

NITW, MMED

**Dr. P. K. Jain**

Thesis External Supervisor

Scientist - G , ARCI

## **Thesis Approval for Ph.D.**

The Thesis entitled "**Development and Characterization of Functional Nanocomposites for Thermal and Capacitive Energy Storage Applications**" by **Mr. Balaji Padya (Roll No: 701625)**, is approved for the degree of Doctor of Philosophy.

Examiners

---

---

---

Supervisor (s)

---

---

---

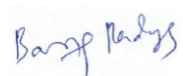
Chairman

---

Date: .....

## **DECLARATION**

This is to certify that the research work presented in the thesis entitled "**Development and Characterization of Functional Nanocomposites for Thermal and Capacitive Energy Storage Applications**" is a bonafide work done by me under the supervision of **Dr. N. Narasaiah**, NITW and **Dr. P.K. Jain**, ARCI and was not submitted elsewhere for the award of any degree. I declare that this written submission represents my ideas in my own words and where others' ideas or words have not been included, I have adequately cited and referenced the original sources. I also declare that I have adhered to all principles of academic honesty and integrity and have not misrepresented or fabricated or falsified any idea/ data/ fact/ source in my submission. I understand that any violation of the above will be a cause for disciplinary action by the Institute and can evoke penal action from the sources which have thus not been properly cited or from whom proper permission has not been taken when needed.



Place: Warangal

**Balaji Padya**

Date: 28-09-2021

(Roll No. 701625)

## **ACKNOWLEDGEMENTS**

I express my deep sense of gratitude to ***Prof. N.V. Ramana Rao***, Director, National Institute of Technology-Warangal, and ***Late Dr. G. Padmanabham***, Former Director ARCI, Hyderabad for permitting me to register at premier institute for higher education, which is institute of national importance.

I wish to express my deep gratitude and heartfelt thanks to my supervisors namely ***Dr. N. Narasaiah*** (Thesis internal supervisor), Professor, MMED, NITW and ***Dr. P.K. Jain*** (Thesis external supervisor) Scientist-G & Head, Centre for Carbon Materials, ARCI, Hyderabad for their excellent guidance, constant encouragement and critical review of my work at every step. Their supervision, advice, guidance as well as encouragement and support were invaluable for me. I could not say enough thank to ***Dr. N. Narasaiah***, who has just been a great mentor in every meaning of the word for giving timely guidance while granting me full freedom to explore new frontiers.

I would like to acknowledge my beloved DSC members: ***Dr. Asit K. Khanra*** (DSC chairman and present HOD of MMED), ***Dr. A. Kumar***, Professor, Dept. Mechanical Engineering (Allied DSC member), ***Dr. B. Srinivasa Rao***, Assistant Professor, MMED and ***Dr. A. K. Pandey***, MMED for critical scientific observation in every research progress meetings and providing constructive suggestions to make my work scientifically sound. Their insightful questions and discussions along the way have helped me a lot over the years. I wish to thank ***Dr. M.K. Mohan***, ***and Dr. C. Vanitha*** (former HOD of MMED), ***Dr. R. Arockia Kumar*** (former faculty advisor) and ***Dr. Sukla Mondol*** (present faculty advisor) and other faculty at NITW for their valuable suggestions, which has been, helped a lot in completing my research.

I would like to extend my thanks to ***Dr. Ravi Kali, Dr. L. Venkatesh, Mr. M. Ramakrishna, Dr. Neha Y Hebalkar, Dr. B.V. Sharada, Dr. Sanjay Dhage, Dr. Rajeev Kumar, Dr. S. Anandan, Dr. N.K. Rotte, Dr. G.V. Ramana, Mr. N. Ravikiran, Mr. Akshay, Mr. G.V. Reddy, Mr. E. Konda, and Mr.P. Anjaiah*** for their immense help in characterization. I am also thankful to all other employees of ARCI and NITW who have helped directly or indirectly during course of research work. Finally, the last but most important, I am grateful to my parents and family members.

**Balaji Padya**

## **ABSTRACT**

Since the industrial revolution, fossil fuels are enormously exploited to meet the energy required for the population explosion that resulted in deteriorated environmental conditions. Accounting for these devastating challenges, humankind is forced to pursue clean and green technology for sustainable development. Consequently, modern transportation is shifting to zero-emission electric vehicles (EV). For EV, an electrochemical system (supercapacitors and batteries) is the primary source for providing energy density and power density. The porous carbon-based materials are widely exploited to derive a unique electrochemical system, especially hybrid supercapacitor, due to remarkable physicochemical characteristics. However, hybridizing a concept of battery and supercapacitor is stimulated to achieve high energy density and power density to apply for EV, which require thermal management of battery module to suppress a phenomenon of thermal runaway. This thesis aims to address the critical issues on automotive material property characterization, capacitive energy storage, and thermal energy storage, which suits EV applications.

In the initial phase, intensifying process parameters for generation of few-layer graphene platelets (FGP) via solution-phase exfoliation, nitrogen-doped tubular carbon (NTC) via chemical vapour deposition and deoxygenated graphene oxide (DGO) via temperature-mediated deoxygenation was carried out. Then, functional nanocomposites based on FGP, NTC and DGO were developed for thermal and capacitive energy storage.

In the second phase, FGP, NTC and DGO based nitrogen-doped porous carbon called PNCG, PNCT, PNCD, respectively, were prepared to apply as electrode material for symmetric carbon/carbon supercapacitor. PNCG, PNCT, PNCD and YP-50 exhibited specific capacitance (3M KOH, 0.5 A/g, graphite foil) of 188, 147, 121, and 114 F/g, respectively. Further, capacity retention of the porous carbon was carried out at 0.5 A/g for 1000 cycles, demonstrated that PNCG, PNCT, PNCD and YP-50 exhibited capacity retention of 96.82, 93.26, 90.50 and 96.43 %, respectively. Considering the contribution from all the physicochemical aspects, the electrochemical properties of the porous carbon found in the order: PNCG>PNCT>YP-50>PNCD. Similarly, porous surface-etched graphene platelets were explored as electrode material for energy storage.

In the third phase, porous carbon-based cathode material for asymmetric supercapacitor (Li-ion hybrid supercapbattery) was developed. PNCG displayed the specific capacity of 188.8, 172.9, 156.9 and 135.4 mAh/g at the discharge current-density of 0.2, 0.5, 1.0 and 2.0 A/g, respectively.

Moreover, PNCG without graphene displayed a specific capacity of 99.0, 83.9, 66.9 and 43.7 mAh/g at 0.2, 0.5, 1.0 and 2.0 A/g, respectively. Furthermore, it presented a discharge capacity of 147.9 mAh/g after 500 cycles at a current density of 1.0 A/g with retention of 94.2 % capacity demonstrating exceptional cycle stability.

In the final phase, myristic (M) and stearic acid (S) based eutectic system (MS) was established in which the nanocarbon materials with variable structural degree (FGP>NCT>DGO) are added to improve thermal transport. Fascinatingly, the MS system's figure-of merit based on thermal conductivity follows the tendency: MS-FGP>MS-NTC>MS-DGO. The significant increase in thermal conductivity (597 %) and appropriate phase transition peak (46.04 °C) were achieved with 5 wt.% FGP loading, which could find a suitable way for thermal management system-battery (TMSB) applied in electric vehicles.

Overall, FGP based hybrids exhibited remarkable capacitive and thermal energy characteristics, which accounts for the highest structural degree, crystallinity and 2D planar structure.

## CONTENTS

<b>Chapter</b>	<b>Description</b>	<b>Page No.</b>
<b>No.</b>		
	Abstract	vii
	Index of Figures	xii
	Index of Tables	xv
	Index of Abbreviations	xvi
<b>Chapter-1</b>	<b>Introduction</b>	1
1.1	Background	1
1.2	Motivation and Thesis Objectives	3
1.3	Research Scope and Approach	4
1.4	Organization of Thesis	5
1.5	References	7
<b>Chapter-2</b>	<b>Literature Review: Materials for energy storage</b>	10
2.1	Necessity of energy storage technologies	10
2.2	Advanced materials for supercapacitors	11
2.2.1	The organized approach for high energy density SCs	14
2.2.2	Factors affecting the electrochemical performance of SCs	15
2.3	Advanced materials for thermal energy storage	19
2.3.1	Need of PCM in EV	19
2.3.2	Materials for TMSB: PCM and fillers	22
2.4	References	28
<b>Chapter-3</b>	<b>Instrumentation &amp; Characterization and Methodology</b>	40
3.1	Instrumentation & Characterization	40
3.2	Methodology	43
3.3	References	44
<b>Chapter-4</b>	<b>Nanocarbon/N-doped carbon hybrid for symmetric supercapacitor</b>	47
4.1	Introduction	47
4.2	Materials and methods	48
4.3	Results and discussion	50
4.4	Conclusions	56

4.5	References	58
<b>Chapter-5</b>	<b>Surface-etched nanoscaled-graphene platelets based porous carbon for supercapacitor</b>	65
5.1	Introduction	65
5.2	Experimental	67
5.2.1	Materials and reagents	67
5.2.2	Preparation of NGNS and its surface modification	67
5.2.3	Instrumentation and characterization	68
5.3	Results and discussion	69
5.3.1	Preparation of NGNS and aNGNS	69
5.3.2	Porosity and electrochemical properties of aNGNS	72
5.4	Conclusions	76
5.5	References	78
<b>Chapter-6</b>	<b>Graphene-coupled nitrogen-doped carbon-based hybrid for supercapbattery</b>	83
6.1	Introduction	83
6.2	Materials and Methods	84
6.2.1	Preparation of PNCG	84
6.2.2	Characterization-related instruments	85
6.2.3	Electrode preparation and fabrication of electrochemical cell	86
6.3	Results and discussion	86
6.3.1	Morphology and physicochemical characterization	86
6.3.2	Li-storage properties of PNCG	91
6.4	Conclusions	95
6.5	References	97
<b>Chapter-7</b>	<b>Nanocarbon-loaded PCM for thermal energy storage</b>	100
7.1	Introduction	100
7.2	Materials and methods	102
7.3	Results and discussion	104
7.3.1	Morphological and structural properties of nanocarbon: FGP, NTC and DGO	104

7.3.2	Thermal conductivity and thermophysical properties of MS-PCM system	106
7.4	Conclusions	110
7.5	References	112
<b>Chapter-8</b>	<b>Conclusion and Scope for Future works</b>	117
8.1	Conclusions	117
8.2	Scope for further research	118
	List of Publications	119
	Curriculum Vitae	121

## INDEX OF FIGURES

<b>Figure No.</b>	<b>Description</b>	<b>Page No.</b>
<b>Fig.1.1</b>	Driving the future: transforming to green technologies	3
<b>Fig.1.2</b>	Adopted approach to solve existing bottlenecks	5
<b>Fig. 2.1</b>	Classification of various energy storage systems	10
<b>Fig.2.2</b>	Ragone plot indicating the ED vs PD for different electrical energy- storage systems. Times marked in the plot are the discharge time, achieved by dividing the PD by the ED	11
<b>Fig. 2.3</b>	Global SC market	12
<b>Fig. 2.4</b>	Historical timeline for the development of SCs and advancement in the phenomenon of storage mechanism	12
<b>Fig. 2.5</b>	Classification of SCs based on charge storage mechanism and materials	13
<b>Fig. 2.6</b>	Schematic interpretation of different possible hybridization approaches between SCs, LIBS, and materials	14
<b>Fig. 2.7</b>	Illustrating the properties of materials for high-performance electrodes	15
<b>Fig. 2.8</b>	The ED and PD of LIBS and SCs: (a) trend of ED, (b) trend of PD	19
<b>Fig. 2.9</b>	(a) Global demand for EV system for next decade (72) and (b) Year- wise statistics of journal papers on TMSB	20
<b>Fig. 2.10</b>	Illustration of TRP initiation and interpretation of temperature- dependent chain reaction	20
<b>Fig.2.11</b>	Classification of TMSB	21
<b>Fig.2.12</b>	Illustration of underlying principle involved in heat storage/release by PCM	22
<b>Fig.2.13</b>	Influence of temperature on the performance of LIBS	23
<b>Fig.2.14</b>	Illustration of various strategies to improve the thermal conductivity of PCM	25
<b>Fig.3.1</b>	A schematic depicting the methodology adopted for research work	43
<b>Fig.4.1</b>	Schematic diagram depicting the procedure for preparation of PNCG, PNCT and PNCD	49

<b>Fig.4.2</b>	SEM images of (a) FGP, (b) NTC, (c) DGO, (d) PNCG, (e) PNCT, and (f) PNCD	50
<b>Fig.4.3</b>	Raman signatures	51
<b>Fig.4.4</b>	Elemental composition of PNCG, PNCT and PNCD: (a) XPS wide scan, and (b) N-content	52
<b>Fig.4.5</b>	Electrochemical capacitive properties of PNCG, PNCT and PNCD: (a) CV, (b) GCD, (c) rate capability and (d) EIS Nyquist plot	53
<b>Fig.4.6</b>	Cyclic stability-based capacitance retention of PNCG, PNCT, PNCD and YP-50	54
<b>Fig.4.7</b>	Ragone plot of symmetric supercapacitor cell: PNCG//PNCG, PNCT//PNCT, PNCD//PNCT and YP-50//YP-5	55
<b>Fig. 4.8</b>	A radar plot depicting the physicochemical and electrochemical properties of PNCG, PNCT, PNCD and YP-50	55
<b>Fig.S4.1</b>	NTC growth: (a) NTC-yield and N-content, (b) Raman signatures, (C) weight loss and (d) derivative weight loss	63
<b>Fig.S4.2</b>	SEM images of (a) NTC-800, (b) NTC-850, and (c) NTC-900; TEM image of (d) NTC-800, (e) NTC-850, and (f) NTC-900.	63
<b>Fig.S4.3</b>	DGO preparation: (a) XRD pattern (b) Raman signatures (c) XPS-wide scan and (d) C/O ratio	64
<b>Fig.S4.4</b>	SEM images of (a) GO (b) DGO-120, (c) DGO-150 (d) DGO-180, (e) DGO-210; TEM image of (f) DGO-210.	66
<b>Fig. 5.1</b>	Schematic diagram indicating the flow-chart for the preparation of aNGNS	70
<b>Fig. 5.2</b>	High-resolution TEM images of GNP (a), NGNS (b) and Raman signatures (c)	71
<b>Fig.5.3</b>	SEM images of NGNS (a), and aNGNS (b) in powder form	72
<b>Fig.5.4</b>	Nitrogen adsorption–desorption isotherm (a) and pore size distribution (b) of aNGNS	73
<b>Fig.5.5</b>	Electrochemical properties of aNGNS: Cyclic voltammetry (a), Charging-discharging curves (b), Specific capacitance (c)	74
<b>Fig.5.6</b>	Ragone plot of aNGNS based supercapacitor cell	74

<b>Fig.5.7</b>	Frequency-response analysis by electrochemical impedance spectroscopy: Nyquist plot (a), and bode plot (phase vs. frequency) (b) and imaginary capacitance vs. frequency (b).	75
<b>Fig.6.1</b>	Morphology of (a) NG, (b) PNCG without NG, and PNCG at (c) low magnification, and (d) high magnification	87
<b>Fig.6.2</b>	TEM micrographs of PNCG at (a) low magnification, (b) high magnification and SAED pattern of (c) spot 1 and (d) spot 2 present in 2a along with TEM images of NG with minimal layers (e and f).	88
<b>Fig.6.3</b>	Thermal stability (TG, DTA and DTG) of PNCG	89
<b>Fig.6.4</b>	Nitrogen adsorption/desorption with pore-size distribution of PNCG	89
<b>Fig. 6.5</b>	Elemental functionality present in PNCG: (a) XPS wide scan, (b) N1s narrow scan, (c) C1s narrow scan, and (d) O1s narrow scan	90
<b>Fig.6.6</b>	<b>Fig.6.6</b> (a) Raman spectra, and (b) XRD pattern of NG and PNCG	90
<b>Fig.6.7</b>	Electrochemical properties of PNCG: (a) CV, (b) CD, (c) capacity vs current density, (d) cyclic stability, and (e) Nyquist plot	93
<b>Fig.6.8</b>	‘Charge-averaged’ charge/discharge voltages: (a) for rate capability, and (b) for cyclic stability	94
<b>Fig. 7.1</b>	SEM images of (a) FGP, (b) NTC, and (c) DGO; TEM images of (d) FGP, (e) NTC and (f) DGO.	105
<b>Fig. 7.2</b>	(a) Raman spectrum and (b) XRD pattern of FGP, NTC and DGO	105
<b>Fig. 7.3</b>	(a) TG and (b) DTG curves of FGP, NTC and DGO.	106
<b>Fig. 7.4</b>	Phase diagram of MS system	106
<b>Fig. 7.5</b>	(a) thermal conductivity of MS, MS-FGP, MS-NTC and MS-DGO and (b) thermal transport mechanism in FGP, NTC and DGO	107
<b>Fig. 7.6</b>	Variation in thermal conductivity of MS-xFGP as a function of FGP loading	108
<b>Fig. 7.7</b>	(a) Phase transition peak characteristics and (b) latent heat of fusion of MS-xFGP system	109
<b>Fig. 7.8</b>	Normalized enthalpy ratio during (a) melting and (b) cooling	109

## INDEX OF TABLES

<b>Table No.</b>	<b>Description</b>	<b>Page No.</b>
2.1	Comparison of SCs: electrode materials along with charge storage mechanism	14
2.2	Physical and electrochemical properties of various porous N-doped carbon used in SCs	17
2.3	Comparison showing the specific capacity of various porous carbon materials for Li-storage	18
2.4	Thermophysical properties of some fatty acids	24
2.5	Comparison of thermal conductivity with different nanoadditives	26
4.1	Elemental composition of PNCG, PNCT and PNCD	52
4.2	Comparison of electrochemical performance of various porous carbon	57
5.1	Comparison of supercapacitor performance of graphene-based porous materials	76
6.1	Literature comparison showing the specific capacity of various porous carbon materials	96
7.1	A comparison of increase in thermal conductivity of carbon-loaded various PCMs	111

## INDEX OF ABBREVIATIONS

Abbreviation	Description
FF	Fossil fuels
EV	Electric Vehicle
IESD	Integrated Energy Storage Device
ECES	Electrochemical Energy Storage System
TES	Thermal Energy Storage
LIBS	Li-ion based Battery System
SC	Supercapacitor
HSS	Hybrid Supercapacitor System
ED	Energy Density
PD	Power Density
PCM	Phase Change Materials
TRP	Thermal Runaway Phenomenon
FGP	Few-layer Graphene Platelets
NTC	Nitrogen-doped Tubular Carbon
DGO	Deoxygenated Graphene Oxide
ESS	Energy Storage Systems
EDC	Electric Double-layer Capacitor
PC	Pseudocapacitors
TMSB	Thermal Management System-Battery
MEG	Microwave-assisted Expanded Graphite
S	Stearic Acid
M	Myristic Acid
SEM	Scanning electron microscopy
TEM	Transmission Electron Microscopy
XRD	X-ray Diffraction Analysis
STA	Simultaneous Thermal Analysis
XPS	X-ray Photoelectron Spectroscopy
LFA	Laser Flash Analyzer
DSC	Differential Scanning Calorimetry
DTG	Differential Thermogravimetry

<b>Abbreviation</b>	<b>Description</b>
CV	Cyclic voltammetry
GCD	Galvanostatic Charge-discharge
EIS	Electrochemical impedance spectroscopy
CES	Capacitive Energy Storage
NC	Nitrogen-enriched Carbon
PNCG	Nitrogen-enriched Carbon-FGP
PNCT	Nitrogen-enriched Carbon-NTC
PNCD	Nitrogen-enriched Carbon-DGO
KOH	Potassium hydroxide
NGNS	Nanoscaled-Graphene Nanoplatelets
aNGNS	Activated-NGNS
DMSO	Dimethyl sulfoxide
DMF	Dimethyl formamide
NMP	N-methyl pyrrolidone
NGF	Natural graphite flakes
GNP	Graphene Nanoplatelets
Rs	Electrode resistance
Rct	charge transfer resistance
AESD	Advanced Energy Storage Devices
HLS	Hybrid Li-ion supercapbattery
PVDF	Polyvinylidene Fluoride
SAED	Selected Area Diffraction Pattern
NG	Nanoscaled-graphene
HDL	Helmholtz Double-layer
CADV	Charge-averaged Discharge Voltage
CACV	Charge-averaged Charge Voltage
Ex-G	Exfoliated Graphite
FOM	Figure of Merit
MS	Myristic-stearic Eutectic
MWCNTs	Multi-walled carbon nanotubes
CF	Carbon fibers

# CHAPTER-1

---

## Introduction

---

### 1.1 Background

The ever-increasing demand for energy sources combined with the rapid development of the global economy for indispensable needs in respect of industrial capacity, manufacturing sector, automotive sector and various other sectors is exclusively dependent on traditional fossil fuels (FF), which has to be transformed to green materials-based technologies (1-3). Population explosion is one of the prime causes to make dependency on such non-renewable sources to meet energy required for every usage (4-6). Usage of such FF like coal, petroleum-derived sources and others may lead to their depletion near future if the present rate of consumption of energy is continued. Usage of FF creates environmental issues like depletion of ozone layer, global warming, melting of glaciers, hazardous to aquatic species, and other critical issues (2). Furthermore, the research community is switching over to usage of renewable sources and environmental-friendly energy sources for generation/conversion of energy (3, 6). Moreover, their intermittent nature and which could readily have influenced significantly by external climatic conditions.

Unfortunately, the world's energy generation is repeatedly reliant on FF-derived sources (coal and its derivatives) for several centuries. Almost all the automobile vehicles are widely exploiting petroleum-derived fuels causing massive air pollution (1). Coincidentally, the researchers exploring the wide variety of sustainable renewable sources to alleviate the environmental-related vital issues. However, renewable sources' intermittent nature enforces us to store the energy to narrow down the gap between energy demand and supply. Currently, prodigious attention is being paid in developing advanced energy storage devices for electric vehicles (EV) in automobiles for transportation and other applications (7-10). However, the system of integrated energy storage device (IESD) used for transportation consists of electrochemical energy storage system (ECES) in combination with thermal energy storage (TES) for thermal management to enable safety aspects. The combination of ECES and TES ensure the EV system to validate driving capability with utmost safety (11-14).

Usually, ECES system consists of Li-ion based battery system (LIBS) or supercapacitor (SC) or hybrid supercapacitor system (HSS) to assist the energy required for driving EV. The EV system with high energy density (ED) and high-power density (PD) is of enormous interest to

establish robust appliances to find appropriateness in modern applications. The LIBS and SC are rich in energy density and power density, respectively, and lack vice versa. To combine LIBS and SC's better properties, a notion of hybridizing them was conceptualised to deliver sufficient ED and PD. The integrated system that delivers high ED and PD required for EV is termed as HSS. In HSS, anode and cathode works on principles of LIBS and SC, respectively. Sometimes, hybrid material consist of materials of LIBS and SCs together responsible for mixed-principle which supports energy storage. The working principle of both the electrode materials differs from each other: anode responsible for LIBS and cathode for SCs mechanism. Consequently, developing suitable electrode materials (porous carbon) through advancing materials technology with cutting-edge features plays a strategic role in preparing robust HSS (15-21). In line with this, the nanocarbon-based hybrid with suitable porosity is developed to design high-performance ECES. Nanocarbon materials are incorporated in a hybrid to ensure the required electrical transport.

Similarly, a TES designed for EV system possesses a high-performance thermal management system in which the heat generated from the ECES should be dissipated quickly (22-24). The prolonged EV driving produces enormous heat during the charging and discharging process of ECES (especially LIBS) due to chemical reactions. The heat should be dissipated by adopting various conventional routes, but a concept of usage of phase change materials (PCM) for heat absorb/release finds its best suitability and advantages. Depending on latent heat and phase transition temperature, various kinds of fatty acids are extensively studied (25-27). However, the PCM system with phase transition in the range of 45-50 °C is critical to find its applicability for EV (28-31). To derive the suitable phase transition temperature, a eutectic binary system consisting of myristic acid and stearic acid was developed. Commonly, fatty acid-based PCM possesses very low thermal conductivity, which hinders the heat propagation. To increase the thermal conductivity of PCM, a small quantity of fillers are added. Among all additives, nanoscaled carbon additives, especially graphene find its promising place owing to its very high thermal conductivity and other salient features (32, 33).

Lastly, this study emphasizes a concept of advancing automotive materials technology to process, synthesize and characterize novel materials useful in developing ECES and TES to find application in EV.

## 1.2 Motivation and Thesis Objectives

The focus was laid on developing integrated energy storage devices by advancing automotive materials technology to support sustainable development via green technologies. Developing novel materials based high performance green technologies as an alternative to the conventional system i.e., replacement of gasoline-based energy system to EV-based energy system is the prime motivation as depicted in **Fig.1.1**.

Primarily, the materials required for ECES are prepared to support short ion-transport pathways to increase the capacitance. The device with high energy density and high power density are of immense interest to support modern applications. To meet such parameters, a material with exceptional physicochemical properties are desirable. In support of this, the porous and electroactive materials (N-doped) are developed in facile routes.

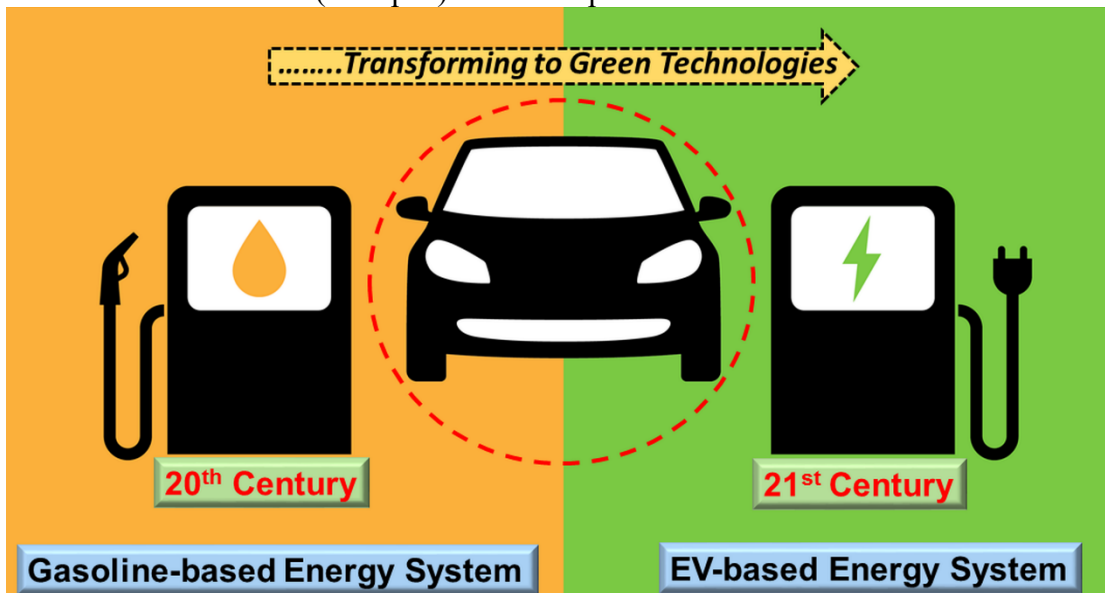


**Fig. 1.1** Driving the future: transforming to green technologies.

Though carbonaceous materials possess remarkable properties such as high electrical conductivity, chemical inertness and surface area, they suffer from low specific capacitance and low energy density, which is a serious issue to be taken care for real-time applications. On the contrary, electroactive redox (metal-based) materials exhibit high specific capacitance but lacking in cyclic stability. The drastic fade in capacitance over repeated cycles for longer duration and less electrical conductivity is a significant disadvantage for practical application. In such cases, nanoelectrodes' development based on integrating electroactive redox material coupled with carbonaceous materials to obtain a synergistic effect to improve specific energy density and specific power density is highly recommended to prepare high-performance electrode material.

In fact, asymmetric ultracapacitor with a widened potential window is desirable as the symmetric ultracapacitor possesses a very narrow potential window. The ED of the electrode material are improved by increasing the potential window of the system. To obtain such characteristics, the carbonaceous nanostructures coupled with redox materials (N-doped) based hybrids are developed. To bridge the gap between the energy supply and demand, ultracapacitor's electrode with high ED and PD was developed via advancing the materials based technology.

Secondly, a novel thermal management system with improved thermal energy storage by applying PCM is required for EV. In which, nanoadditives are loaded to enhance thermal conductivity and heat transfer of PCM as the pristine organic (fatty acids) PCM possesses low thermal conductivity (34). In order to suppress thermal runaway phenomenon (TRP), a PCM with high latent heat and exceptional thermal conductivity are desirable. To achieve remarkable thermal conductivity of PCM composites, carbon-based nanoadditives are loaded with sacrificing the latent heat.

This thesis exclusively emphasized on development of nanomaterials (1-D and 2-D) based functional nanocomposites for hybrid electrochemical energy storage and thermal energy storage systems applied in electric vehicles via advancing the automotive materials technology approach.

### **1.3 Research Scope and Approach**

As a part of developing materials for zero-emission EV, an ECES with high ED and PD and efficient TES to comply safety norms are desirable. In this context, advancing automotive materials technology to design a rational material framework with a simple and cost-effective process was developed. This thesis's focus includes advancing materials technology to develop nanocarbon and nanocarbon-enabled functional nanocomposites for an integrated energy storage device with high PD and ED with safety aspects.

As a part of this, various innovative methods were deployed as follows:

- Intensifying process parameters to grow small-scaled carbonaceous nanostructures such as few-layer graphene platelets (FGP), nitrogen-doped tubular carbon (NTC) and deoxygenated graphene oxide (DGO).
- Preparation of nanocarbon (FGP or NTC or DGO)/nitrogen-enriched carbon hybrid with porosity-rich framework

- Designing capacitive-type electrode (cathode) for hybrid energy storage device (asymmetric) with exceptional electrochemical characteristics
- Processing and evaluation of electrochemical properties of as-prepared porous carbon based electrodes in comparison to commercially applied YP-50.
- Preparation of nanocarbon (FGP or NTC or DGO)/PCM composite with high thermal conductivity to suppress thermal runaway phenomenon (TRP)

As a remedy to solve existing bottlenecks in the field of ECES and TES, the novel approaches are adopted as shown **Fig.1.2**.

Electrochemical Energy Storage System				
S.No	Bottlenecks	Approach	Execution	Remarks
1	Low electrical conductivity and desired pore-size	Nanostructuring-approach	Nanocarbon hybrid and activation	$E = 0.5 CV^2$
2	Low capacitance	Doping-approach	N-doping	
3	Low voltage window	Hybridizing devices-approach	Capacitive-type cathode	$C \uparrow \quad V \uparrow$

Thermal Energy Storage System				
1	Phase transition : 45-50 °C	Eutectics-approach	Myristic-Stearic acid	$q = k \Delta T$
2	Low thermal conductivity	Nanofiller-approach	Nanocarbon addition	$k \uparrow$

**Fig.1.2** Adopted approach to solve existing bottlenecks.

#### 1.4 Organization of Thesis

This thesis tackles and throw light on IESD consist of ECES and TES for EV used in automotive sector. The thesis is categorized into 8 chapters with studies performed on advancing materials technology to develop functional nanocomposite materials.

**Chapter 1** states the background for research question, Motivation and Objectives, Research scope and Approach, and organization of the thesis.

**Chapter 2** includes comprehensive literature review explaining concepts on growth and energy storage property study of low-dimensional carbon materials based functional nanocomposites for ECES and TES. It delineates work status concerning previous reports based on synthesis

processes, growth mechanisms, underlying principles, and growth kinetics of small-scaled nanostructures. It presents the mechanism of energy storage in ECES and TES and kind of nanoscaled materials applied for them.

**Chapter 3** includes the instrumentation & characterization and methodology.

**Chapter 4** contains the electrochemical properties of three kinds of porous carbon materials and commercially available activated carbon applied for symmetric supercapacitor

**Chapter 5** describes the electrochemical characteristics of porous graphene platelets applied for symmetric supercapacitors

**Chapter 6** deals with graphene platelets based porous carbon as cathode material for asymmetric supercapacitor

**Chapter 7** describes the preparation and thermal energy storage properties of nanocarbon loaded phase change materials

**Chapter 8** provides the summary of the research work and conclusion on the raised research questions followed by scope of future work.

## 1.5 References

1. D.A. Lashof, D.R. Ahuja, Relative contributions of greenhouse gas emissions to global warming, *Nature* 344 (1990) 529-531.
2. S. Chu, A. Majumdar, Opportunities and challenges for a sustainable energy future, *Nature* 488 (2012) 294-303.
3. D.G. Nocera, Living healthy on a dying planet, *Chem. Soc. Rev.* 38 (2009) 13-15.
4. A. Hagfeldt, G. Boschloo, L. Sun, L. Kloo, H. Pettersson, Dye-sensitized solar cells, *Chem. Rev.* 110 (2010) 6595-6663.
5. K. Christopher, R. Dimitrios, A Review on exergy comparison of hydrogen production methods from renewable energy sources, *Energy Environ. Sci.* 5 (2012) 6640-6651.
6. S. O. Amrouche, D. Rekioua, T. Rekioua, S. Bacha, Overview of energy storage in renewable energy systems, *Int. J. Hydrogen Energy* 41 (45) (2016) 20914-20927.
7. M. Wada, Research and development of electric vehicles for clean transportation, *J. Environ. Sci.* 21 (2009) 745-749.
8. S.J. Skerlos, J.J. Winebrake, Targeting plug-in hybrid electric vehicle policies to increase social benefits, *Energy Policy* 38 (2010) 705-708.
9. P. Baptista, M. Tomás, C. Silva, Plug-in hybrid fuel cell vehicles market penetration scenarios, *Int. J. Hydrogen Energy* 35 (2010) 10024-10030.
10. J. Dong, C. Liu, Z. Lin, Charging infrastructure planning for promoting battery electric vehicles: an activity-based approach using multiday travel data, *Transport. Res. Part C: Emerg. Technol.* 38 (2014) 44-55.
11. A. Barré, B. Deguilhem, S. Grolleau, M. Gérard, F. Suard, D. Riu, A review on lithium-ion battery ageing mechanisms and estimations for automotive applications, *J. Power Sources* 241 (2013) 680-689.
12. J. Jaguemont, N. Omar, P. Van den Bossche, J. Mierlo, Phase-change materials (PCM) for automotive applications: A review. *Appl. Therm. Eng.* 132 (2018) 308-320.
13. N. Yang, X. Zhang, G. Li, D. Hua, Assessment of the forced air-cooling performance for cylindrical lithium-ion battery packs: a comparative analysis between aligned and staggered cell arrangements, *Appl. Therm. Eng.* 80 (2015) 55-65.
14. K. Yu, X. Yang, Y. Cheng, C. Li, Thermal analysis and two-directional air flow thermal management for lithium-ion battery pack, *J. Power Sources* 270 (2014) 193-200.
15. H. Catherino, J. Burgel, P. Shi, A. Rusek, X. Zou, Hybrid power supplies: a capacitor assisted battery, *J. Power Sources* 162 (2006) 965-970.

16. W. Henson, Optimal battery/ultracapacitor storage combination, *J Power Sources* 179 (2008) 417-423.
17. G. Sikha, B. Popov, Performance optimization of a battery-capacitor hybrid system, *J Power Sources* 134 (2004) 130-138.
18. W. G. Pell, B.E. Conway, Peculiarities and requirements of asymmetric capacitor devices based on combination of capacitor and battery-type electrodes, *J. Power Sources* 136 (2004) 334-345.
19. H.S. Choi, C. R. Park, Theoretical guidelines to designing high performance energy storage device based on hybridization of Lithium-ion battery and supercapacitor, *J. Power Sources* 259 (2014) 1-14.
20. B. Akinwolewiwa, C. Wei, G.Z. Chen, Mechanisms and designs of asymmetrical electrochemical capacitors, *Electrochim. Acta* 2017, 247 (2017) 344-357.
21. A. Jagadale, X. Zhou, R. Xiong, D. P. Dubal, J. Xu, S. Yang, Lithium-ion capacitors (LICs): Development of the materials, *Energy Storage Mater* 19 (2019) 314-329.
22. P.R. Tete, M. M. Gupta, S.S. Joshi, Developments in battery thermal management systems for electric vehicles: A technical review, *J Energy Storage* 35 (2021) 102255 (63pp).
23. P. Kumar, D. Chaudhary, P. Varshney, U. Varshney, S. M. Yahya, Y. Rafat, Critical review on battery thermal management and role of nanomaterial in heat transfer enhancement for electrical vehicle application, *J Energy Storage* 32 (2020) 102003 (25pp).
24. M. Malik, I. Dincer, M.A. Rosen, Review on use of phase change materials in battery thermal management for electric and hybrid electric vehicles, *Int. J. Energy Res.* (2016) 1011-1031.
25. K. Kant, A. Shukla, A. Sharma, Ternary mixture of fatty acids as phase change materials for thermal energy storage applications, *Energy Reports* 2 (2016) 274-279.
26. H. Ke, Phase diagrams, eutectic mass ratios and thermal energy storage properties of multiple fatty acid eutectics as novel solid-liquid phase change materials for storage and retrieval of thermal energy, *Appl. Therm Eng* 113 (2017) 1319-1331.
27. S. Kahwaji, M.A. White, Prediction of the properties of eutectic fatty acid phase change materials, *Thermochim Acta* 660 (2018) 94-100.

28. X. Feng, M. Ouyang, X. Liu, L. Lu, Y. Xia, X. He, Thermal runaway mechanism of lithium-ion battery for electric vehicles: A review, *Energy Storage Mater* 10 (2018) 246-267.
29. R. Spotnitz, J. Franklin, Abuse behaviour of high-power, lithium-ion cells, *J. Power Sources* 113 (1) (2003) 81-100.
30. Q. Wang, P. Ping, X. Zhao, G. Chu, J. Sun, C. Chen, Thermal runaway caused fire and explosion of lithium-ion battery, *J. Power Sources* 208 (2012) 210-224.
31. S. Arora, Selection of thermal management system for modular battery packs of electric vehicles: A review of existing and emerging technologies, *J Power Sources* 400 (2018) 621-640.
32. G. Yang, Y. Yim, J. Lee, Y. J. Heo, S. J. Park, Carbon-filled organic phase-change materials for thermal energy storage: a review, *Molecules* 24 (2019) 2055 (17pp).
33. L.A. Jauregui, Y. Yue, A.N. Sidorov, J. Hu, Q. Yu, G. Lopez, R. Jalilian, D.K. Benjamin, D.A. Delk, W. Wu, Z. Liu, X. Wang, Z. Jiang, X. Ruan, J. Bao, S.S. Pei, Y.P. Chen, Thermal transport in graphene nanostructures: experiments and simulations, *ECS Transactions* 28 (2010) 73-83.

## CHAPTER-2

### Literature Review: Materials for energy storage

#### 2.1 Necessity of energy storage technologies

The population explosion-driven tremendous energy usage led to the rapid exhaustion of FF. In addition, its exploitation for fast manufacturing and industrial sectors created environmental deterioration associated with greenhouse gas emissions, which has driven increasing global demands to develop sustainable energy supply (1-3). Consequently, sustainable development hand-in-hand with wide usage of renewable sources such as solar, hydro, geotechnical, wind energy etc., are the favourite remedy for addressing these key concerns (4-10). These renewable sources' intermittent nature forced us to look at an alternative to store them for usage to ensure availability at odd times.

Advanced and efficient storage technologies are on top priority to mitigate fluctuation in energy generation and release for usage along with energy generation. To ensure energy availability in odd hours, energy storage systems (ESS) such as chemical ESS, mechanical ESS, biological ESS, magnetic ESS, thermochemical ESS and thermal ESS are prominent to store energy, as depicted in **Fig.2.1**. ESS act as an energy reservoir for energy release during its demand (11).

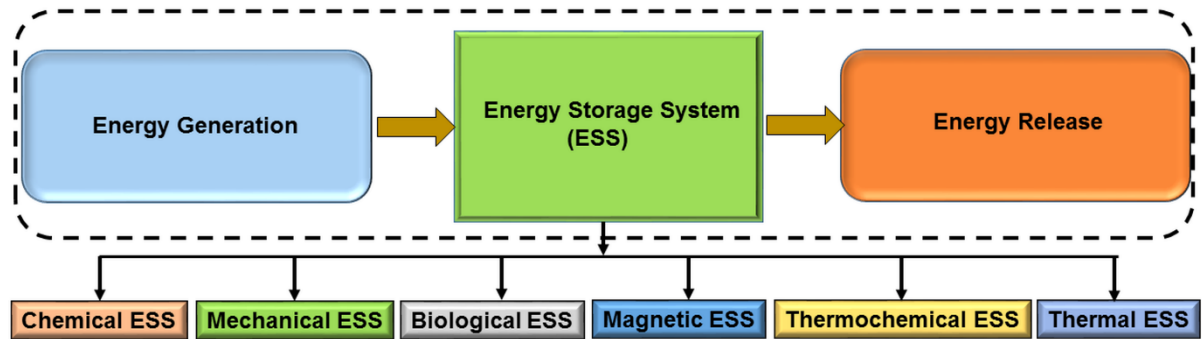


**Fig. 2.1** Classification of various energy storage systems (11).

In the process of developing green technology-based appliances to mitigate environmental-related issues, EV systems in transportation have drawn colossal interest (12-17). LIBS, SC and HSS working on chemical ESS are considered the central part of the EV system to provide energy, and power and a compatible thermal ESS to meet safety aspects (14-17, 18). Though the concept of chemical ESS and thermal ESS is well-known for many years, the advancing materials technology-based materials with cutting-edge features are attracted immensely in developing high-performance compact devices. The comprehensive state-of-the-art advancement in

materials for chemical ESS and thermal ESS are described in **Section 2.2** and **Section 2.3**, respectively.

## 2.2 Advanced materials for supercapacitors

Electrochemical capacitor systems are currently being used in innovative applications (stationary and on-board) due to attractive electrochemical properties (19-25). Depending on ED and PD requirements, the SC system has drawn a great deal of attention to develop a compact device that can deliver high ED and high PD, as illustrated in **Fig. 2.2** (26-28). In such cases, the materials with salient features are decisively required for electrode preparation. In the last few decades, enormous efforts have been made to enhance SC's performance using novel materials with shape-designed architecture for swift ion-transport via creating shorten ion-diffusion path length (23, 26, 27). Even though the SCs have greatly improved (materials and cell-design) with a timeline, they lack sufficient ED. According to a recent report released by IDTechEx, the SC market is supposed to reach 8.3 billion US dollars by 2025, as shown in **Fig. 2.3** (29, 30). Surprisingly, the global market is driven by applying SC in zero-emission vehicles in a wide variety of locomotives such as buses, trucks, load-levelling system, trains, and aircraft. The strategy of lowering-emission, environmental-driven exploitation, global warming, government boosting, and emerging start-ups made the exponential increase in the SC market.

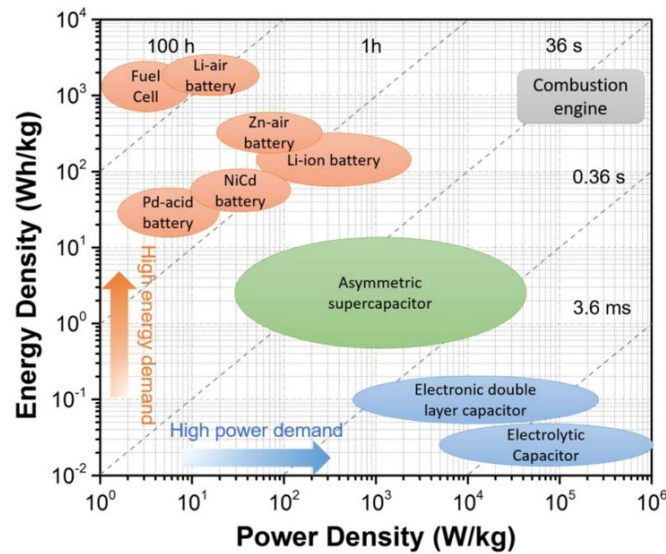


**Fig. 2.2** Ragone plot indicating the ED vs PD for different electrical energy-storage systems. Times marked in the plot are the discharge time, achieved by dividing the PD by the ED (26).

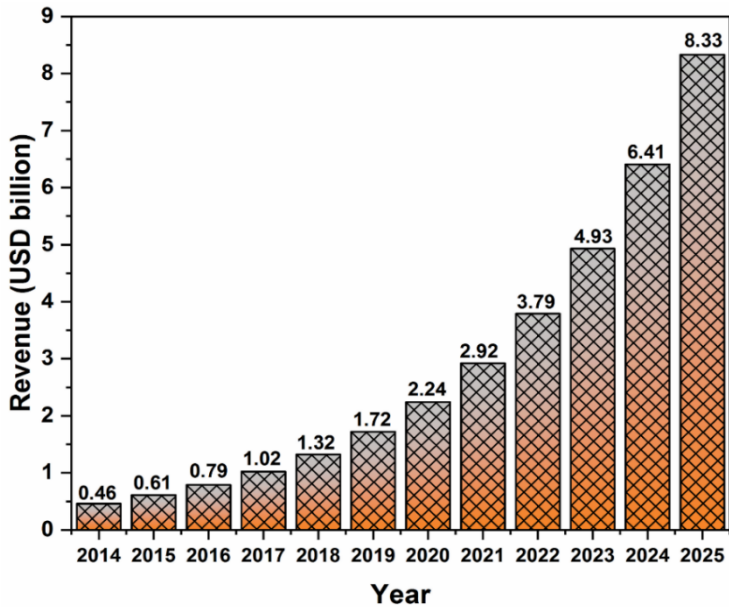


**Fig. 2.3** Global SC market (30).

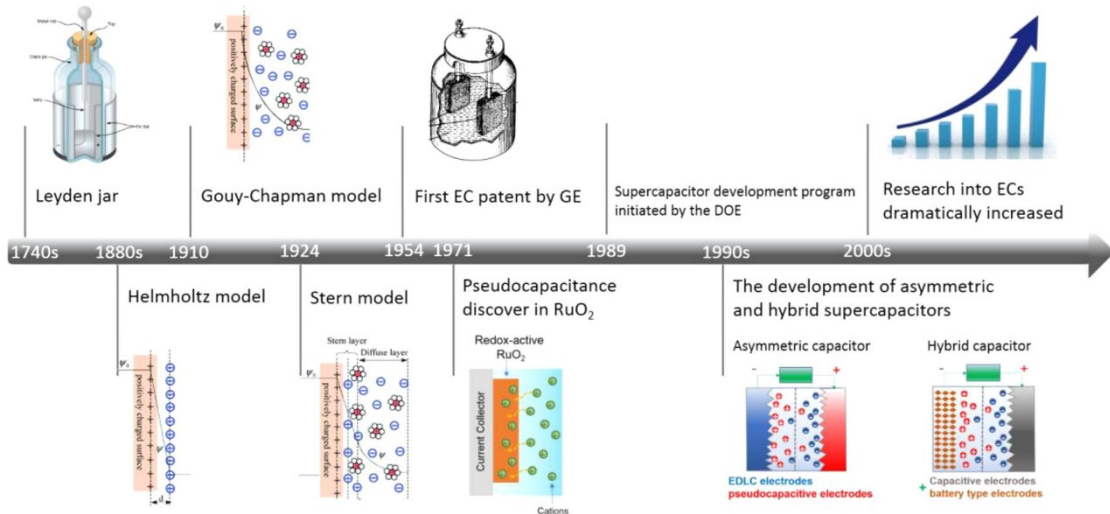


**Fig. 2.4** Historical timeline for the development of SCs and advancement in the phenomenon of storage mechanism (26, 36).

On the other hand, SC can complement or replace LIBS in few applications because they exhibit high PD, rapid charging and long cycle life. The advantages of SC triggered a considerable market to apply them for modern compact appliances. Though commercially available SC can deliver higher ED in comparison to the conventional solid-state electrolytic capacitor (up to 5 Wh/kg); still, it is significantly inferior to LIBS (up to 200 Wh/kg) and fuel cells ( $\sim$  350 Wh/kg) (31-35). Thus, low ED of SC restricted its widespread use, and extensive research efforts are underway to design high ED and high PD. In this context, a device that

integrates SC and LIBS termed HSS was popularized to provide desirable power and energy, as illustrated in **Fig. 2.4**. **Fig. 2.4** delineates the historical timeline and advances in the storage mechanism responsible for energy storage in SCs.

Based on the electrical charge storage mechanism and the materials, SC is categorized into an electric double-layer capacitor (EDC), pseudocapacitors (PC) and hybrid supercapacitors system (HSS). They work on physical charge storage, Faradaic reaction and a combination of physical charge storage and Faradaic reaction for EDC, PC and HSS, respectively, as depicted in **Fig. 2.5**. Most of the time, carbon-based materials (porous carbon and nanocarbon), redox-materials (oxides, sulfides and conducting polymers) and hybrid materials (composites) are widely used for EDC, PC and HSS, respectively, as indicated in **Table 2.1**. The SC system's ED and PD are mostly dependent on electrode materials, electrolyte, and cell-design configuration. The viscosity and ionic conductivity of the electrolyte plays a crucial role in deciding ED and PD. An electrode material plays an essential role in making the SC compact with high performance.

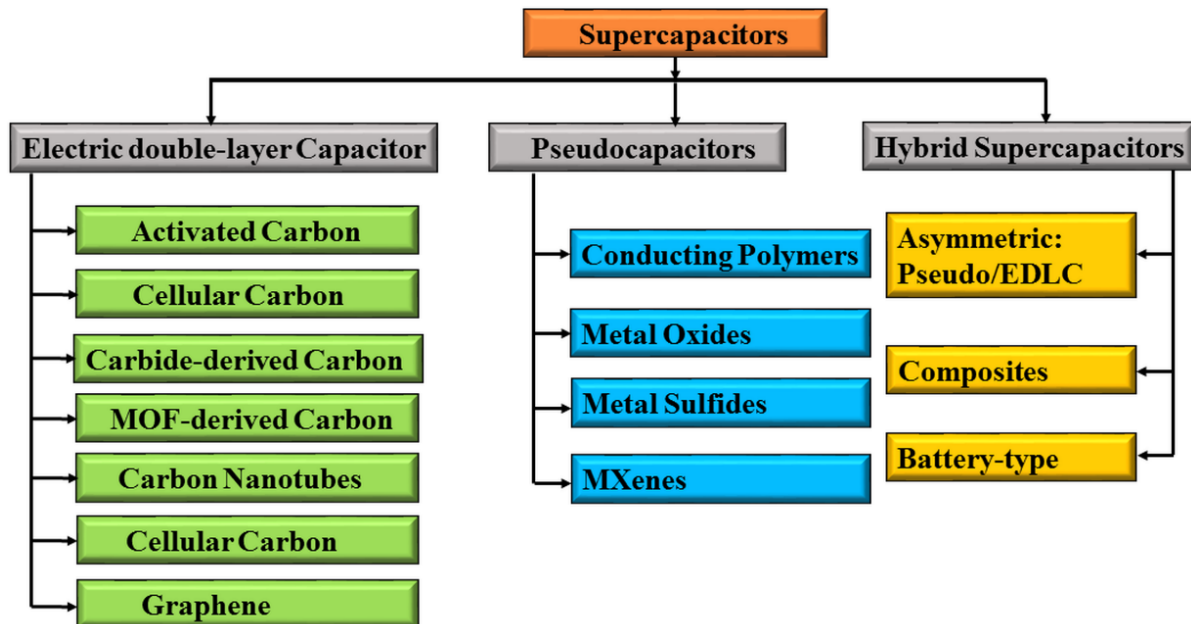


**Fig. 2.5** Classification of SCs based on charge storage mechanism and materials (22).

**Table 2.1:** Comparison of SCs: electrode materials along with charge storage mechanism

Category	Electrode material	Charge storage mechanism
EDC	Activated carbon, porous carbon	Physical adsorption/desorption
PC	Metal oxides, sulphides, nitrides and polymers	Faradaic process
HSS	Anode: PC-type ; Cathode: EDC-type	Anode:Faradaic; Cathode:non-Faradaic
	Hybrid with PC-type and EDC-type	both Faradaic and non-Faradaic
Anode: Battery-type; Cathode:EDC-type	Battery-type: redox; Cathode:non-Faradaic	

### 2.2.1 The organized approach for high energy density SCs

For SCs, porous carbon materials are widely exploited due to controllable porosity, pore-size distribution, electrical conductivity and capacity retention, which meet the requirement of physicochemical properties desirable for it (22, 23). Although activated carbon is used as electrode materials for many decades, its electrical conductivity and capacitance is a prime concern, influencing the electrochemical characteristics of SCs (37-40). In this context, a concept of (i) Nanostructuring-architecture and (ii) doping (N, S, P and B) are the most suitable approaches to improve electrochemical properties (41).

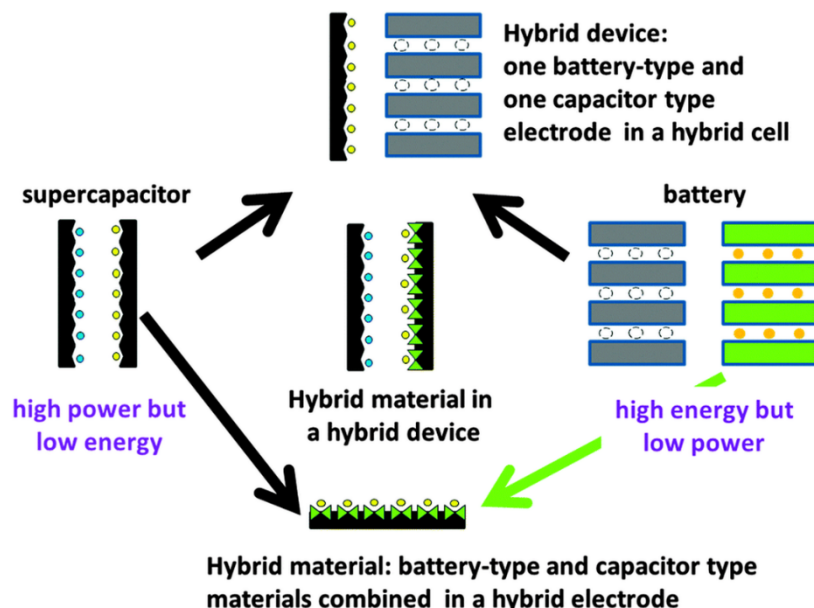


**Fig. 2.6.** Schematic interpretation of different possible hybridization approaches between SCs, LIBS, and materials (27).

Commonly, SCs have high PD but lack in providing sufficient ED. The system's ED is measured as  $0.5CV^2$  where C and V are specific capacitance and voltage window, respectively. To increase

the ED of SCs, either C or V of the system has to be enlarged. To improve C of SCs, materials with nanostructured-architecture or doping could assist in enhancement. However, the V of the system could be enhanced by (i) using appropriate electrolyte and (ii) hybridizing materials. In this context, hybrid supercapacitor gained utmost importance to have an SC system with high ED and PD that could balance power and energy to design an EV. The phenomenon of working of HSS is described in **Fig. 2.6**. It clearly presents on possible hybridization approach by considering (i) hybridizing one capacitor-type electrode with one battery-type electrode (hybrid device approach) and (ii) battery-type and capacitor-type materials combined in a hybrid material (hybrid material approach) (27).

### 2.2.2 Factors affecting the electrochemical performance of SCs

The electrochemical performance of SCs mostly depends on the following factors (27, 34-38):

- (i) SCs shall possess high PD accompanied by adequate ED
- (ii) High electrochemical cyclic stability with high capacity retention
- (iii) Rapid charging-discharging phenomenon
- (iv) Reasonably low self-discharging

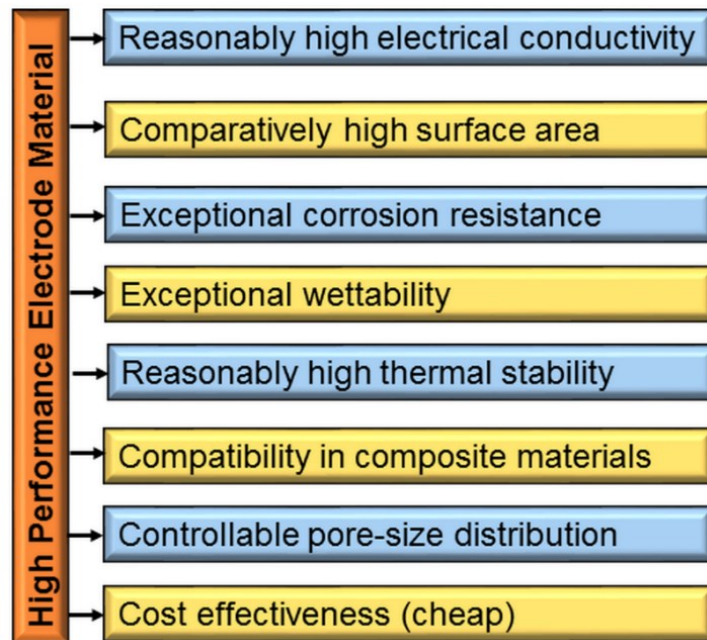


**Fig. 2.7** Illustrating the properties of materials for high-performance electrodes.

To attain the parameters mentioned earlier, an electrode material should possess reasonably high electrical conductivity and corrosion resistance, comparatively high surface area and thermal stability, and compatible pore-size distribution etc., as illustrated in **Fig. 2.7**.

All the physical, chemical, and thermal characteristics of material will have a detrimental effect on SC's electrochemical performance. Especially, nanostructuring, doping and hybridizing approaches are appropriate to ameliorate electrochemical properties. Considering all the factors, quite a fair amount of work has been carried out worldwide to develop a high-performance electrode material described in **Table 2.2**.

A few of the innovative studies that emphasized on supercapacitors are described as follows:

**Frackowiak et al. (2001)** described that with the addition of N-atom in the carbon network, it generates capacitance, which is the sum of EDC due to physical adsorption/desorption at electrode/electrolyte interface and Faradaic reaction-coupled with electron donor characteristics of N-doping (42).

**Han et al. (2018)** presented a simple process of preparing N-doped porous carbon from melamine-added Pueraria powder (NPC) that resulted in significant improvement in capacitance to 250 F/g from 44 F/g (undoped) using 6M KOH and 0.5 A/g (43). Nitrogen incorporated in carbon network result in surface modification with defective-sites with increased electrolyte wettability and functional group participation in pseudocapacitance.

**Mao et al. (2018)** described a process of preparing N-doped carbon for areal capacitance. The N-doped carbon and undoped carbon has shown capacitance of 683 mF/cm<sup>2</sup>, and 330 mF/cm<sup>2</sup>, respectively (44).

**Mostazo-Lopez et al. (2018)** described a process of synthesising N-doped carbon, which exhibited an immense increase in energy density from 5.9 to 6.7 Wh/kg, which gives a clear indication that N-doping leads to improved energy density which might be applicable in practical applications (45).

**Dai et al. (2018)** delineate a process of preparing N-doped porous graphene to apply BMIMBF<sub>4</sub> electrolyte with a higher operating potential of about 3.5 V to achieve 55 Wh/kg and 1800 W/kg (46). A higher voltage window is an added advantage to increase energy density.

**Candelaria et al. (2012)** outline a process of preparing N-doped carbon with excellent wettability. It exhibited a contact angle of almost zero from 102.3, which resulted in an increase in capacitance of two times compared to undoped carbon (47).

**Table 2.2**

Physical and electrochemical properties of various porous N-doped carbon used in SCs

Materials	specific surface area (m <sup>2</sup> /g)	Capacitance (F/g)	ED (Wh/kg)	PD (kW/kg)	Ref.
Zeolite-templated carbon	3600	273	8	98000	48
Carbon nanocages	2407	313	6	22	49
Activated carbon	1580	855	39	23	45
Graphite nanosheets	380	480	83	426	50
Activated carbon	2905	351	39	1	51
Activated carbon	1459	451	11	125	52
Activated carbon	2255	258	5	10	53
Graphene	203	390	55	1800	46
Activated biomass	2650	200	6	8	54
Activated carbon	2723	221	5	2500	55
Graphene aerogel	446	318	60	900	56
Activated carbon	1848	261	4	10	57
Template-derived carbon	2506	337	10	14.4	58

A hybrid capacitor with capacitive-type cathode working on porous carbon with N-doping is widely used for attraction of Li-ion towards electronegativity created due to N-doping in carbon network. The li-storage capacity of various porous carbon materials is described in **Table 2.3**. From the above comprehensive discussion, it can be established that porosity and N-doping are the most favourable approach to advance physicochemical properties such as normalized capacitance, wettability, widened potential window and energy/power density, which have a constructive influence on the overall performance of ECES.

**Table 2.3**

Comparison showing the specific capacity of various porous carbon materials for Li-storage

<b>Materials</b>	<b>Electrolyte</b>	<b>Current density</b>	<b>Window</b>	<b>Capacity</b>	<b>Ref.</b>
		(A/g)	(V)	(mAh/g)	
ERGO	1 M LiPF <sub>6</sub>	1.0	2.0-4.5	133	59
NHCN-2	1M LiPF <sub>6</sub>	1.0	2.0-4.5	123	60
NPC	1M LiPF <sub>6</sub>	0.1	2.0-4.5	83	61
URGO	1M LiPF <sub>6</sub>	0.02	2.0-4.0	35	62
HDMPC	1M LiPF <sub>6</sub>	0.1	2.0-4.5	109	63
PRGO	1M LiPF <sub>6</sub>	0.17	1.5-4.5	171	64
CPAC-5	1M LiPF <sub>6</sub>	0.3	2.0-4.5	135	65
a-NGA	1M LiPF <sub>6</sub>	1.5	2.0 -4.0	52	66
Coconut AC	1M LiPF6	0.1	3.0-4.6	63	67
Corncob-NAC	-	0.4	2.0-4.5	129	68
Egg-carbon	1M LiPF6	0.4	2.0-4.5	128	69
CDC	1M LiPF6	0.1	2.0-4.0	101	70

Considering all the advancements in materials, electrolytes and cell-design, considerable improvements were achieved worldwide, as depicted in **Figure 2.8**. It infers that over the last 3 decades, enhancement in ED nearly 3 and 20 times higher for LIBs and SC, respectively, was achieved. Besides, PD was improved almost 20 to 25 times for both LIBS and SC over 3 decades. **Figure 2.8** clearly indicates that the advancement in materials and materials technology played a crucial role in improving LIBS and SCs, as all the electrochemical properties are mostly dependent on materials. Moreover, the upgradation in materials properties, device making, and fabrication techniques have played imperative part in creating compact appliances with high performance electrode materials.

In the case of HSS, Li-ion based capacitor, which uses battery-type anode and porous carbon-based capacitive-type cathode with widened voltage, is of great interest. However, the charge balancing (mass-based capacity balancing) based on both the streamlined process mechanisms is crucial.

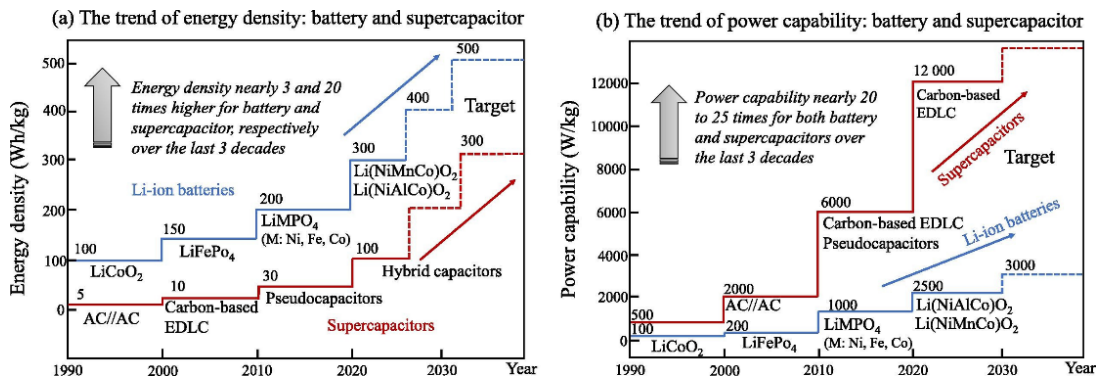


**Fig. 2.8** The ED and PD of LIBS and SCs: (a) trend of ED, (b) trend of PD (36).

### 2.3 Advanced materials for thermal energy storage

#### 2.3.1 Need of PCM in EV

Sustainable development paralleled with mitigating environmental changes has forced humankind to explore green energy storage system (1-7). To substitute the internal combustion engine in the automobile manufacturing sector, a network of sustainable and renewable sources is mostly sought (71). Under the pressure of limitations of energy sources and environmental issues, the electrified automobiles are on first choice (72). In a quest to it, electric vehicles (EV) are the most promising candidate for generating clean energy, as most of the energy-related activity in the world is dependent on FF (12-17). The EV system is expected to have a market rise of 15 to 20 % in the next ten years, and it consistently dominates the automobile energy sector along with its thermal management system-battery (TMSB), as shown in **Fig. 2.9** (72). Owing to high energy density (ED), massive mileage and other advantages, Li-ion based battery system (LIBS) attracted immensely to find its place in EV for energy storage/release (12-17). LIBS is considered as the heart of the EV system. Besides, it will not release harmful greenhouse gases, which are sources of environmental deterioration, global warming and biodiversity degradation. LIBS is considered the accurately suitable, safest, and only option for EV as it delivers the highest ED compared to other battery systems such as Nickel-Cadmium, Nickel-metal hydride, and Lead-acid, and so on (74,75). Unfortunately, LIBS's performance, life cycles,

and safety are indeterminately dependent on operating temperature, discharge rate, external climatic conditions, and internal heat generation (76-78).

**Fig. 2.9** (a) Global demand for EV system for next decade (72) and (b) Year-wise statistics of journal papers on TMSB (73).

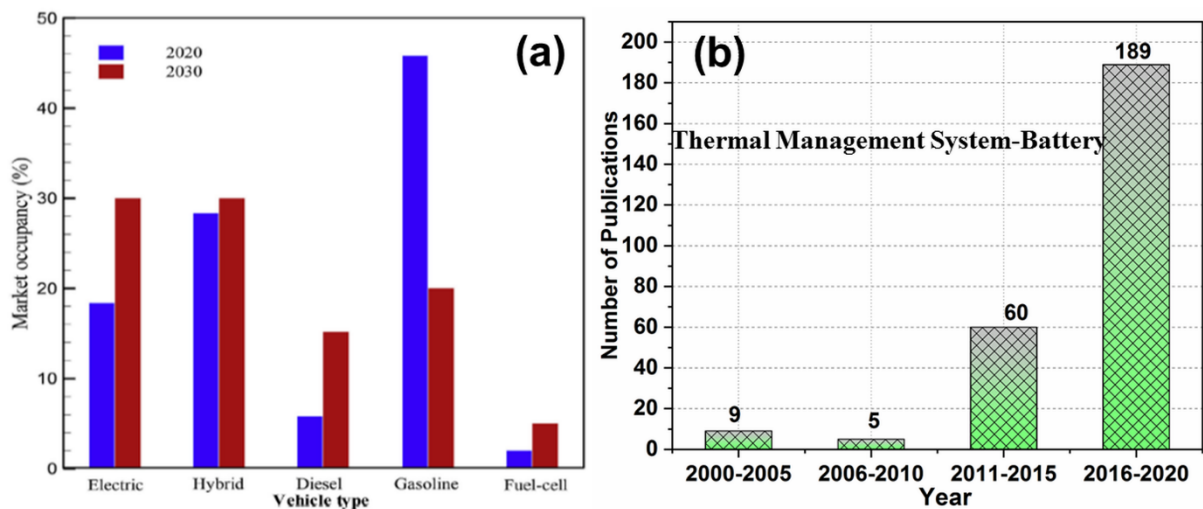


**Fig. 2.10** Illustration of TRP initiation and interpretation of temperature-dependent chain reaction (84-87).

At high current density, the LIBS produces tremendous heat during acceleration, long-discharge cycle and fast charging. Then, overheating, explosion, thermal abuse and safety risk become severe as they lead to abrupt rupture of LIBS cell. Significantly, the temperature has a catastrophic impact on capacity fade (77, 79). To achieve high ED and more life cycles, a sustainable environment with isothermal temperature must be maintained. Otherwise, the burst in temperature could lead to a thermal runaway phenomenon (TRP) by generating mechanical, electrical and thermal abuse (80-83). In a TRP state, the LIBS catches fire due to cascading of excess heat propagation from a damaged cell to its adjacent cell, as indicated in **Fig.2.10**.

Considering a LIBS, in the process of initiation of TRP, the solid-electrolyte interface layer decomposition, electrolyte breakdown, separator melt (short circuit), cathode decomposition, and thermal instability arises in the temperature range of 80-85 °C, 100-120 °C, 120-130°C, 130-150°C, and 150-180 °C, respectively (87-91). TRP trigger within few seconds with tremendous heat production of 70 KW/ m<sup>3</sup>, 200 KW/ m<sup>3</sup>, 360 KW/m<sup>3</sup> at 1C, 3C and 5C, respectively (92). Therefore, a material, which can trap as-generated heat and maintain

isothermal uniformity, is essential to pause TRP. Subsequently, a novel TMSB is looked-for to avert LIBS from TRP caused by excess heat generation.

To suppress the abrupt rise in LIBS's temperature, the processes of active and passive cooling systems are adopted, as illustrated in **Fig.2.11**. Among all, air-cooling, liquid cooling, heat pipe cooling, thermoelectric cooling are widely used (93-106). Nevertheless, an effective thermal management system is urgently required to overcome the traditional cooling system's disadvantages.

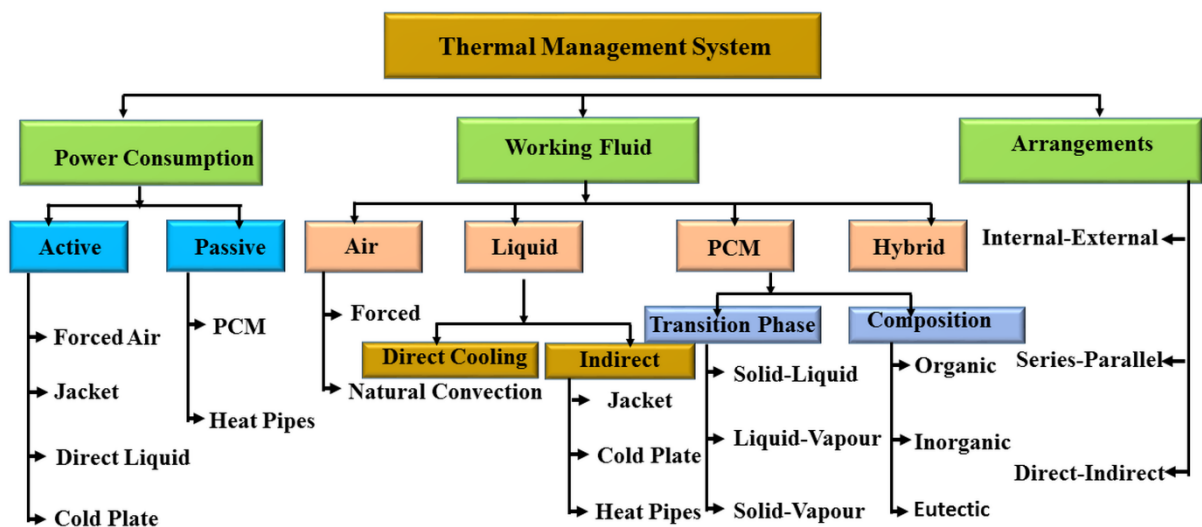
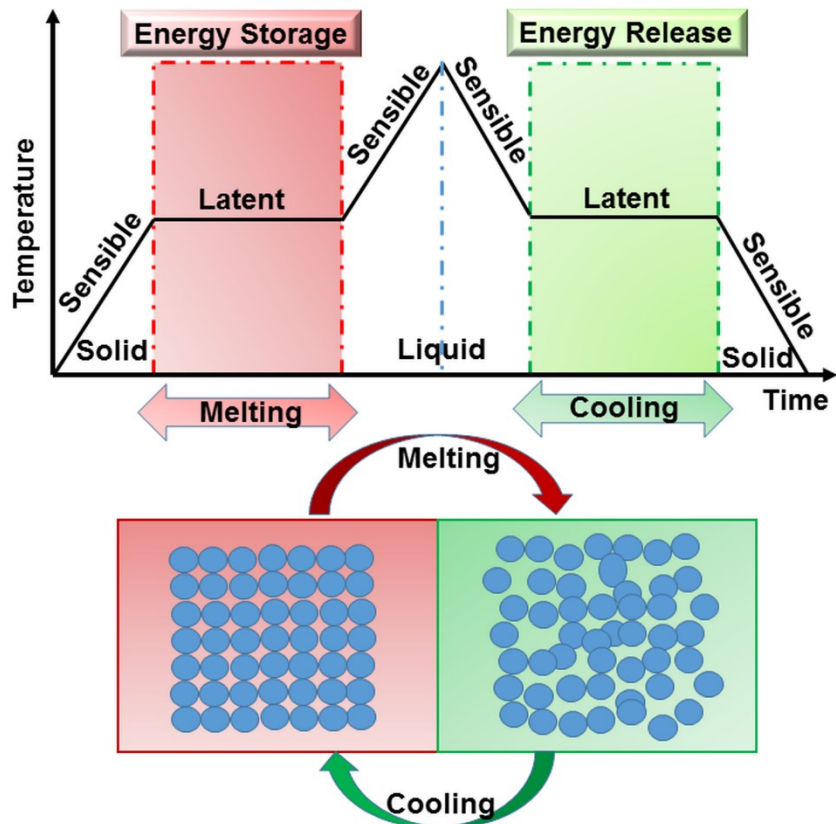


**Fig.2.11** Classification of TMSB.

### 2.3.2 Materials for TMSB: PCM and fillers

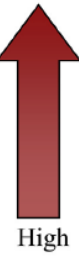
Various kinds of cooling systems are adopted for TMSB, as illustrated in **Fig.2.11**. Currently, a PCM-based materials drawn a considerable market to maintain uniform temperature distribution in LIBS as an alternative to traditional cooling methods (96-106).

To intensify the effective means of storing heat, a PCM composition with appropriate phase transition is essential, as described in **Fig.2.12**, in which the PCM will absorb and release heat during melting and cooling, respectively. The existing PCM materials may not handle the heat dissipation solely as they possess significantly less thermal conductivity (96,98, 99,102,103,106, 107). Based on PCM materials' availability, they are categorized into various sets as described in **Fig.2.11**.



**Fig.2.12** Illustration of underlying principle involved in heat storage/release by PCM.

In LIBS, maintaining temperature distribution below 60 °C is crucial to suppress TRP (84-87, 96-106). To this point, LIBS exhibit maximum cycle life and superior energy storage capacity in the temperature range of 25-40 °C and 15-24 °C, respectively, as shown in **Fig.2.13** (87). Therefore, a PCM system with phase transition falls in a range of 40-50 °C with suitable latent heat and it is considered as a promising candidate for temperature controlling in TMSB.

Battery cell temperature	Cause	Leads to	Effect
High 	Electrolyte decomposition	Irreversible lithium loss	Capacity fade
	Continuous side reactions at low rate	Impedance Rise	Power fade
	Decrease of accessible anode surface for Li-ion intercalation		
	Decomposition of binder	Loss of mechanical stability	Capacity fade
25 °C – 40 °C	Maximum cycle life		
15 °C – 24 °C	Superior energy Storage capacity		
Low 	Lithium plating	Irreversible loss of lithium	Capacity/ power fade
	Electrolyte decomposition	Electrolyte loss	

**Fig.2.13** Influence of temperature on the performance of LIBS (87).

Generally, the category of fatty acids with a general formula with  $\text{CH}_3(\text{CH}_2)_{2n}\text{COOH}$  is widely considered renewable PCMs for latent heat storage due to their remarkable thermodynamic and kinetic characteristics. The exceptional properties such as latent heat of fusion, supercooling, thermal and chemical stability, minimum volume change, and the broad range of melting point made them appropriate for EV (108-110). Unlike paraffin-based wax, each fatty acids have distinct thermal properties, but their melting points and latent heat increase moderately as the number of carbon atoms in the fatty acid molecule increases, as indicated in **Table.2.4**. The fatty acids class possesses phase transition temperature and latent heat of fusion in the range of 5-70 °C and 45-210 kJ/kg, respectively. The well-known fatty acids such as capric acid, lauric acid, pentadecanoic acid, myristic acid, palmitic acid and stearic acids are widely studied for TES. Widened phase transition temperature with reasonable high latent heat makes them ideal for a plethora of applications depending on the requirement. To adjust a phase transition, a composition of multiple-fatty acids called eutectics has a significant role in suiting exact temperature. Eutectic PCM could assist in developing an advanced TES for energy absorbing/releasing with suitable temperature and appropriate latent heat of fusion.

**Table 2.4:** Thermophysical properties of some fatty acids (111)

Fatty acid	Transition Temp. (°C)	Latent heat (kJ/kg)
Capric acid (12-C)	30.1	158.0
Lauric acid (12-C)	43.7	210.8
Pentadecanoic acid (15-C)	52.5	158.6
Myristic acid (14-C)	52.2	190
Palmitic acid (16-C)	54.1	183
Stearic acid (18-C)	64.5	196

Despite the phase transition temperature, thermal conductivity plays a crucial role in heat dissipation by increasing the heat transfer rate. However, they possess very less thermal conductivity. The low thermal conductivity of fatty acids is a significant concern in applying them for practical applications. In such cases, additives are included in the PCM to ameliorate thermal conductivity, as illustrated in **Fig.2.14**. The addition of nanoadditives to the PCM could be an appropriate option to enhance thermal conductivity and heat transfer. However, the category of additives called ‘nanomaterials’ are suitable additives owing to their exceptional thermo-physical characteristics (111-114). These nanomaterials possess numerous advantages over bulk materials like high surface-to-volume ratio, high porosity, unique physicochemical characteristics. Besides, they exhibit increased electrical conductivity, improved magnetic coercivity, improved hardness and toughness, augmented quantum efficiency, better catalytic activity and increased thermal transport etc.

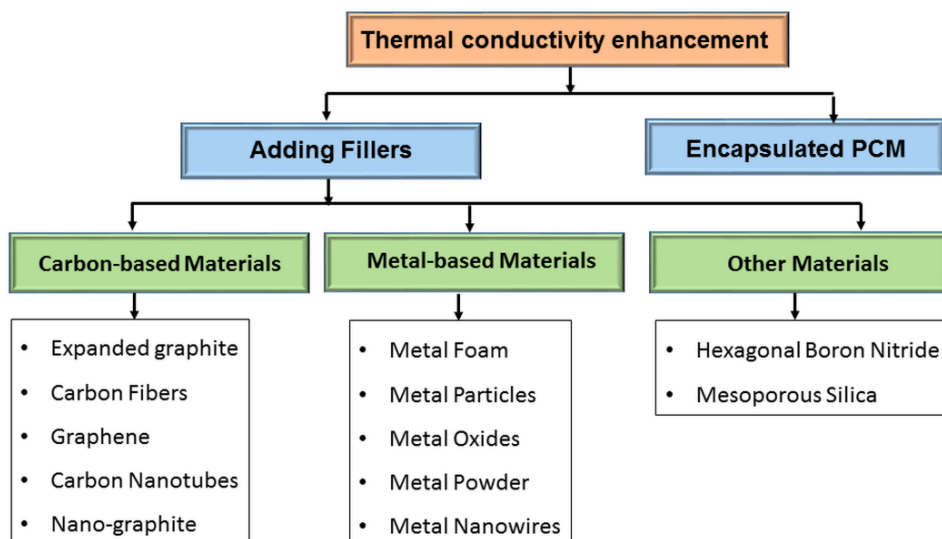


**Fig.2.14** Illustration of various strategies to improve the thermal conductivity of PCM.

The light-weight and high porosity of these materials make them unique and suitable for a plethora of applications. Similarly, having better thermal conductivity as compared to bulk materials makes them the right candidate to design a higher heat transfer system. The nanomaterials (based on dimensionality) such as 1-D, 2-D and 3-D material enhances thermal conductivity (115-119). The wide varieties of nanomaterials like CuO, h-BN, Ag, SiO<sub>2</sub>, TiO<sub>2</sub>, Fe, Cu, Al<sub>2</sub>O<sub>3</sub>, Co<sub>3</sub>O<sub>4</sub>, SiC, AlN, Fe<sub>3</sub>O<sub>4</sub>, carbon nanotubes and graphene are used in the process of augmenting thermal conductivity of PCM as shown in **Table 2.5**.

Among all nanoadditives widely exploited for thermal conductivity enhancement, carbon-based nanostructures (graphene, carbon nanotubes, expanded graphite, carbon onion and carbon nanofibers) have attracted tremendously due to their exceptional thermal conductivity and relatively low density (111). The inherent mechanical, thermal and chemical characteristics of carbon nanomaterials make them a right candidate as filler. The easy processing of carbon nanomaterials with shapes and dimensionality are the added advantages over other nanomaterials. In addition, nanocarbon materials are chemically inert and least corrosive to the PCM containers. Especially, 2D-structured carbon allotrope with atomically thin called 'graphene' is of huge interest, as it possesses thermal conductivity of 3000-5000 W/m.K (112-128). The ballistic phonon transport in graphitized and crystalline materials is responsible for high thermal transport.

Considering all the TES materials' advancements, carbon-based materials are dominant over other materials due to exceptional thermal conductivity, low toxicity, chemical stability, and compatibility with the storage system (111).

**Table 2.5:** Comparison of thermal conductivity with different nanoadditives

PCM	Nanoadditive	Fraction (wt. %)	Enhancement (%)	Ref.
Soy wax	Carbon nanofiber and CNT	10	145	129
PEG and silica gel	AlN	30	199	130
Palmitic acid	Carbon nanotubes	1	150	131
Lauric acid	Graphene platelets	1 vol %	227	132
Paraffin	Nanographite	10	740	133
Adipic and sebacic acid	Graphite	0.5	1190	134
Bees wax	Graphene platelets	0.3	1156	135
Erythritol	Carbon fiber	10	560	136
Erythritol	Ni particles	17 vol%	290	137
Paraffin	Fe <sub>3</sub> O <sub>4</sub>	20	160	138
n-octadecane	Mesoporous silica	5	106	139
PEG	Al <sub>2</sub> O <sub>3</sub>	3	150	140
1-tetradecanol	Ag nanowires	62.73	456	141
Stearic and benzamide	Expanded graphite	12	1230	142
Palmitic and capric acid	Diatomite	5	125	143
Myristic and stearic acid	N-doped porous carbon	12	117	144
Myristic and capric acid	SiO <sub>2</sub>	1.5	142	145

A few of the eutectic PCM loaded with filler based systems are described as follows:

**Guixiang et al. (2019)** outlines the process of determination of eutectic mixture to derive the exact composition of stearic acid and benzamide (SA-BA) by performing differential scanning calorimetry. The microwave-assisted expanded graphite (MEG) was used to improve thermal

conductivity. MEG/SA-BA exhibited a thermal conductivity improvement of 1230 %. Thermal stability and thermal cycle reliability test were demonstrated (142).

**Atinifu et al. (2018)** demonstrated a novel process for the generation of porous carbon through in-situ (NPC) and post-synthesis route (MGC) loaded eutectic mixture of myristic acid-stearic acid (M-S). NPC/M-S and MGC/M-S exhibited an increase in thermal conductivity of 117 % and 74 %, respectively. The porous carbon acted as a conducting agent, and shape-stabilizer (144).

**Kahwaji et al. (2018)** presented a process of deriving data on molar masses (mass-fraction), transition temperatures, latent heats of fusion and heat capacities of 15 types of fatty acid phase change materials (PCMs), which are useful in designing a eutectic organic PCM (110). They considered a process of phase equilibrium theory and the laws of thermodynamics.

**Kahwaji et al. (2018)** demonstrated a process of making the datasheet consisting of molar masses, transition temperatures, latent heat of fusion and heat capacities of various fatty acids and their eutectics. It delineates an Excel sheet that consists of all the thermal properties of organic PCM (146).

The thorough literature on materials for ECES and TES reveals that there exist much scope in improving the performances of appliances by obtaining the superior materials characteristics. In this context, (i) the porous carbon based functional nanocomposite materials with superior capacitive energy storage via controlled porous structure and (ii) Nanocarbon-loaded eutectic PCM with enhanced thermal transport via nanocarbon loading have widely attracted to develop automotive materials required for the application in EV sector. In line with this, the functional nanocomposites based on nanocarbon loading were developed to obtain superior ECES and TES characteristics to make them as a right candidate for EV application.

## 2.4 References

1. D.A. Lashof, D.R. Ahuja, Relative contributions of greenhouse gas emissions to global warming, *Nature* 344 (1990) 529-531.
2. S. Chu, A. Majumdar, Opportunities and challenges for a sustainable energy future, *Nature* 488 (2012) 294-303.
3. D.G. Nocera, Living healthy on a dying planet, *Chem. Soc. Rev.* 38 (2009) 13-15.
4. A. Hagfeldt, G. Boschloo, L. Sun, L. Kloo, H. Pettersson, Dye-sensitized solar cells, *Chem. Rev.* 110 (2010) 6595-6663.
5. A.C. Dillon, Carbon nanotubes for photoconversion and electrical energy storage, *Chem. Rev.* 110 (2010) 6856-6872.
6. E.V. Kondratenko, G. Mul, J. Baltrusaitis, G.O. Larrazabal, J. Perez-Ramirez, Status and perspectives of CO<sub>2</sub> conversion into fuels and chemicals by catalytic, photocatalytic and electrocatalytic processes, *Energy Environ. Sci.* 6 (2013) 3112-3135.
7. K. Christopher, R. Dimitrios, A Review on exergy comparison of hydrogen production methods from renewable energy sources, *Energy Environ. Sci.* 5 (2012) 6640-6651.
8. T.R. Cook, D.K. Dogutan, S.Y. Reece, Y. Surendranath, T.S. Teets, D.G. Nocera, Solar energy supply and storage for the legacy and nonlegacy worlds, *Chem. Rev.* 110 (2010) 6474-6502.
9. S. O. Amrouche, D. Rekioua, T. Rekioua, S. Bacha, Overview of energy storage in renewable energy systems, *Int. J. Hydrogen Energy* 41 (45) (2016) 20914-20927.
10. A. Afif, N. Radenahmad, Q. Cheok, S. Shams, J.H. Kim, A.K. Azad, Ammonia-fed fuel cells: a comprehensive review, *Renew. Sustain. Energy Rev.* 60 (2016) 822-835.
11. I. Dincer, M. Rosen, *Thermal energy storage: systems and applications*; John Wiley & Sons: Hoboken, NJ, USA, 2010.
12. S. Amjad, S. Neelakrishnan, R. Rudramoorthy, Review of design considerations and technological challenges for successful development and deployment of plug-in hybrid electric vehicles, *Renew. Sustain. Energy Rev.* 14 (2010) 1104-1110.
13. M. Wada, Research and development of electric vehicles for clean transportation, *J. Environ. Sci.* 21 (2009) 745-749.
14. S.J. Skerlos, J.J. Winebrake, Targeting plug-in hybrid electric vehicle policies to increase social benefits, *Energy Policy* 38 (2010) 705-708.
15. P. Baptista, M. Tomás, C. Silva, Plug-in hybrid fuel cell vehicles market penetration scenarios, *Int. J. Hydrogen Energy* 35 (2010) 10024-10030.

16. J. Dong, C. Liu, Z. Lin, Charging infrastructure planning for promoting battery electric vehicles: an activity-based approach using multiday travel data, *Transport. Res. Part C: Emerg. Technol.* 38 (2014) 44-55.
17. A. Barré, B. Deguilhem, S. Grolleau, M. Gérard, F. Suard, D. Riu, A review on lithium-ion battery ageing mechanisms and estimations for automotive applications, *J. Power Sources* 241 (2013) 680-689.
18. J. Jaguemont, N. Omar, P. Van den Bossche, J. Mierlo, Phase-change materials (PCM) for automotive applications: A review, *Appl. Therm. Eng.* 132 (2018) 308-320.
19. P. Simon, Y. Gogotsi. Capacitive energy storage in nanostructured carbon electrolyte systems, *Accounts Chem. Res.* 46 (5) (2013) 1094-1103.
20. M. Inagaki, H. Konno, O. Tanaike, Carbon materials for electrochemical capacitors, *J. Power Sources* 195 (24) (2010) 7880-7903.
21. Z. Yang, J. Tian, Z. Yin, C. Cui, W. Qian, F. Wei, Carbon nanotube- and graphene-based nanomaterials and applications in high-voltage supercapacitor: A review, *Carbon* 141 (2019) 467-480.
22. S. Najib, E. Erdem, Current progress achieved in novel materials for supercapacitor electrodes: mini review, *Nanoscale Adv.*, 1 (2019) 2817-2827.
23. J. Yin, W. Zhang, N. A. Alhebshi, N. Salah, H. N. Alshareef, Synthesis strategies of porous carbon for supercapacitor applications, *Small Methods* (2020) 1900853 (31pp).
24. A. Burke, Ultracapacitors: why, how, and where is the technology, *J. Power Sources* 91(1) (2000) 37-50.
25. S. Zhang, N. Pan, Supercapacitors performance evaluation, *Adv. Energy Mater.* 5(2015) 1401401.
26. Y. Shao, M. F. El-Kady, J. Sun, Y. Li, Q. Zhang, M. Zhu, H. Wang, B. Dunn, R. B. Kaner, Design and mechanisms of asymmetric supercapacitors, *Chem. Rev.* 118 (2018) 9233-9280.
27. D. P. Dubal, O. Ayyad, V. Ruiz, P. G. Romero, Hybrid energy storage: the merging of battery and supercapacitor chemistries, *Chem. Soc. Rev.*, 44 (2015) 1777-1790.
28. P. Simon, Y. Gogotsi, B. Dunn, Where do batteries end and supercapacitors begin?, *Science* 343 (2014) 1210-1211.
29. <https://www.maximizemarketresearch.com/market-report/global-SC-market/27055/>.

30. K.V.G. Raghavendra, R. Vinoth, K. Zeb, C.V.V.M. Gopi, S. Sambasivam, M. R. Kummara, I. M. Obaidatd, H. J. Kim, An intuitive review of supercapacitors with recent progress and novel device applications, *J Energy Storage* 31 (2020) 101652 (34pp).

31. B. Li, F. Dai, Q.F. Xiao, L. Yang, J.M. Shen, C.M. Zhang, M. Cai, Nitrogen-doped activated carbon for a high energy hybrid supercapacitor, *Energy Environ. Sci.* 9 (2016) 102-106.

32. H.W. Wang, Y. Zhang, H.X. Ang, Y.Q. Zhang, H.T. Tan, Y.F. Zhang, Y.Y. Guo, J.B. Franklin, X.L. Wu, M. Srinivasan, H.J. Fan, Q.Y. Yan, A high-energy lithium-ion capacitor by integration of a 3D interconnected titanium carbide nanoparticle chain anode with a pyridine-derived porous nitrogen-doped carbon cathode, *Adv. Funct. Mater.* 26 (2016) 3028-3093.

33. X. Ye, Y. Zhu, H. Jiang, L. Wang, P. Zhao, Z. Yue, Z. Wan, C. Jia, A rapid heat pressing strategy to prepare fluffy reduced graphene oxide films with meso/macropores for high-performance supercapacitors, *Chem. Eng. J.* 361 (2019) 1437-1450.

34. Y. Yoo, G.D. Park, Y.C. Kang, Carbon microspheres with micro- and mesopores synthesized via spray pyrolysis for high-energy-density, electrical-double-layer capacitors, *Chem. Eng. J.* 365 (2019) 193-200.

35. B. Li, F. Dai, Q.F. Xiao, L. Yang, J.M. Shen, C.M. Zhang, M. Cai, Activated carbon from biomass transfer for high-energy density lithium-ion supercapacitors, *Adv. Energy Mater.* 6 (2016) 1600802.

36. J. Zhao, A. F. Burke, Review on supercapacitors: technologies and performance evaluation, *J Energy Chemistry* 59 (2021) 276-291.

37. X. Wang, L. Liu, Z. Niu, Carbon-based materials for lithium-ion capacitors Mater, *Chem. Front.*, 3 (2019) 1265-1279.

38. C. Li, X. Zhang, C. Sun, K. Wang, X. Sun, Y. Ma, Recent progress of graphene-based materials in lithium-ion capacitors, *J. Phys. D: Appl. Phys.* 52 (2019) 143001 (19pp).

39. A. Banerjee, K.K. Upadhyay, D. Puthusseri, V. Aravindan, S. Madhavi, S. Ogale, MOF-derived crumpled-sheet-assembled perforated carbon cuboids as highly effective cathode active materials for ultra-high energy density Li-ion hybrid electrochemical capacitors (Li-HECs), *Nanoscale* 6 (8) (2014) 4387-4394.

40. X. Xu, Y. Cui, J. Shi, W. Liu, S. Chen, X. Wang, H. Wang, Sorghum core-derived carbon sheets as electrodes for a lithium-ion capacitor, *RSC Adv.* 7 (28) (2017) 17178-17183.

41. Q. Abbas, R. Raza, I. Shabbir, A.G. Olabi, Heteroatom doped high porosity carbon nanomaterials as electrodes for energy storage in electrochemical capacitors: A review, *J Sci-Adv Mater Dev* 4 (2019) 341-352.
42. E. Frackowiak, F. Beguin, Carbon materials for the electrochemical storage of energy in capacitors, *Carbon* 39 (2001) 937-950.
43. X. Han, H. Jiang, Y. Zhou, W. Hong, Y. Zhou, P. Gao, R. Ding, E. Liu, A high performance nitrogen-doped porous activated carbon for supercapacitor derived from pueraria, *J. Alloy. Compd.* 744 (2018) 544-551.
44. Z. Mao, S. Zhao, J. Wang, Y. Zeng, X. Lu, Y. Tong, Facile synthesis of nitrogen doped porous carbon as robust electrode for supercapacitors, *Mater. Res. Bull.* 101 (2018) 140-145.
45. M.J. Mostazo-Lopez, R. Ruiz-Rosas, A. Castro-Muñiz, H. Nishihara, T. Kyotani, E. Morallon, D. Cazorla-Amoros, Ultraporous nitrogen-doped zeolite-templated carbon for high power density aqueous-based supercapacitors, *Carbon* 129 (2018) 510-519.
46. S. Dai, Z. Liu, B. Zhao, J. Zeng, H. Hu, Q. Zhang, D. Chen, C. Qu, D. Dang, M. Liu, A high-performance supercapacitor electrode based on N-doped porous graphene, *J. Power Sources* 387 (2018) 43-48.
47. S.L. Candelaria, B.B. Garcia, D. Liu, G. Cao, Nitrogen modification of highly porous carbon for improved supercapacitor performance, *J. Mater. Chem.* 22 (2012) 9884-9889.
48. J. Zhao, H. Lai, Z. Lyu, Y. Jiang, K. Xie, X. Wang, Q. Wu, L. Yang, Z. Jin, Y. Ma, J. Liu, Z. Hu, Hydrophilic hierarchical nitrogen-doped carbon nanocages for ultrahigh supercapacitive performance, *Adv. Mater.* 27 (2015) 3541-3545.
49. T. Lin, I.-W. Chen, F. Liu, C. Yang, H. Bi, F. Xu, F. Huang, Nitrogen-doped mesoporous carbon of extraordinary capacitance for electrochemical energy storage, *Science* 350 (2015) 1508-1513.
50. M.S. Javed, S.S.A. Shah, T. Najam, M.K. Aslam, J. Li, S. Hussain, M.A. Ahmad, M. Ashfaq, R. Raza, W. Mai, Synthesis of mesoporous defective graphene-nanosheets in a space-confined self -assembled nanoreactor: highly efficient capacitive energy storage, *Electrochim. Acta* 305 (2019) 517-527.
51. K. Zou, Y. Deng, J. Chen, Y. Qian, Y. Yang, Y. Li, G. Chen, Hierarchically porous nitrogen-doped carbon derived from the activation of agriculture waste by potassium hydroxide and urea for high-performance supercapacitors, *J. Power Sources* 378 (2018) 579-588.

52. G. Wang, J. Zhang, S. Kuang, J. Zhou, W. Xing, S. Zhuo, Nitrogen-doped hierarchical porous carbon as an efficient electrode material for supercapacitors, *Electrochim. Acta* 153 (2015) 273-279.

53. M. Sevilla, N. Diez, G.A. Ferrero, A.B. Fuertes, Sustainable supercapacitor electrodes produced by the activation of biomass with sodium thiosulfate, *Energy Storage Mater.* 18 (2019) 356-365.

54. M. Sevilla, N. Diez, G.A. Ferrero, A.B. Fuertes, Sustainable supercapacitor electrodes produced by the activation of biomass with sodium thiosulfate, *Energy Storage Mater.* 18 (2019) 356-365.

55. P. Song, X. Shen, W. He, L. Kong, X. He, Z. Ji, A. Yuan, G. Zhu, N. Li, Protein-derived nitrogen doped hierarchically porous carbon as electrode material for supercapacitors, *J. Mater. Sci. Mater. Electron.* 29 (2018) 12206-12215.

56. P. Xu, Q. Gao, L. Ma, Z. Li, H. Zhang, H. Xiao, X. Liang, T. Zhang, X. Tian, C. Liu, A high surface area N-doped holey graphene aerogel with low charge transfer resistance as high performance electrode of non-flammable thermostable supercapacitor, *Carbon* 149 (2019) 452-461.

57. J. Zhou, Z. Zhang, W. Xing, J. Yu, G. Han, W. Si, S. Zhuo, Nitrogen-doped hierarchical porous carbon materials prepared from meta-aminophenol formaldehyde resin for supercapacitor with high rate performance, *Electrochim. Acta* 153 (2015) 68-75.

58. M. Chen, H. Xuan, X. Zheng, J. Liu, X. Dong, F. Xi, N-doped mesoporous carbon by a hard-template strategy associated with chemical activation and its enhanced supercapacitance performance, *Electrochim. Acta* 238 (2017) 269-277.

59. F. Tu, S. Liu, T. Wu, G. Jin, C. Pan, Porous graphene as cathode material for lithium ion capacitor with high electrochemical performance, *Powder Technol.* 253 (2014) 580-583.

60. C. Li, X. Zhang, K. Wang, X. Sun, Y. Ma, High-power and long-life lithium-ion capacitors constructed from N-doped hierarchical carbon nanolayer cathode and mesoporous graphene anode, *Carbon* 140 (2018) 237-248.

61. Y. Cui, W. Liu, Y. Lyu, Y. Zhang, H. Wang, Y. Liu, D. Li, All-carbon lithium capacitor based on salt crystal-templed, N-doped porous carbon electrodes with superior energy storage, *J. Mater. Chem. A* 6 (2018) 18276-18285.

62. M.H. Ryou, J.K Jin, J. Kim, J.W. Choi, Functionaized graphene for high performance lithium ion capacitor, *Chem Sus Chem* 5 (2012) 2328-2333.

63. J. Niu, R. Shao, M. Liu, J. Liang, Z. Zhang, M. Dou, Y. Huang, F. Wang, Porous carbon electrodes with battery-capacitive storage features for high performance Li-ion capacitor, *Energy Stor. Mater.* 12 (2018) 145-152.

64. D. P. Dubal, G. R. Pedro, All nanocarbon Li-ion capacitor with high energy and high power density, *Mater. Today Energy* 8 (2018) 109-117.

65. Q. Lu, B. Lu, M. Chen, X. Wang, T. Xing, M. Liu, X. Wang, Porous activated carbon derived from Chinese-chive for high energy hybrid lithium-ion capacitor, *J Power Sources* 398 (2018) 128-136.

66. Q. Fan, M. Yang, Q. Meng, B. Cao, Y. Yu, Activated nitrogen-doped graphene-based aerogel composites as cathode materials for high energy density lithium-ion supercapacitor, *J. Electrochem. Soc.* 163 (8) (2016) A1736-A1742.

67. A. Jain, V. Aravindan, S. Jayaraman, P.S. Kumar, R. Balasubramanian, S. Ramakrishna, S. Madhavi, M.P. Srinivasan, Activated carbons derived from coconut shells as high energy density cathode material for Li-ion capacitors, *Sci. Rep.* 3 (2013) 3002 (6pp).

68. B. Li, F. Dai, Q.F. Xiao, L. Yang, J.M. Shen, C.M. Zhang, M. Cai, Nitrogen-doped activated carbon for a high energy hybrid supercapacitor, *Energy Environ. Sci.* 9 (1) (2016) 102-106.

69. B. Li, F. Dai, Q.F. Xiao, L. Yang, J.M. Shen, C.M. Zhang, M. Cai, Activated carbon from biomass transfer for high-energy density lithium-ion supercapacitors, *Adv Energy Mater* 6 (18) (2016) 1600802.

70. H. Li, J. Chen, B. Yang, K. Wang, X. Zhang, T. Zhang, L. Zhang, W. Liu, X. Yan, Constructing surface-driven lithium ion storage structure for high performance hybrid capacitor, *Electrochim. Acta* 299 (2019) 163-172.

71. R.D.O. Neto, C.A.R. Sotomonte, C.J.R. Coronado, M.A.R. Nascimento, Technical and economic analyses of waste heat energy recovery from internal combustion engines by the organic Rankine cycle, *Energy Convers. Manage.* 129 (2016) 168-179.

72. T. Zhang, C. Gao, Q. Gao, G. Wang, M. Liu, Y. Guo, C. Xiao, Y.Y. Yan, Status and development of electric vehicle integrated thermal management from BTM to HVAC, *Appl. Therm. Eng.* 88 (2015) 398-409.

73. P.R. Tete, M. M. Gupta, S.S. Joshi, Developments in battery thermal management systems for electric vehicles: A technical review, *J Energy Storage* 35 (2021) 102255 (63pp).

74. P. Kumar, D. Chaudhary, P. Varshney, U. Varshney, S. M. Yahya, Y. Rafat, Critical review on battery thermal management and role of nanomaterial in heat transfer enhancement for electrical vehicle application, *J Energy Storage* 32 (2020) 102003 (25pp).

75. T. Placke, R. Kloepsch, S. Dühnen, M. Winter, Lithium ion, lithium metal, and alternative rechargeable battery technologies: the odyssey for high energy density, *J. Solid State Electrochem.* 21 (2017) 1939-1964.

76. P. Ramadass, B. Haran, R. White, B.N. Popov, Capacity fade of Sony 18650 cells cycled at elevated temperatures: Part I. cycling performance, *J Power Sources* 112 (2002) 606-613.

77. T.M. Bandhauer, S. Garimella, T.F. Fuller, A critical review of thermal issues in lithium-ion batteries, *J. Electrochem. Soc.* 158 (2011) R1–R25.

78. X.M. Xu, R. He, Review on the heat dissipation performance of battery pack with different structures and operation conditions, *Renew. Sustain. Energy Rev.* 29 (2014) 301-315.

79. J.R. Belt, C.D. Ho, T.J. Miller, M.A. Habib, T.Q. Duong, The effect of temperature on capacity and power in cycled lithium ion batteries, *J. Power Sources* 142 (2005) 354-360.

80. Y. Zeng, K. Wu, D. Wang, Z. Wang, L. Chen, Overcharge investigation of lithium ion polymer batteries, *J. Power Sources* 160 (2006) 1302-1307.

81. J. Lamb, C.J. Orendorff, L.A.M. Steele, S.W. Spangler, Failure propagation in multi-cell lithium ion batteries, *J. Power Sources* 283 (2015) 517-523.

82. D. Doughty, E.P. Roth, A general discussion of Li Ion battery safety, *Electrochem.Soc. Interface* 21 (2012) 37-44.

83. D.P. Abraham, E.P. Roth, R. Kostecki, K. McCarthy, S. MacLaren, D.H. Doughty, Diagnostic examination of thermally abused high-power lithium-ion cells, *J. Power Sources* 161 (2006) 648-657.

84. X. Feng, M. Ouyang, X. Liu, L. Lu, Y. Xia, X. He, Thermal runaway mechanism of lithium ion battery for electric vehicles: A review, *Energy Storage Mater* 10 (2018) 246-267.

85. R. Spotnitz, J. Franklin, Abuse behavior of high-power, lithium-ion cells, *J. Power Sources* 113 (1) (2003) 81-100.

86. Q. Wang, P. Ping, X. Zhao, G. Chu, J. Sun, C. Chen, Thermal runaway caused fire and explosion of lithium ion battery, *J. Power Sources* 208 (2012) 210-224.

87. S. Arora, Selection of thermal management system for modular battery packs of electric vehicles: A review of existing and emerging technologies, *J. Power Sources* 400 (2018) 621-640

88. D.P. Abraham, E.P. Roth, R. Kostecki, K. McCarthy, S. MacLaren, D.H. Doughty, Diagnostic examination of thermally abused high-power lithium-ion cells, *J. Power Sources* 161 (2006) 648-657

89. S. Al Hallaj, H. Maleki, J.S. Hong, J.R. Selman, Thermal modeling and design considerations of lithium-ion batteries, *J. Power Sources* 83 (1999) 1-8.

90. D. Lisbona, T. Snee, A review of hazards associated with primary lithium and lithium-ion batteries, *Process Saf. Environ. Protect.* 89 (2011) 434-442.

91. H. Yang, S. Amiruddin, H.J. Bang, Y.-K. Sun, J. Prakash, A review of Li-ion cell chemistries and their potential use in hybrid electric vehicles, *J. Ind. Eng. Chem.* 12 (2006) 12-38.

92. Y. Lai, S. Du, L. Ai, L. Ai, Y. Cheng, Y. Tang, M. Jia, Insight into heat generation of lithium ion batteries based on the electrochemical-thermal model at high discharge rates, *Int. J. Hydrogen Energy* 40 (2015) 13039-13049.

93. G. Xia, L. Cao, G. Bi, A review on battery thermal management in electric vehicle application, *J. Power Sources* 367 (2017) 90-105.

94. A. R. M. Siddique, S. Mahmud, B. V. Heyst. A comprehensive review on a passive (phase change materials) and an active (thermoelectric cooler) battery thermal management system and their Limitations, *J. Power Sources* 401 (2018) 224-237.

95. I. Dinçer, H.S. Hamut, N. Javani, Thermal management of electric vehicle battery systems, John Wiley & Sons Ltd, 2017

96. J. Jaguement, N. Omar, P.V. Bossche, J. Mierlo, Phase-change materials (PCM) for automotive applications: A review, *Appl. Therm. Eng.* 132 (2018) 308-320.

97. R. Zhao, S. Zhang, J. Liu, J. Gu, A review of thermal performance improving methods of lithium ion battery: electrode modification and thermal management system, *J. Power Sources* 299 (2015) 557-577.

98. M. Malik, I. Dincer, M.A. Rosen, Review on use of phase change materials in battery thermal management for electric and hybrid electric vehicles, *Int. J. Energy Res.* (2016) 1011-1031.

99. L.F. Cabeza, A. Castell, C. Barreneche, A. De Gracia, A.I. Fernández, Materials used as PCM in thermal energy storage in buildings: a review, *Renew. Sustain. Energy Rev.* 15 (2011) 1675-1695.

100. J. Jaguemont, L. Boulon, Y. Dubé, A comprehensive review of lithium-ion batteries used in hybrid and electric vehicles at cold temperatures, *Appl. Energy* 164 (2016) 99-114.

101. Q. Wang, B. Jiang, B. Li, Y. Yan, A critical review of thermal management models and solutions of lithium-ion batteries for the development of pure electric vehicles, *Renew. Sustain. Energy Rev.* 64 (2016) 106-128.

102. N.R. Jankowski, F.P. McCluskey, A review of phase change materials for vehicle component thermal buffering, *Appl. Energy* 113 (2014) 1525-1561.

103. I. Dincer, H.S. Hamut, J. Nader, Thermal management of electric vehicle battery systems, Wiley Edition, 2017.

104. M. Gepp, R. Filimon, S. Koffel, V.R.H. Lorentz, M. März, Advanced thermal management for temperature homogenization in high-power lithium-ion battery systems based on prismatic cells, *IEEE Int. Symp. Ind. Electron.* (2015) 1306-1311.

105. D. Chen, J. Jiang, G.H. Kim, C. Yang, A. Pesaran, Comparison of different cooling methods for lithium ion battery cells, *Appl. Therm. Eng.* 94 (2016) 846-854.

106. M.M. Farid, A.K. Khudhair, S.A.K. Razackm, A.H. Said, A review on phase change energy storage: materials and applications, *Energy Convers. Manag.* 45 (2004) 1579-1615.

107. L. Fan, J.M. Khodadadi, Thermal conductivity enhancement of phase change materials for thermal energy storage: A review, *Renew. Sustain. Energy Rev.* 15 (2011) 24-46.

108. P. Singh, R.K. Sharma, A.K. Ans, R. Goyal, A. Sari, V.V. Tyagi, A comprehensive review on development of eutectic organic phase change materials and their composites for low and medium range thermal energy storage applications, *Sol. Energy Mater. Sol Cells* 223 (2021) 110955 (25pp).

109. H. Ke, Phase diagrams, eutectic mass ratios and thermal energy storage properties of multiple fatty acid eutectics as novel solid-liquid phase change materials for storage and retrieval of thermal energy, *Appl. Therm. Eng.* 113 (2017) 1319-1331.

110. S. Kahwaji, M.A. White, Prediction of the properties of eutectic fatty acid phase change materials, *Thermochim. Acta* 660 (2018) 94-100.

111. G. Yang, Y. Yim, J. Lee, Y. J. Heo, S. J. Park, Carbon-filled organic phase-change materials for thermal energy storage: a review, *Molecules* 24 (2019) 2055 (17pp).

112. Y. Lin, Y. Jia, G. Alva, G. Fang, Review on thermal conductivity enhancement, thermal properties and applications of phase change materials in thermal energy storage, *Renew. Sustain. Energy Rev.* 82 (2018) 2730-2742.

113. L. Fan, J.M. Khodadadi, Thermal conductivity enhancement of phase change materials for thermal energy storage: A review, *Renew. Sustain. Energy Rev.* 15 (2011) 24-46.

114. Q. Tang, J. Sun, S. Yu, G. Wang, Improving thermal conductivity and decreasing supercooling of paraffin phase change materials by n-octadecylamine-functionalized multi-walled carbon nanotubes, *RSC Adv.* 4 (2014) 36584-38590.

115. Z.T. Yu, X. Fang, L.W. Fan, X. Wang, Y.Q. Xiao, Y. Zeng, X. Xu, Y.C. Hu, K.F. Cen, Increased thermal conductivity of liquid paraffin-based suspensions in the presence of carbon nano-additives of various sizes and shapes, *Carbon* 53 (2013) 277-285.

116. P. Cheng, X. Chen, H. Gao, X. Zhang, Z. Tang, A. Li, G. Wang, Different dimensional nanoadditives for thermal conductivity enhancement of phase change materials: fundamentals and applications, *Nano Energy* 85 (2021) 105948 (25pp).

117. X. Chen, H. Gao, Z. Tang, W. Dong, A. Li, G. Wang, Optimization strategies of composite phase change materials for thermal energy storage, transfer, conversion and utilization, *Energy Environ. Sci.* 13 (2020) 4498-4535.

118. H. Gao, J. Wang, X. Chen, G. Wang, X. Huang, A. Li, W. Dong, Nanoconfinement effects on thermal properties of nanoporous shape-stabilized composite PCMs: a review, *Nano Energy* 53 (2018) 769-797.

119. A. Giri, P.E. Hopkins, A review of experimental and computational advances in thermal boundary conductance and nanoscale thermal transport across solid interfaces, *Adv. Funct. Mater.* 30 (2019) 1903857.

120. W. Jang, Z. Chen, W. Bao, C.N. Lau, C. Dames, Thickness-dependent thermal conductivity of encased graphene and ultrathin graphite, *Nano Lett.* 10 (2010) 3909-3913.

121. L.A. Jauregui, Y. Yue, A.N. Sidorov, J. Hu, Q. Yu, G. Lopez, R. Jalilian, D.K. Benjamin, D.A. Delk, W. Wu, Z. Liu, X. Wang, Z. Jiang, X. Ruan, J. Bao, S.S. Pei, Y.P. Chen, Thermal transport in graphene nanostructures: experiments and simulations, *ECS Transactions* 28 (2010) 73-83.

122. L. Chen, H. Xie, B. Wang, Z. Wu, Thermal transport behaviors of suspended graphene sheets with different sizes, *Int. J Therm. Sci.* 94 (2015) 221-227.

123. P.G. Klemens, Theory of the a-plane thermal conductivity of graphite, *J. Wide Bandgap Mater.* 7 (2000) 332-339.

124. D.L. Nika, S. Ghosh, E.P. Pokatilov, A.A. Balandin, Lattice thermal conductivity of graphene flakes: comparison with bulk graphite, *Appl. Phys. Lett.* 94 (2009) 203103.

125. D.L. Nika, A.S. Askerov, A.A. Balandin, Anomalous size dependence of the thermal conductivity of graphene ribbons, *Nano Lett.* 12 (2012) 3238-3244.

126. C. Yu, G. Zhang, Impacts of length and geometry deformation on thermal conductivity of graphene nanoribbons, *J. Appl. Phys.* 113 (2013) 044306.

127. H. Malekpour, K.H. Chang, J.C. Chen, C.Y. Lu, D.L. Nika, K.S. Novoselov, A.A. Balandin, Thermal conductivity of graphene laminate, *Nano Lett.* 14 (2014) 5155-5161.

128. T.H. Liu, S.C. Lee, C.W. Pao, C.C. Chang, Anomalous thermal transport along the grain boundaries of bicrystalline graphene nanoribbons from atomistic simulations, *Carbon* 73 (2014) 432-442.

129. Y. Cui, C. Liu, S. Hu, X. Yu, The experimental exploration of carbon nanofiber and carbon nanotube additives on thermal behavior of phase change materials, *Sol. Energy Mater. Sol. Cells* 95 (4) (2011) 1208-1212.

130. W. Wang, X. Yang, Y. Fang, J. Ding, J. Yan, Enhanced thermal conductivity and thermal performance of form-stable composite phase change materials by using  $\beta$ -Aluminum nitride, *Appl. Energy* 86 (7) (2009) 1196-1200.

131. J. Wang, H. Xie, Z. Xin, Y. Li, L. Chen, Enhancing thermal conductivity of palmitic acid based phase change materials with carbon nanotubes as fillers, *Sol. Energy* 84 (2) (2010) 339-344.

132. S. Harish, D. Orejon, Y. Takata, M. Kohno, Thermal conductivity enhancement of lauric acid phase change nanocomposite with graphene nanoplatelets, *Appl. Therm. Eng.* 80 (2015) 205-211.

133. M. Li, A nano-graphite/paraffin phase change material with high thermal conductivity, *Appl. Energy* 106 (2013) 25-30.

134. Y. Seki, S. Ince, M.A. Ezan, A. Turgut, A. Erek, Graphite nanoplates loading into eutectic mixture of Adipic acid and Sebatic acid as phase change material, *Sol. Energy Mater. Sol. Cells* 140 (2015) 457-463.

135. M. Amin, N. Putra, E.A. Kosasih, E. Prawiro, R.A. Luanto, T.M.I. Mahlia, Thermal properties of beeswax/graphene phase change material as energy storage for building applications, *Appl. Therm. Eng.* 112 (2017) 273-280.

136. Q. Zhang, Z. Luo, Q. Guo, G. Wu, Preparation and thermal properties of short carbon fibers/erythritol phase change materials, *Energy Convers. Manage.* 136 (2017) 220-228.

137. T. Oya, T. Nomura, M. Tsubota, N. Okinaka, T. T. Akiyama, Thermal conductivity enhancement of erythritol as PCM by using graphite and nickel particles, *Appl. Therm. Eng.* 61 (2) (2013) 825-828.

138. N. Sahan, M. Fois, H. Paksoy, Improving thermal conductivity phase change materials-a study of paraffin nanomagnetite composites, *Sol. Energy Mater. Sol. Cells* 137 (2015) 61-67.

139. S. Motahar, N. Nikkam, A. A. Alemrajabi, R. Khodabandeh, M.S. Toprak, M.Muhammed, A novel phase change material containing mesoporous silica nanoparticles for thermal storage: a study on thermal conductivity and viscosity, *Int. Commun. Heat Mass Transfer* 56 (2014) 114-120.

140. B. Tang, C. Wu, M. Qiu, X. Zhang, S. Zhang, PEG/SiO<sub>2</sub>-Al<sub>2</sub>O<sub>3</sub> hybrid form-stable phase change materials with enhanced thermal conductivity, *Mater. Chem. Phys.* 144 (1) (2014) 162-167.

141. J.L. Zeng, Z. Cao, W. Yang, L.X. Sun, L. Zhang, Thermal conductivity enhancement of Ag nanowires on an organic phase change material, *J. Therm. Anal. Calorim.* 101 (1) (2010) 385-389.

142. G. Ma, J. Sun, Y. Zhang, Y. Jing, Y. Jia, Preparation and thermal properties of stearic acid-benzamide eutectic mixture/expanded graphite composites as phase change materials for thermal energy storage, *Powder Technol.* 342 (2019) 131-140.

143. F. Tang, D. Su, Y. Tang, G. Fang, Synthesis and thermal properties of fatty acid eutectics and diatomite composites as shape-stabilized phase change materials with enhanced thermal conductivity, *Sol. Energy Mater. Sol. Cells* 141 (2015) 218-224.

144. D. G. Atinifu, W. Dong, X. Huang, H. Gao, G. Wang, Introduction of organic-organic eutectic PCM in mesoporous N-doped carbons for enhanced thermal conductivity and energy storage capacity, *Appl. Energy* 211 (2018) 1203-1215.

145. M. Martín, A. Villalba, A.I. Fernández, C. Barreneche, Development of new nano-enhanced phase change materials (NEPCM) to improve energy efficiency in buildings: lab-scale characterization, *Energy Build.* 192 (2019) 75-83.

146. S. Kahwaji, M.A. White, Data supporting the prediction of the properties of eutectic organic phase change materials, *Data in Brief* 17 (2018) 724-730.

## CHAPTER-3

---

### Instrumentation & Characterization and Methodology

---

#### 3.1 Instrumentation & Characterization

Various kinds of characterization tools were utilized for the characterization of materials in this research work are as follows:

Scanning electron microscopy (SEM, Carl-Zeiss, Gemini-500 model, Germany), transmission electron microscopy (TEM, TEM, Model FEI Technai G<sup>2</sup> S-Twin, USA), Raman spectroscopy (Lab Ram HR800 Raman spectrometer; 514.5 nm green line of Ar<sup>+</sup> ion laser was used as the excitation source), BET surface area analyzer (BET, Micromeritics, ASAP 2020 model, USA), X-ray diffraction analysis (XRD, XRD, Bruker's AXS Model D8 Advance System) simultaneous thermal analysis (STA, STA, 449 Jupiter model, Netzsch, Germany), X-ray photoelectron spectroscopy (XPS, Omicron model, USA), and various kinds of electrochemical studies (BioLogic Make, BCS-805 Model, France). A laser flash analyzer (LFA, Netzsch, LFA 427, Germany) was used to measure PCM materials' thermal diffusivity and thermal conductivity.

The purpose of each characterization techniques, along with their principle and mechanism involved in the in-depth analysis of powder was delineated as below:

SEM is a morphology analysis technique that provides a highly magnified image of the specimen's surface (1-3). It provides topographical and morphological information of the sample. A pinch of powder was uniformly and evenly spread over a conductive carbon or copper tape placed on an aluminium/copper stub. The powder material with poor electrical conductivity was coated with a fine layer of gold through a vacuum-assisted sputtering system to improve the electrical conductivity.

TEM technique is used to obtain the microstructure under high resolution. It is advantageous in obtaining both the microstructure and diffraction information from a single specimen (4-6). It is a handy technique for getting the crystal structure (as that of XRD) and the materials' microstructure. The sample preparation is a critical trick in observing the specimen in detail. Its practice involves the suspension of a pinch of powder in 5 ml of ethanol solution, sonicating the sample for half an hour, and drop-casted carefully on a carbon-coated copper grid. The material shall be evenly distributed over a grid; otherwise, it may create a lump and could not be transparent. The stub along with the sample was dried to evaporate solvent before its loading into the vacuum chamber.

Raman spectroscopy becomes a crucial characterization tool when dealing with carbon-related materials (7-10). This technique is instrumental in detecting the vibrational frequencies of the molecules of the specimen under consideration. When a beam of laser (source of irradiation) is transmitted through the sample, a fraction of the scattered light is detected at a particular angle which is usually a small fraction of the source (approximately < 0.1 %) by the visible-region spectrophotometer and is drawn into a series of lines called Raman lines. Raman spectroscopy is governed by Raman scattering, which discusses the molecular excitation to the virtual states and Rayleigh scattering discussions. Generally, in a Raman spectrum, the X-axis contains a wavenumber, which detects the vibrational modes or gives information about the functional groups/identities. In contrast, the Y-axis intensity shows the concentration of the active species present in the specimen. It exhibits strong frequency dependence on the excitation energy of the Laser

XRD is used to obtain the crystalline information and the specimen's average crystallite size (11-12). The sample prepared for XRD analysis is in its powdery form, spread uniformly on a glass substrate. When a beam of monochromatic radiation ( $\text{Cu-K}_\alpha$  – 0.154 nm) is focused over the specimen, the high energetic rays bombard with the specimen molecules producing characteristic X-rays of the sample. The XRD spectra contain diffraction ( $2\theta$ ) on the X-axis while it has intensity on the Y-axis. The X-axis data helps identify the specimen qualitatively (elemental analysis). Simultaneously, the intensity corresponds to the degree of crystallinity, i.e. the more the peak intensity, the more that particular crystalline nature existing in the specimen.

BET is used to measure surface area and pore-size distribution (13). It measures the physical adsorption of nitrogen gas molecules on a solid surface and serves as the basis for a critical analysis technique to measure the material's specific surface area. Before the sample's specific surface area can be determined, it is necessary to remove gasses and vapours that may have physically adsorbed onto the surface after manufacture and during treatment, handling, and storage. If out-gassing is not achieved, the specific surface area may be reduced or maybe variable because an intermediate zone of the surface is covered with molecules of the previously adsorbed gasses or vapours. The out-gassing conditions are critical for obtaining the required precision and accuracy of specific surface area. The BET determination is usually carried out at the temperature of liquid nitrogen. The amount of gas adsorbed can be measured by a volumetric or continuous flow procedure.

STA is a combination of thermogravimetry (TG), differential thermogravimetry (DTG) and differential scanning calorimetry (DSC) (14-16). TG is performed on the material to

determine changes in weight with the temperature change. Such analysis relies on a high degree of precision in three measurements; weight, temperature and temperature change. Basically, TG consists of two crucibles; one is the reference and another for the sample. The powder-filled in a crucible is allowed to elevated temperatures at a fixed heating rate to determine weight loss. TG is commonly employed in research and testing to determine characteristics of materials such as polymers, to determine degradation temperatures, absorbing materials, decomposition points of explosives and solvent residues. It is also used to estimate the corrosion kinetics in high-temperature oxidation. A derivative weight loss curve (DTG) can be used to convey the point at which weight loss is most apparent. In a DSC technique, the heat flow into or out of a sample is measured as a temperature function. DSC was deployed to study the latent heat fusion of pure PCM materials and nano-filled PCM composites.

XPS is a quantitative spectroscopic technique with the surface chemical analysis that processes the elemental functionality, functional moieties, and electronic state of the elements within a powder material (17-21). Simultaneously measuring the kinetic energy and the number of electrons that escape from the surface ( 1-10 nm) of the material (photoelectric effect) is analyzed to generate XPS spectra by irradiating the powder with a beam of intense X-rays. It works under ultra-high vacuum conditions.

Electrochemical energy storage studies are performed for the as-prepared electrode using three primary techniques: Cyclic voltammetry (CV), galvanostatic Charge-discharge (GCD), and Electrochemical impedance spectroscopy (EIS) (22-27). CV is used for measuring the I-V response of the electrode by applying a voltage ramp of certain volts depending upon the type of the electrolyte. CV curves include oxidation-reduction peaks. The oxidation peak(s) is observed during the positive voltage duration. In contrast, the discharge peak(s) is observed during the reverse cycle (Note: The oxidation-reduction peaks are observed only if there is the pseudo-capacitive type of material). For an EDC, the peaks are not observed. GCD is used to measure the V-t (Voltage-time) response, which is used to determine the charge-discharge phenomenon. It is the primary technique for determining the specific capacitance of the electrode besides CV. The GCD curves describe the discharge time data, which is used for the calculation of specific capacitance. EIS is used for evaluating the frequency response of the electrode. The frequency response is an impedance curve plotted between Real Z (X-axis) and Img Z (Y-axis). In general, the frequency response is plotted between 0.01 and 100,000 Hz, with the amplitude of voltage being 5 mV-10 mV (AC voltage). The high-frequency response corresponds to the electrode's pure capacitive nature, while the lower frequencies correspond to the resistive nature of the

electrode. The electrode's frequency response is realized into an equivalent circuit consisting of a combination of resistors and capacitors the referred to as the Nyquist plot.

LFA was deployed to measure the thermal conductivity of materials (28-31). During LFA measurements, a very thin film of conducting carbon (in the form of graphite milk) was sprayed on top of the material to ensure continuity and ensure absorption by avoiding the laser's scattering (28). A laser flash system with Nd: YAG pulse laser was used to measure the material's thermal diffusivity with laser energy of 20 joules/ pulse and a laser transmission filter of 25%. The infrared detector measured the temperature at the bottom of the material subjected to a short burst of radiant energy from the laser source and the temperature difference. The equation to obtain the thermal diffusivity ( $\alpha$ ) is  $\alpha = 0.138785 l^2/t^{0.5}$ , where  $l$  is the thickness of the material, and  $t$  is the time to reach 50 % of the maximum temperature. Thermal conductivity ( $k$ ) was calculated using the relation  $k = \alpha \cdot \rho \cdot C_p$ , where  $\alpha$ ,  $\rho$  and  $C_p$  are thermal diffusivities, density and specific heat of the material. An argon flow of 100 ml/min maintained throughout the measurements during the heating and cooling.

### 3.2 Methodology

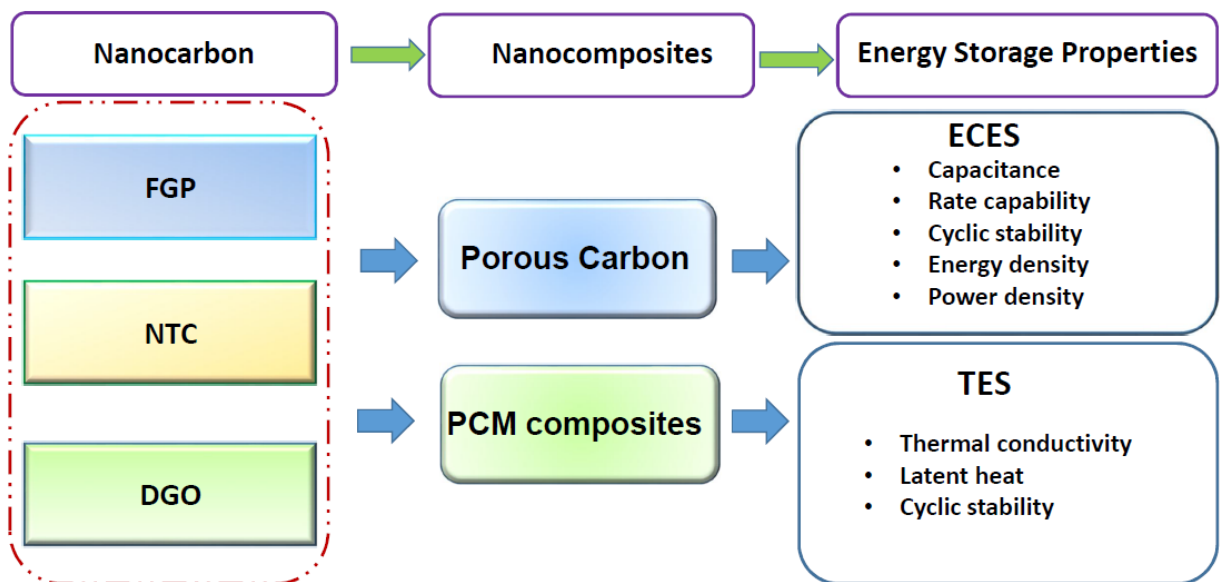


**Fig.3.1** A schematic depicting the methodology adopted for research work.

In a process of developing advanced materials for energy storage in ECES and TES, nanocarbon-based functional nanocomposites are developed. Typically, it consists of three stages; (i) synthesis of various (three) nanocarbon, (ii) development of nanocomposites, and (iii) evaluation of energy storage properties as depicted in **Fig.3.1**.

### 3.3 References

1. C.W.Oatley, W.C. Nixon, R.F.W. Pease, Scanning electron microscopy, *Adv. Electronics Electron. Phys.* 21 (1965) 181-247.
2. E. Suzuki, High-resolution scanning electron microscopy of immunogold-labelled cells by the use of thin plasma coating of osmium, *Journal of Microscopy*. 208 (3) (2002) 153-157.
3. A. Antonovsky, The application of colour to SEM imaging for increased definition, *Micron and Microscopica Acta*. 15 (2) (1984) 77-84.
4. S.J.Pennycook, M. Varela, C.J.D. Hetherington, A.I. Kirkland, Materials advances through aberration-corrected electron microscopy, *MRS Bulletin* 31 (2011) 36-43.
5. P.A. Crozier, T.W. Hansen, In situ and operando transmission electron microscopy of catalytic materials, *MRS Bulletin* 40 (2014) 38-45.
6. A.P. Pogany, P.S. Turner, Reciprocity in electron diffraction and microscopy, *Acta Crystallography. Sect. A* 24 (1) (1968) 103-109.
7. M. S. Dresselhaus, A. Jorio, M. Hofmann, G. Dresselhaus, R.Saito, Perspectives on carbon nanotubes and graphene Raman spectroscopy, *Nano Lett.* 10 (2010) 751-758.
8. J.B. Wu, M. L. Lin, X. Cong, H.N. Liu, P. H. Tan, Raman spectroscopy of graphene-based materials and its applications in related devices, *Chem. Soc. Rev.* 47 (2018) 1822-1873.
9. F. Tuinstra, J.L. Koenig, Raman spectrum of graphite, *J. Chem. Phys.* 53 (1970) 1126-1130.
10. A.C. Ferrari, Raman spectroscopy of graphene and graphite: disorder, electron-phonon coupling, doping and nonadiabatic effects, *Solid State Commun.* 143 (2007) 47-57.
11. W.H. Bragg, W.L. Bragg, The reflection of X-rays by crystals, *Proc. R. Soc. Lond. A* 88 (605) (1913) 428-438.
12. E.S. Ameh, A review of basic crystallography and X-ray diffraction applications, *Int. J. Adv. Manuf.* 105 (2019) 3289-3302.
13. P. Sinha, A. Datar, C. Jeong, X. Deng, Y.G. Chung, L.C. Lin, Surface area determination of porous materials using the Brunauer-Emmett-Teller (BET) method: limitations and improvements, *J.Phys. Chem. C* 123 (2019) 20195-20209.
14. M. J. Biercuk, M. C. Llaguno, M. Radosavljevic, J. K. Hyun, A. T. Johnson, J. E. Fischer, Carbon nanotube composites for thermal management, *Appl. Phys. Lett.* 80 (2002) 2767-2769.

15. D. Walter, G. Buxbaum, W. Laqua, The mechanism of the thermal transformation from goethite to hematite, *J.Therm. Anal. Cal.* 63 (2001)733-748.
16. W. Zhang, M. Li, DSC Study on the polyacrylonitrile precursors for carbon fibers, *J. Mater. Sci. Technol.* 21 (4) (2005) 581-584.
17. K. Ghosh, M. Kumar, T Maruyama, Y. Ando, Tailoring the field emission property of nitrogen-doped carbon nanotubes by controlling the graphitic/pyridinic substitution, *Carbon* 48 (1) (2010) 191-200.
18. K. Chizari, U. Sundararaj, The effects of catalyst on the morphology and physicochemical properties of nitrogen-doped carbon nanotubes, *Mater. Lett.* 116 (2014) 289-292.
19. W. Kang, H. Li, M. Ai, S. Wei, H. Gao, J. Liu, Y. Qian, Synthesis of nitrogen-doped carbon and application in highly selective and sensitive dopamine sensing, *Mater. Lett.* 116 (2014) 374-377.
20. K. Chizari, A.Vena, L. Laurentius, U. Sundararaj, The effect of temperature on the morphology and chemical surface properties of nitrogen-doped carbon nanotubes, *Carbon* 68 (2014) 369-379.
21. P.K. Chu, L. Li, Characterization of amorphous and nanocrystalline carbon films, *Mater. Chem. Phys.* 96 (2006) 253-277.
22. B.E. Conway, *Electrochemical supercapacitors: scientific fundamentals and technological applications*, Kluwer Academic/Plenum Publishers, New York, 1999.
23. J. R. Miller, R.A. Outlaw, B.C. Holloway, Graphene electric double layer capacitor with ultra-high-power performance, *Electrochim. Acta* 56 (2011) 10443-10449.
24. L.L. Zhang, X.S. Zhao, Carbon-based materials as supercapacitor electrodes, *Chem. Soc. Rev.* 38 (2009) 2520-2531.
25. T. Morishita, Y. Soneda, T. Tsumura, M. Inagaki, Preparation of porous carbons from thermoplastic precursors and their performance for electric double layer capacitors, *Carbon* 44 (2006) 2360-2367.
26. M. Jiang, X.P. Cao, D.D. Zhu, Y.X. Duan, J.M. Zhang, Hierarchically porous N-doped carbon derived from ZIF-8 nanocomposites for electrochemical applications, *Electrochim. Acta* 196 (2016) 699-707.

27. W.C. Chen, T.C. Wen, H. Teng, Polyaniline-deposited porous carbon electrode for supercapacitor, *Electrochimica Acta* 48 (2003) 641-649.
28. L. Qiu, P. Guo, Q. Kong, C. W. Tan, K. Liang, J. Wei, J. N. Tey, Y. Feng, X. Zhang, B. K. Tay, Coating-boosted interfacial thermal transport for carbon nanotubearray nano-thermal interface materials, *Carbon* 145 (2019) 725-733.
29. A.N. Volkov, L.V. Zhigilei, Heat conduction in carbon nanotube materials: Strong effect of intrinsic thermal conductivity of carbon nanotubes, *Appl. Phys. Lett.* 101 (2012) 043113 (1-5)
30. W.Yu,L.Wang, Y.Qi, L.Chen, L.Wang, H.Xie, The influence of nitrogen doping on thermal conductivity of carbon nanotubes, *Thermochim. Acta* 617 (2015) 163-168
31. S.K. Chien, Y.T. Yang, C.K.Chen, The effects of vacancy defects and nitrogen doping on the thermal conductivity of armchair (10, 10) single-wall carbon nanotubes, *Solid state commun.* 151 (2011) 1004-1008.

## CHAPTER-4

---

### **Nanocarbon/N-doped carbon hybrid for symmetric supercapacitor**

---

The technical content described in chapter-4 is based on the work published in *Colloids and Surfaces A: Physicochemical and Engineering Aspects* 627 (2021) 127225.

#### **4.1. Introduction**

Alarming environmental concerns and global warming raised the question of exploring green technologies, which could avoid fossil fuels (FF). Rapid depletion and hazardous air pollution related to FF laid a route to investigate alternate energy technology to mitigate FF dependency (1, 2). As a lookout for renewable and green energy sources, solar, electrochemical energy storage/conversion, wind, geothermal etc., are widely explored (3-8). However, their intermittent nature posed a critical challenge on their on-time availability. To narrow the gap between the supply and demand of energy, energy storage devices such as batteries and supercapacitors or their hybrids play vital roles. Consequently, exceptionally promising high-performance electrode materials for capacitive energy storage (CES) in supercapacitors are insightful focus to find suitability in a broad range of applications in various fields of modern technology (9-11). High-performance electrode materials with exceptional properties gained huge interest to apply them for multifunctional and compact energy storage devices.

As an electrode material for supercapacitor, the material with high surface area, high electrical conductivity, and suitable pore-size distribution are desired to develop high-performance devices (12-16). In exploring various powder materials, activated carbon is well-known for its usages for several years. However, its limited capacitance made the scientific community look for alternative (12-14, 17). In the process of exploiting other materials, the nanoscaled-carbon-coupled carbonaceous material hybrid exhibited exceptionally remarkable electrochemical properties due to the combination of nanocarbon-related physicochemical properties along with other carbonaceous material (18-20). In a nanoscaled-carbon category, graphene, carbon nanotubes, de-oxygenated graphene oxide and onion-like carbon are of great interest in increasing the electrical conductivity of hybrids to enhance the charge transfer during the charge storage. The heteroatom-incorporated (N, O, B, P, S, and F) carbon network play a detrimental effect on swift charge transfer in energy conversion/storage (21-26). The functionalities induced due to the addition of heteroatoms in the carbon network participate in pseudocapacitive characteristics to enhance capacitance. To impart rapid ion-transport in carbon

network, the strategies such as the addition of nanocarbon, N-doping and nanotexturing are adopted. It is believed that the addition of nanocarbon, N-doping and nanotexturing could assist in increasing the electrical transport, redox reactions and increase in surface area, respectively.

Herein, this work demonstrates a comparative analysis (four porous carbon material) of capacitive energy storage dependent on kind of nanocarbon with multidimensionality and diverse structural degree. The primary focus was laid on the preparation of porous hybrid consisting of nitrogen-enriched carbon (NC) coated on few-layered graphene platelets (FGP), nitrogen-incorporated tubular carbon (NTC) and deoxygenated graphene oxide (DGO) applied for supercapacitor. FGP-loaded NC exhibited superior capacitive performance, even better than commercially available YP-50.

#### 4.2. Materials and methods

All the chemicals are purchased from M/s Sigma Aldrich, India and used without further purification. FGP was prepared from 2-stage expanded graphite (EG) by implementing complex fluid-dynamics assisted liquid-phase exfoliation to convert it into FGP via rapid exfoliation and fragmentation. The sharp blades in a kitchen-blender could delaminate EG into fewer layers in FGP (27). NTC was grown through atmospheric-pressure chemical vapour deposition by thermocatalytical decomposition of acetonitrile-ethanol over Fe-nano catalyst. In brief, the bubbler-assisted vapour of precursor was allowed over a Fe-nanocatalyst to decompose the hydrocarbon at 800, 850 and 900 °C. The aspects of intensifying process parameters for NTC growth at different growth temperatures are depicted in **Fig.S4.1** and **Fig.S4.2**. Based on yield and N-content, NTC-850 found to be optimum. FGP was oxidized with the oxidizing chemical to prepare graphene oxide (GO). GO was converted into DGO via hydrothermal-assisted partial de-oxygenation technique. GO solution containing reducing agent (ascorbic acid & ammonia solution) thoroughly dispersed with ultrasonication (on/off mode). Then, the solution was sealed in a Teflon-lined autoclave system maintained at 120, 150, 180 and 210 °C for 5 h. The solid was then filtered with a vacuum-assisted filtration, thoroughly washed with water, and acetone. Finally, it was dried at 70 °C for overnight to form DGO. The intensifying process parameters are delineated in **Fig.S4.3** and **Fig. S4.4**. Based on the C/O ratio, DGO-210 found to be optimum.

FGP, NTC and DGO were functionally-modified (with nitric acid) to incorporate the functional groups to tailor the interface with NC. Then, polyaniline was coated on FGP or NTC or DGO via oxidative chemical polymerization of aniline, carbonized and activated with the similar procedure reported elsewhere (28). For simplicity, porous NC-FGP, porous NC-NTC and

porous NC-DGO were designated as PNCG, PNCT and PNCD, respectively. A schematic diagram for the preparation of porous carbon was depicted in **Fig.4.1**. Later, PNCG, PNCT and PNCD powder was collected for further characterization and electrochemical performance.

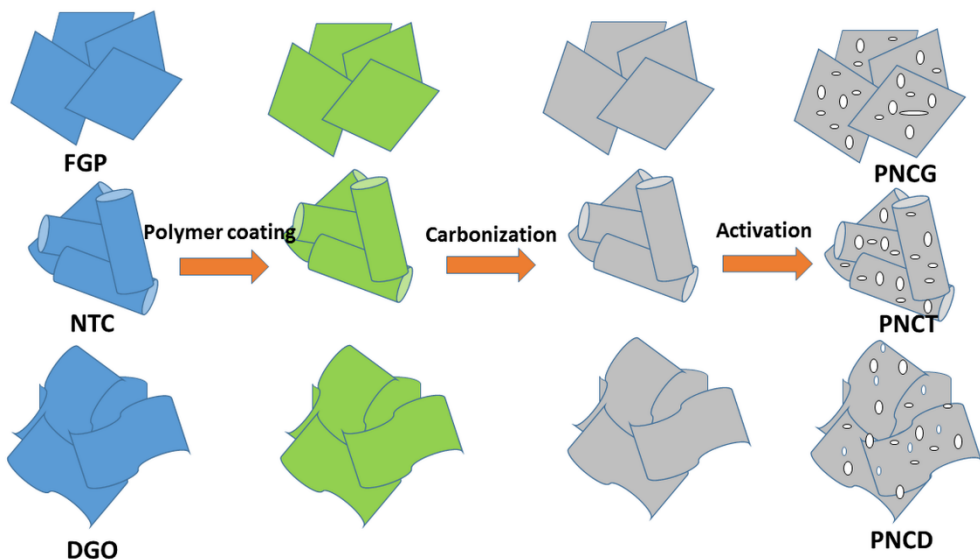


**Fig.4.1** Schematic diagram depicting the procedure for preparation of PNCG, PNCT and PNCD.

FGP, NTC, DGO, PNCG, PNCT and PNCD were characterized using scanning electron microscopy (SEM, Carl-Zeiss, Gemini-500 model, Germany ), X-ray photoelectron spectroscopy (XPS, Omicron model, USA), simultaneous thermo-gravimetric analysis (STA, 449 Jupiter model, Netzsch, Germany), and Raman spectroscopy (Lab Ram HR800 Raman spectrometer , 514.5 nm) to determine the morphological aspects , elemental composition, thermal stability, BET surface area, and crystallinity of the products, respectively.

All electrochemical measurements were performed in a sandwich-structured coin-cell configuration. The electrochemical cell containing 3 M KOH was used as the electrolyte. The mixture of electroactive material (80 %), acetylene black (10 %) and polyvinylidene fluoride (10 %) in an organic solvent was uniformly casted onto a custom-designed flexible graphite foil (10 mm × 10 mm) by doctor blade process, and then, dried for 20 h to evaporate the solvent.

The mass loading of active material in each electrode is maintained with 2.96 mg/cm<sup>2</sup>. The electrochemical workstation (Biologic Make, BCS-805 Model, France) was used to perform cyclic voltammetry (CV), galvanostatic charge/discharge tests (GCD), and electrochemical impedance spectroscopy (EIS) for the measurement of electrochemical properties. The EIS analyses were measured at an open circuit potential of 5 mV sinusoidal voltage in the frequency range of 0.01 Hz-10 kHz.

### 4.3. Results and discussion

**Fig.4.2** shows the morphology of FGP, NTC, DGO, PNCG, PNCT and PNCD. FGP, NTC and DGO consist of 2D-structure with flat surfaces, 1D-structure with nano pipe morphology, and 2D-structure with wrinkled and folded sheets, respectively, as depicted in **Fig.4.2 (a, b, and c)**. Upon activation process, NC on FGP, NTC and DGO converted the surfaces into highly rough and uneven due to the formation of nano porosity-rich surfaces along with oxidized surfaces. All three materials PNCG, PNCT and PNCD, possess surfaces with shining to a great extent could be due to the presence of oxidized surfaces, which lead to charge accumulation, as shown in **Fig.4.2 (d, e, and f)**.

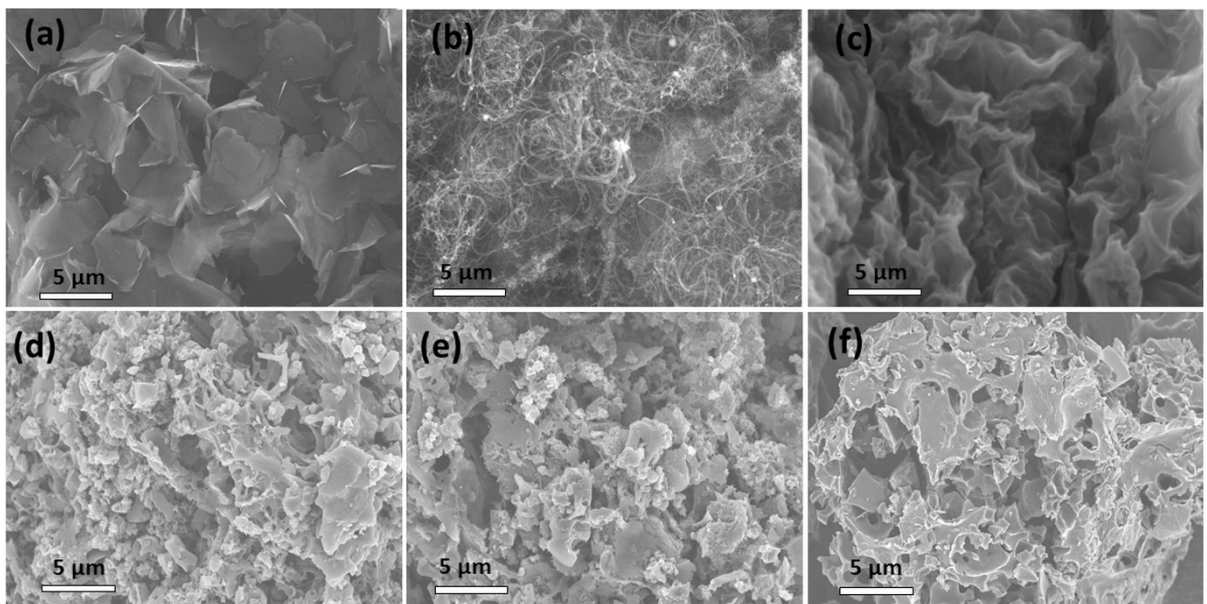


**Fig.4.2** SEM images of (a) FGP, (b) NTC, (c) DGO, (d) PNCG, (e) PNCT, and (f) PNCD.

Raman spectroscopy is a widely compliant qualitative technique that diagnoses the degree of structural defects in carbonaceous materials (29-32). Generally, it consists of first-order and second-order Raman signatures located around 1365, 1599, 2460, and 2744  $\text{cm}^{-1}$  for D-band, G-band, D+D'-band, and 2D-band, respectively. **Fig.4.3** shows the Raman signatures of FGP, NTC, DGO, PNCG, PNCT and PNCD. The Raman signatures (position and intensity) such as D-band and G-band provide insights into defects and graphitization degrees. The qualitative evidence for the degree of defects can be obtained by performing the intensity ratio of the D-band to G-band ( $I_D/I_G$ ). FGP, NTC, DGO, PNCG, PNCT and PNCD possesses  $I_D/I_G$  ratio of 0.220, 0.950, 0.960, 1.016, 1.018 and 1.019, respectively. It indicates that the activation process modifies the surfaces by an etching technique, which resulted in an increase in  $I_D/I_G$  ratio. A higher ratio of  $I_D/I_G$  indicates quite more defects and a lesser degree of graphitization. After activation, the porous carbon (PNCG or PNCT or PNCD) contains huge traces of defect-sites due to disorder, edge

planes, N-incorporated defects  $sp^3$ -hybridized C-species, and activation-induced defects during surface modification.

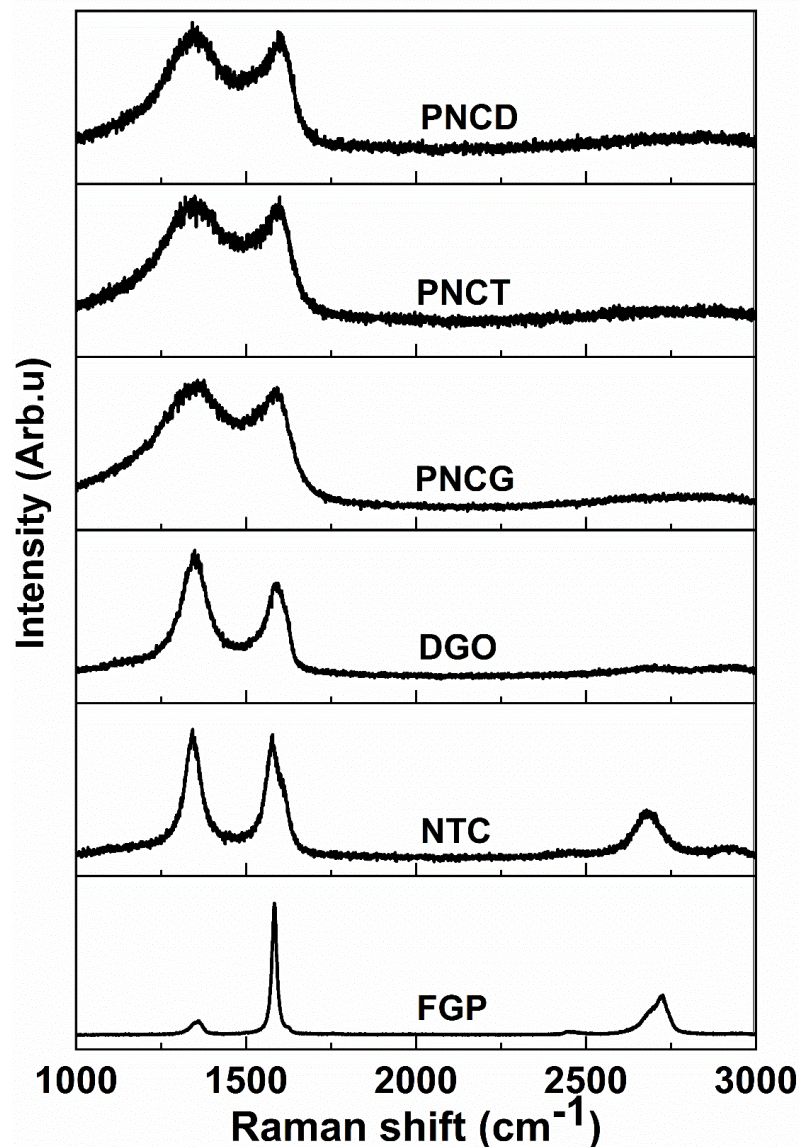


**Fig.4.3** Raman signatures.

XPS measurements (based on binding energy) were performed to find out the functional moieties and elements present in porous carbon (PNCG or PNCT or PNCD), as illustrated in **Fig.4.4**. **Fig.4.4a** shows XPS wide scan for all the three porous materials possesses three intense peaks 284.5, 400.5 and 531.5 eV corresponding to C, N and O, respectively. The material's elemental composition was calculated based on the area under the curve ( $N_A / (C_A + N_A + O_A)$ ) in the XPS-wide scan. PNCG, PNCT, and PNCD exhibited nitrogen content of 4.32, 4.35 and 4.33 at. %, respectively, as illustrated in **Fig. 4.4b**. A piece of detailed information on the presence of C, N, and O-related functional moieties present in PNCG (derived by performing de-

convolution of C1s, N1s and O1s peaks) was described in our previous study elsewhere (28). As the origin of the coated NC material is similar in all the three materials, they possess C, N, and O-related functionality in the undistinguishable and comparable manner described for PNCG without much variation. The elemental composition of PNCG, PNCT, and PNCD was presented in **Table 4.1**. It confirmed that they possess C, N and O quantity without much difference. On considering N-content, they follow in the order of PNCT>PNCD>PNCG. N-related moieties and O-related functional groups are suitable sources of generating pseudo capacitance due to redox reactions (21-26).

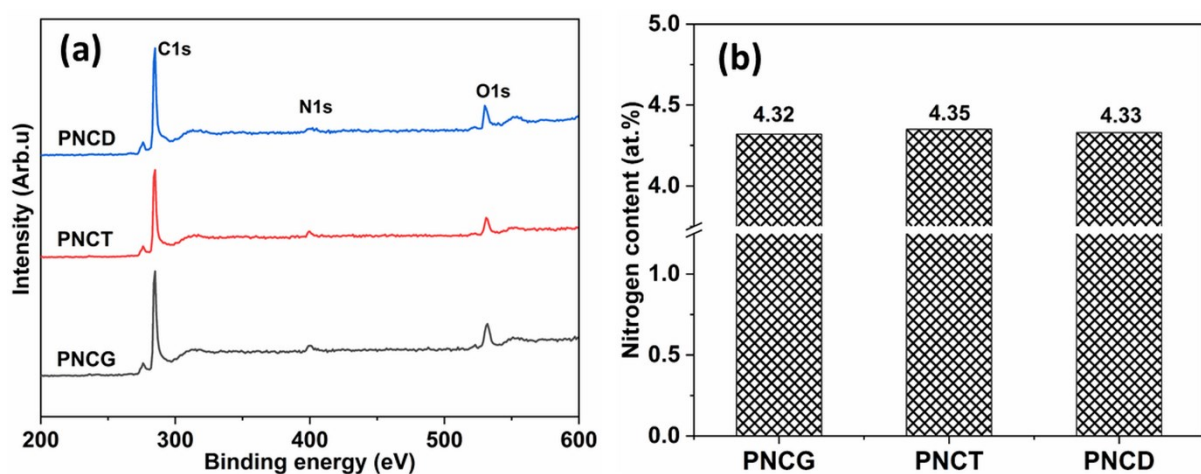


**Fig.4.4** Elemental composition of PNCG, PNCT and PNCD: (a) XPS wide scan, and (b) N-content.

**Table 4.1:** Elemental composition of PNCG, PNCT and PNCD

Material	C (at. %)	N (at. %)	O (at. %)
PNCG	89.42	4.32	6.26
PNCT	89.33	4.35	6.32
PNCD	89.22	4.33	6.45

Electrochemical capacitive behaviour of supercapacitor based on PNCG, PNCT, PNCD and YP-50 (commercial) was evaluated by CV, GCD and EIS techniques as shown in **Fig.4.5**. **Fig. 4.5a** shows that all the four materials showed quasi-rectangular shaped CV indicate double-layer formation and redox-coupled pseudo capacitors via physical adsorption/desorption-mediated charge storage and pseudo capacitance (functional groups). Interestingly, PNCG presented a larger CV curve compared to others implies that it can store more charges than other materials. According to the area under the CV curve, PNCG possesses a large area even compared to commercially available YP-50. Further, the electrochemical properties were diagnosed by GCD, as illustrated in **Fig.4.5b**. All the materials exhibited initial ohmic loss, but PNCG possesses significantly less. GCD showed the nearly-straight lines (presence of N and O functionality) during charging/discharging indicates the capacitive behaviour-dependent in the double-layer capacitor with redox-coupled pseudo capacitors (21-26). PNCG exhibited a larger time during charging/discharging shows its capacitive-rich behaviour in comparison to others. The specific gravimetric capacitance (at different current density) of PNCG, PNCT, PNCD and YP-50 was illustrated in **Fig.4.5c**.

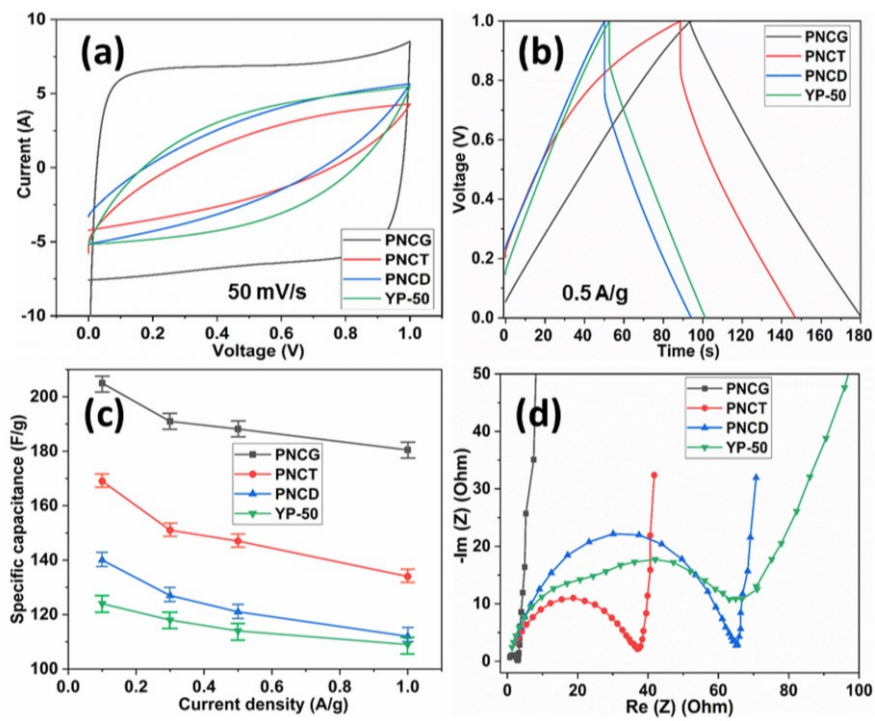


**Fig.4.5** Electrochemical capacitive properties of PNCG, PNCT and PNCD: (a) CV, (b) GCD, (c) rate capability and (d) EIS Nyquist plot.

PNCG, PNCT, PNCD and YP-50 exhibited specific capacitance (at 0.5 A/g) of 188, 147, 121, and 114 F/g, respectively. Considering the rate capability and capacitance, their electrochemical performance found in the order: PNCG>PNCT>PNCD>YP-50. To have a clear idea of their performance, EIS was performed to measure the resistance involved in electrode assembly, and it is depicted in **Fig.4.5d**. The Nyquist plot consists of the semicircle, Warburg impedance and capacitive characteristic line in the high-frequency zone, medium-frequency zone and low-frequency zone, respectively (33-36). The presence of semicircle indicates the contribution of functional groups, defects and redox pseudocapacitive moieties (34). It develops the resistance at the interfaces of the electrode (active material)-electrolyte, which contribute to charge transfer resistance. Warburg impedance was originated from the ion-diffusion within complex and intricate narrow pores (37-39). However, it was not much dominant. The bulk resistance for PNCG, PNCT, PNCD and YP-50 found to be around 0.22, 0.32, 0.35 and 0.35 ohm/cm<sup>2</sup>, respectively. Considering the contribution from bulk resistance and N-doping (functional moieties), the specific capacitance of the porous carbon found in the order of PNCG >PNCT>PNCD>YP-50.

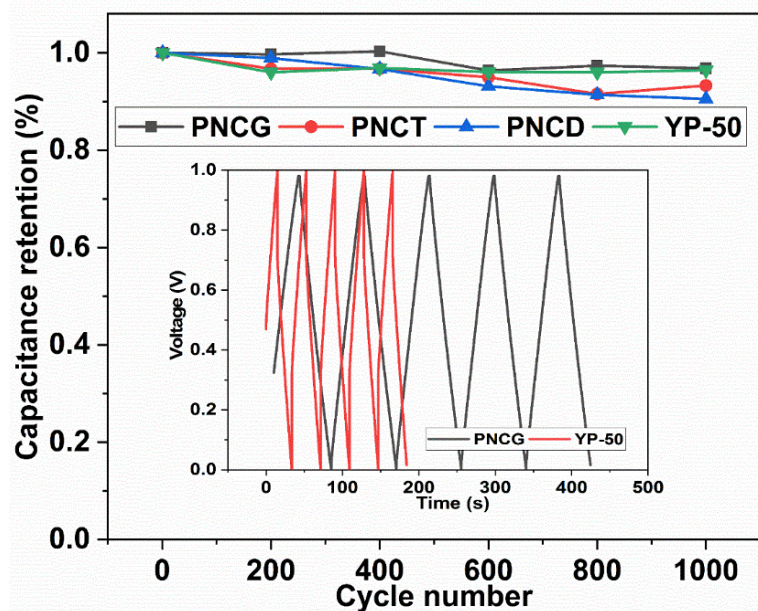


**Fig.4.6** Cyclic stability-based capacitance retention of PNCG, PNCT, PNCD and YP-50.

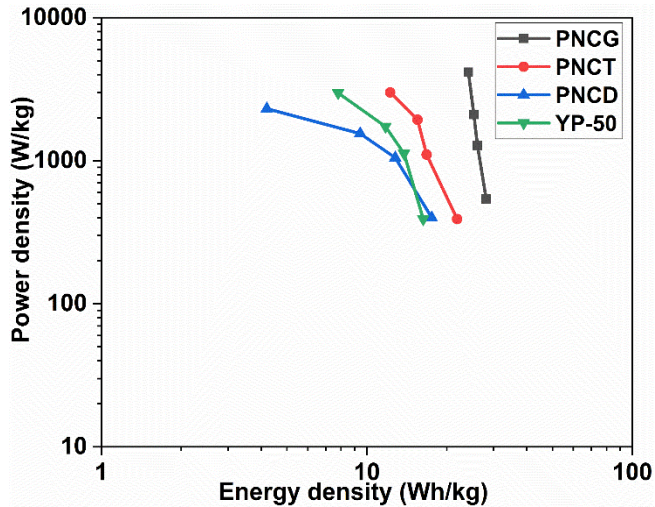


**Fig.4.7** Ragone plot of symmetric supercapacitor cell: PNCG//PNCG, PNCT//PNCT, PNCD//PNCT and YP-50//YP-50

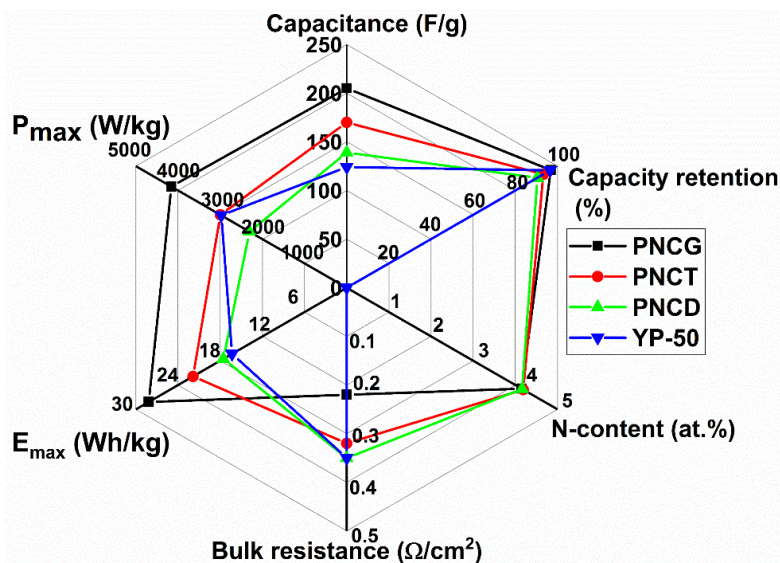
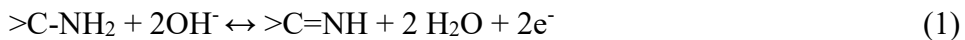


**Fig. 4.8** A radar plot depicting the physicochemical and electrochemical properties of PNCG, PNCT, PNCD and YP-50.

Further, capacity retention of the porous carbon was carried out at 0.5 A/g for 1000 cycles for practical application, and it was shown in **Fig.4.6**. PNCG, PNCT, PNCD and YP-50 exhibited capacity retention of 96.82, 93.26, 90.50 and 96.43 %, respectively. Interestingly, PNCG outperformed other materials in terms of excellent capacity retention. Based on capacity retention, they are organized in the order: PNCG>YP-50>PNCT>PNCD. Overall, the structural degree, N-doping and initial ohmic loss played a crucial role in determining electrochemical capacitive performance. FGP in PNCG could support rapid electron transport owing to high crystallinity

with low defects and a long-range ordered carbon network. Considering the power density and energy density, a Ragone plot was designed as shown in **Fig.4.7**. It infers that PNCG//PNCG exhibited a maximum energy density of 28.17 Wh/kg with the maximum power density of 4160 W/kg.

In addition, the heteroatom-incorporated in carbon network induces pseudocapacitive characteristics, which improves the capacitance. The functional moieties such as N-related and O-related present in porous carbon could participate in electrochemistry to enhance capacitance through the following reactions (40-43):



A radar chart depicting the physicochemical and electrochemical properties of PNCG, PNCT, PNCD and YP-50 is illustrated in **Fig.4.8**.

Especially, PNCG dominates the other three porous carbon in terms of energy density (maximum), power density (maximum), specific capacitance, bulk resistance, and capacity retention. Overall, considering all the physicochemical and electrochemical characteristics, PNCG//PNCG considered best. It exhibited superior maximum energy density and capacity retention on par with the previous reports, as indicated in **Table 4.2** [44-56]. It surpassed even a commercially applied YP-50 in terms of capacitance, energy density and capacity retention.

#### 4.4. Conclusions

To conclude, N-enriched porous carbon loaded with a class of nanocarbon with a variable structural degree was prepared to apply for symmetric carbon/carbon supercapacitor. PNCG//PNCG exhibited a maximum energy density of 28.17 Wh/kg with the maximum power density of 4160 W/kg, whereas commercially applied YP-50//YP-50 shown a maximum energy density of 16.32 Wh/kg with a maximum power density of 2977 W/kg. This systematic method could open up a state-of-the-art approach to apply PNCG in a plethora of energy storage applications.

**Table 4.2:** Comparison of electrochemical performance of various porous carbon

Electrode Material	C (Fg <sup>-1</sup> )	E <sub>max</sub> (Wh Kg <sup>-1</sup> )	P <sub>max</sub> (kW Kg <sup>-1</sup> )	Current Collector	Electrolyte	Ref.
Carbon nano-cages	313	6	22	Ni-foam	6M KOH	44
Activated carbon	855	39	23	Graphene foam	0.5M H <sub>2</sub> SO <sub>4</sub>	45
Zeolite-templated carbon	273	8	98000	Gold (Au)	1M H <sub>2</sub> SO <sub>4</sub> or 0.5M KOH	46
Graphene nanosheets	480	83	426	Carbon paper	LiCl/ LiCl-PVA hydrogel	47
Activated carbon	351	39	1.0	Glassy carbon	1M H <sub>2</sub> SO <sub>4</sub> / 2M Li <sub>2</sub> SO <sub>4</sub> /6M KOH	48
Activated carbon	451	11	125	SS mesh	1M H <sub>2</sub> SO <sub>4</sub>	49
Activated carbon	258	5	10	Ni- foam	6M KOH	50
Graphene	390	55	1800	Ni foam	BMIMBF4	51
Activated biomass	200	6	8	Gold / Stainless steel	1M H <sub>2</sub> SO <sub>4</sub> / 1M TEABF <sub>4</sub> /AN/neat EMImTFSI	52
Activated carbon	221	5	2500	Ni Foam	6M KOH	53
Graphene aerogels	318	60	900	Ni foam	6M KOH/ EMIMTFSI-80	54
Activated carbon	261	4	10	Ni Foam	6M KOH	55
Template- carbon	337	10	14.4	Ni foam	6M KOH	56
PNCG	205	28	4.2	Graphite foil	3M KOH	This work

## 4.5 References

1. D.A. Lashof, D.R. Ahuja, Relative contributions of greenhouse gas emissions to global warming, *Nature* 344 (1990) 529-531.
2. S. Chu, A. Majumdar, Opportunities and challenges for a sustainable energy future, *Nature* 488 (2012) 294-303.
3. A. Hagfeldt, G. Boschloo, L. Sun, L. Kloo, H. Pettersson, Dye-sensitized solar cells, *Chem. Rev.* 110 (2010) 6595-6663.
4. A.C. Dillon, Carbon nanotubes for photoconversion and electrical energy storage, *Chem. Rev.* 110 (2010) 6856-6872.
5. E.V. Kondratenko, G. Mul, J. Baltrusaitis, G.O. Larrazabal, J. Perez-Ramirez, Status and perspectives of CO<sub>2</sub> conversion into fuels and chemicals by catalytic, photocatalytic and electrocatalytic processes, *Energy Environ. Sci.* 2013, 6 (2013) 3112-3135.
6. K. Christopher, R. Dimitrios, A Review on exergy comparison of hydrogen production methods from renewable energy sources, *Energy Environ. Sci.* 5 (2012) 6640-6651.
7. T.R. Cook, D.K. Dogutan, S.Y. Reece, Y. Surendranath, T.S. Teets, D.G. Nocera, Solar energy supply and storage for the legacy and nonlegacy worlds, *Chem. Rev.* 110 (2010) 6474-6502.
8. S. O. Amrouche, D. Rekioua, T. Rekioua, S. Bacha, Overview of energy storage in renewable energy systems, *Int. J. Hydrogen Energy* 41 (45) (2016) 20914-20927.
9. P. Simon, Y. Gogotsi, Capacitive energy storage in nanostructured carbon electrolyte Systems, *Accounts Chem. Res.* 46 (5) (2013) 1094-1103.
10. S. Najib, E. Erdem, Current progress achieved in novel materials for supercapacitor electrodes: mini review, *Nanoscale Adv.*, 1 (2019) 2817-2827.
11. J. Yin, W. Zhang, N. A. Alhebshi, N. Salah, H. N. Alshareef, Synthesis strategies of porous carbon for supercapacitor applications, *Small Methods* (2020) 1900853 (31pp).
12. F. Béguin, V. Presser, A. Balducci, E. Frackowiak, Carbons and electrolytes for advanced supercapacitors, *Adv. Mater.* 26 (2014) 2219-2251.
13. Q. Wang, J. Yan, Z. Fan, Carbon materials for high volumetric performance supercapacitors: design, progress, challenges and opportunities, *Energy Environ. Sci.* 9 (2016) 729-762.
14. L.L. Zhang, X.S. Zhao, Carbon-based materials as supercapacitor electrodes, *Chem. Soc. Rev.* 38 (2009) 2520-2531.

15. R. Raccichini, A. Varzi, S. Passerini, B. Scrosati, The role of graphene for electrochemical energy storage, *Nat. Mater.* 14 (2015) 271-279.
16. J. Wang, S. Kaskel, KOH activation of carbon-based materials for energy storage, *J. Mater. Chem.* 22 (2012) 23710-23725.
17. D. Qu, H. Shi, Studies of activated carbons used in double-layer capacitors, *J. Power Sources* 74 (1998) 99-107.
18. Y.G. Guo, J.S. Hu, L.J. Wan, Nanostructured materials for electrochemical energy conversion and storage devices, *Adv. Mater.* 20 (15) (2008) 2878-2887.
19. R. Liu , S. Sun , R. Zhong , H. Zhang , X. Wu, Nitrogen-doped microporous carbon coated on carbon nanotubes for high performance supercapacitors, *Microporous and Mesoporous Mater.* 305 (2020) 110300.
20. Q. Fan, M. Yang, Q. Meng, B. Cao, Y. Yu, Activated-nitrogen-doped graphene-based aerogel composites as cathode materials for high energy density lithium-ion supercapacitor, *J. Electrochem. Soc.* 163 (8) (2016) A1736-A1742.
21. Q. Abbas, R. Raza, I. Shabbir, A.G. Olabi. Heteroatom doped high porosity carbon nanomaterials as electrodes for energy storage in electrochemical capacitors: A review. *J. Sci-Adv Mater Dev* 4 (2019) 341-352.
22. Y. Huang, S.L. Candelaria, Y. Li, Z. Li, J. Tian, L. Zhang, G. Cao, Sulfurized activated carbon for high energy density supercapacitors, *J. Power Sources* 252 (2014) 90-97.
23. C. Wang, Y. Zhou, L. Sun, Q. Zhao, X. Zhang, P. Wan, J. Qiu, N/P-Codoped thermally reduced graphene for high-performance supercapacitor applications, *J. Phys. Chem. C* 117 (2013) 14912-14919.
24. J. Han, L.L. Zhang, S. Lee, J. Oh, K.-S. Lee, J.R. Potts, J. Ji, X. Zhao, R.S. Ruoff, S. Park, Generation of B-doped graphene nanoplatelets using a solution process and their supercapacitor applications, *ACS Nano* 7 (2013) 19-26.
25. L. Hou, L. Lian, D. Li, G. Pang, J. Li, X. Zhang, S. Xiong, C. Yuan, Mesoporous N-containing carbon nanosheets towards high-performance electrochemical capacitors, *Carbon* 64 (2013) 141-149.
26. J. Zhou, J. Lian, L. Hou, J. Zhang, H. Gou, M. Xia, Y. Zhao, T.A. Strobel, L. Tao, F. Gao, Ultrahigh volumetric capacitance and cyclic stability of fluorine and nitrogen co-doped carbon microspheres, *Nat. Commun.* 6 (2015) 8503-8510.
27. Balaji Padya, N. Ravikiran, Ravi Kali, N. Narasaiah, P. K. Jain, High thermal energy storage and thermal conductivity of few-layer graphene platelets loaded phase change

materials: A thermally conductive additive for thermal energy harvesting, *Energy Storage* 2 (6) (2020) 199 (8pp).

28. Balaji Padya, Ravi Kali, N. Ravikiran, N. Narasaiah, P.K. Jain, Constructing graphene-coupled nitrogen-doped carbon-based all-carbon hybrid for hybrid Li-ion supercapbattery: An investigation and insight into “charge-averaged” charge/discharge voltage analysis, *J Alloys and Compd.* 872 (2021) 159660 (9pp).
29. M. S. Dresselhaus, A. Jorio, M. Hofmann, G. Dresselhaus, R. Saito, Perspectives on carbon nanotubes and graphene Raman spectroscopy, *Nano Lett.* 10 (2010) 751-758.
30. J.B. Wu, M. L. Lin, X. Cong, H.N. Liu, P. H. Tan, Raman spectroscopy of graphene-based materials and its applications in related devices, *Chem. Soc. Rev.* 2018, 47 (2018) 1822-1873.
31. F. Tuinstra, J.L. Koenig, Raman spectrum of graphite, *J. Chem. Phys.* 53 (1970) 1126-1130.
32. A.C. Ferrari, Raman spectroscopy of graphene and graphite: disorder, electron-phonon coupling, doping and nonadiabatic effects. *Solid State Commun.* 143 (2007) 47-57.
33. B.A. Mei, O. Munteşari, J. Lau, B. Dunn, L. Pilon, Physical interpretations of Nyquist plots for EDLC electrodes and devices, *J. Phys. Chem. C* 122 (2018) 194-206.
34. P.L. Taberna, P. Simon, J.F. Fauvarque, Electrochemical characteristics and impedance spectroscopy studies of carbon-carbon supercapacitors, *J. Electrochem. Soc.* 150 (2003) 292-300.
35. T.S. Mathis, N. Kurra, X. Wang, D. Pinto, P. Simon, Y. Gogotsi, Energy storage data reporting in perspective-guidelines for interpreting the performance of electrochemical energy storage Systems, *Adv. Energy Mater.* 9 (2019) 1902007.
36. S. Ahmed, A. Ahmed, M. Rafat, Performance of chitosan derived activated carbon in supercapacitor, *Adv. Nat. Sci.: Nanosci. Nanotechnol.* 10 (2019) 025003.
37. J. Chmiola, G. Yushin, Y. Gogotsi, C. Portet, P. Simon, P.L. Taberna, Anomalous increase in carbon capacitance at pore sizes less than 1 nanometer, *Science* 313 (2006) 1760-1763.
38. C. Largeot, C. Portet, J. Chmiola, P.-L. Taberna, Y. Gogotsi, P. Simon, Relation between the Ion Size and Pore Size for an Electric Double-Layer Capacitor, *J. Am. Chem. Soc.* 130 (2008) 2730–2731.
39. J. Kang, S. Atashin, S.H. Jayaram, J.Z. Wen, Frequency and temperature dependent electrochemical characteristics of carbon based electrodes made of commercialized

activated carbon, graphene and single-walled carbon nanotube, *Carbon* 111 (2017) 338-349.

40. E. Frackowiak, G. Lota, J. Machnikowski, C. Vix-Guterl, F. B'eguin, Optimisation of supercapacitors using carbons with controlled nanotexture and nitrogen content, *Electrochim. Acta* 51 (2006) 2209-2214.

41. D. He, J. Niu, M. Dou, J. Ji, Y. Huang, F. Wang, Nitrogen and oxygen co-doped carbon networks with a mesopore-dominant hierarchical porosity for high energy and power density supercapacitors, *Electrochim. Acta* 238 (2017) 310-318.

42. Y. Zhou, Z. Song, Q. Hu, Q. Zheng, N. Jiang, F. Xie, W. Jie, C. Xu, D. Lin, Hierarchical nitrogen-doped porous carbon/carbon nanotube composites for high-performance supercapacitor, *Superlattices Microstruct.* 130 (2019) 50-60.

43. L. Wan, W. Wei, M. Xie, Y. Zhang, X. Li, R. Xiao, J. Chen, C. Du, Nitrogen, sulfur co-doped hierarchically porous carbon from rape pollen as high-performance supercapacitor electrode, *Electrochim. Acta* 311 (2019) 72-82.

44. J. Zhao, H. Lai, Z. Lyu, Y. Jiang, K. Xie, X. Wang, Q. Wu, L. Yang, Z. Jin, Y. Ma, J. Liu, Z. Hu, Hydrophilic hierarchical nitrogen-doped carbon nanocages for ultrahigh supercapacitive performance, *Adv. Mater.* 27 (2015) 3541-3545.

45. T. Lin, I.-W. Chen, F. Liu, C. Yang, H. Bi, F. Xu, F. Huang, Nitrogen-doped mesoporous carbon of extraordinary capacitance for electrochemical energy storage, *Science* 350 (2015) 1508-1513.

46. M.J. Mostazo-Lopez, R. Ruiz-Rosas, A. Castro-Muniz, H. Nishihara, T. Kyotani, E. Morallon, D. Cazorla-Amoros, Ultraporous nitrogen-doped zeolite-templated carbon for high power density aqueous-based supercapacitors, *Carbon* 129 (2018) 510-519.

47. M.S. Javed, S.S.A. Shah, T. Najam, M.K. Aslam, J. Li, S. Hussain, M.A Ahmad, M Ashfaq, R. Raza, W. Mai, Synthesis of mesoporous defective graphene-nanosheets in a space-confined selfassembled nanoreactor: highly efficient capacitive energy storage, *Electrochim. Acta* 305 (2019) 517-527.

48. K. Zou, Y. Deng, J. Chen, Y. Qian, Y. Yang, Y. Li, G. Chen, Hierarchically porous nitrogen-doped carbon derived from the activation of agriculture waste by potassium hydroxide and urea for high-performance supercapacitors, *J. Power Sources* 378 (2018) 579-588.

49. C. Wang, D. Wu, H. Wang, Z. Gao, F. Xu, K. Jiang, Biomass derived nitrogen doped

hierarchical porous carbon sheets for supercapacitors with high performance, *J. Colloid Interface Sci.* 523 (2018) 133-143.

50. G. Wang, J. Zhang, S. Kuang, J. Zhou, W. Xing, S. Zhuo, Nitrogen-doped hierarchical porous carbon as an efficient electrode material for supercapacitors, *Electrochim. Acta* 153 (2015) 273-279.

51. S. Dai, Z. Liu, B. Zhao, J. Zeng, H. Hu, Q. Zhang, D. Chen, C. Qu, D. Dang, M. Liu, A high-performance supercapacitor electrode based on N-doped porous graphene, *J. Power Sources* 387 (2018) 43-48.

52. M. Sevilla, N. Diez, G.A. Ferrero, A.B. Fuertes, Sustainable supercapacitor electrodes produced by the activation of biomass with sodium thiosulfate, *Energy Storage Mater.* 18 (2019) 356-365.

53. P. Song, X. Shen, W. He, L. Kong, X. He, Z. Ji, A. Yuan, G. Zhu, N. Li, Protein-derived nitrogen doped hierarchically porous carbon as electrode material for supercapacitors, *J. Mater. Sci. Mater. Electron.* 29 (2018) 12206-12215.

54. P. Xu, Q. Gao, L. Ma, Z. Li, H. Zhang, H. Xiao, X. Liang, T. Zhang, X. Tian, C. Liu, A high surface area N-doped holey graphene aerogel with low charge transfer resistance as high performance electrode of non-flammable thermostable supercapacitor, *Carbon* 149 (2019) 452-461.

55. J. Zhou, Z. Zhang, W. Xing, J. Yu, G. Han, W. Si, S. Zhuo, Nitrogen-doped hierarchical porous carbon materials prepared from meta-aminophenol formaldehyde resin for supercapacitor with high rate performance, *Electrochim. Acta* 153 (2015) 68-75.

56. M. Chen, H. Xuan, X. Zheng, J. Liu, X. Dong, F. Xi, N-doped mesoporous carbon by a hard-template strategy associated with chemical activation and its enhanced supercapacitance performance, *Electrochim. Acta* 238 (2017) 269-277.

## List of Supplementary Files

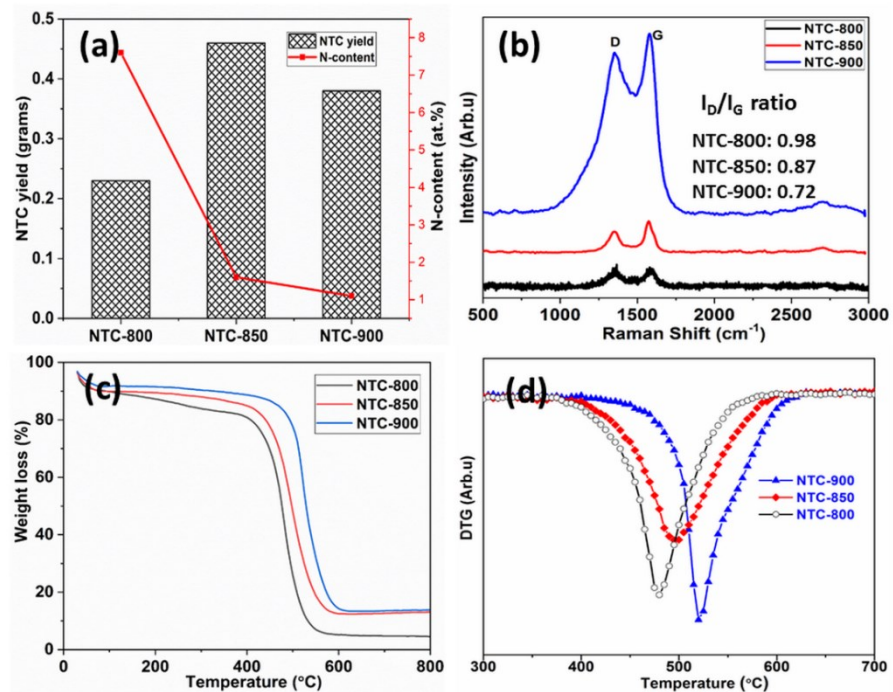


**Fig.S4.1.** NTC growth: (a) NTC-yield and N-content, (b) Raman signatures, (C) weight loss and (d) derivative weight loss.

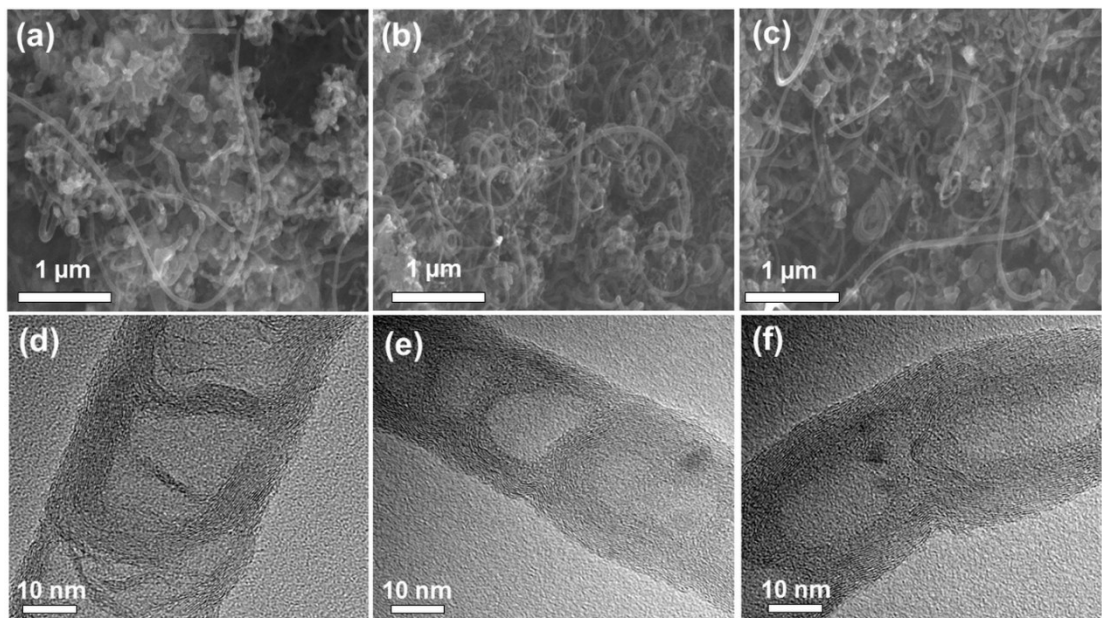


**Fig.S4.2.** SEM images of (a) NTC-800, (b) NTC-850, and (c) NTC-900; TEM image of (d) NTC-800, (e) NTC-850, and (f) NTC-900.

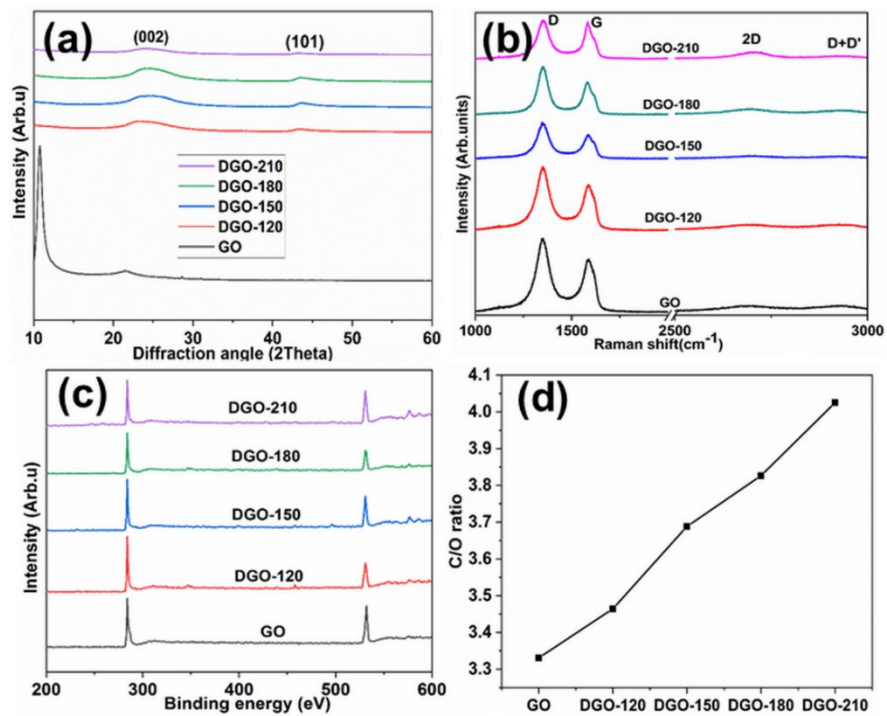


**Fig.S4.3.** DGO preparation: (a) XRD pattern (b) Raman signatures (c) XPS-wide scan and (d) C/O ratio.

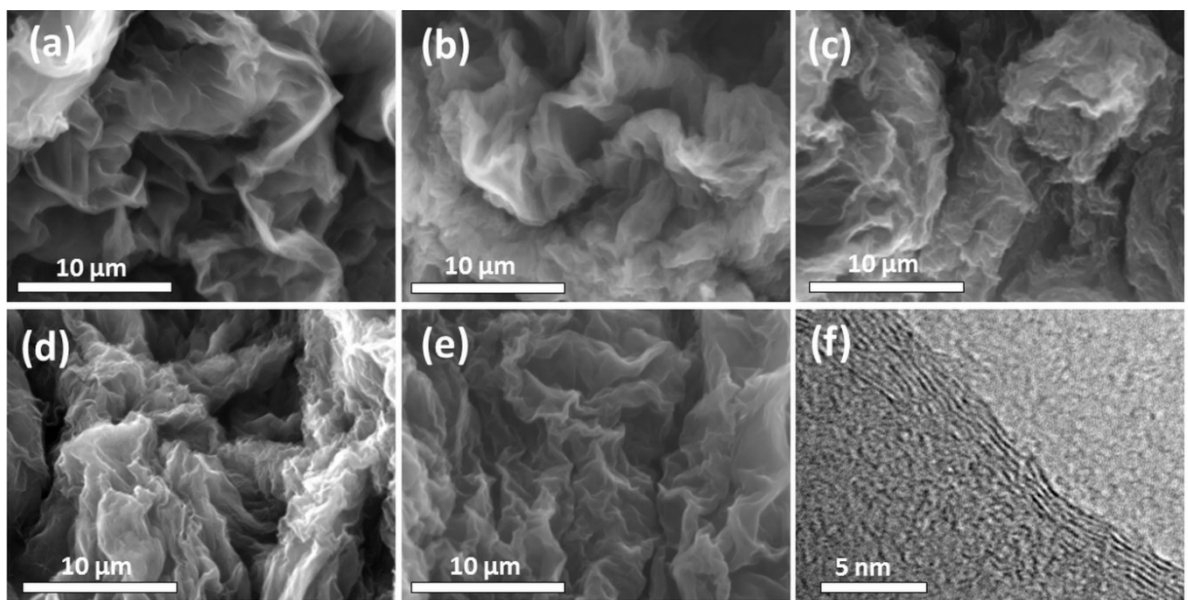


**Fig.S4.4.** SEM images of (a) GO (b) DGO-120, (c) DGO-150 (d) DGO-180, (e) DGO-210; TEM image of (f) DGO-210.

## CHAPTER-5

---

### **Surface-etched nanoscaled-graphene platelets based porous carbon for supercapacitor**

---

The technical content described in chapter-5 is based on the work published in Colloids and Surfaces A 609 (2021) 125587.

#### **5.1. Introduction**

In recent years, the critical issues with the use of conventional sources for energy and its derivatives posing severe environmental pollution, and global warming (1-4). To reduce the burden on them, the usage of renewable sources for sustainable developments are of immense interest (5-7). Furthermore, the integrated energy storage devices (IESD) drawn a great deal of consideration, as the majority of renewable sources are intermittent in nature. IESD does not show impression unless an efficient energy storage system is coupled with sustainable appliances. Presently, supercapacitors represent research hotspot owing to their exceptional fast charging, high-power density, and long-life cycle performance (8, 9). In this connection, wide range of materials are exploited as electrode materials for supercapacitor but, carbonaceous materials are widely explored as electrode material for electric double-layer capacitors (EDC) as they possess exceptional thermal, mechanical, electrical, electronic and chemical characteristics (10,11). The high surface area with controlled porosity, pore-size distribution, wettability of electrode materials with electrolyte and conductivity are crucial factors in determining their application in capacitive energy storage (12). Interestingly, graphene-related materials attracted considerable attention due to their very high surface area and exotic characteristics (13-15).

Till date, there are numerous methods to produce graphene are available, but an efficient technology of fabrication of graphene is a severe obstacle holding down progress in experimental studies, and marketability of graphene and graphene-based nanostructures. Each process employed in fabrication of graphene is plagued by severe limitations (16-24). Production of high-quality graphene in bulk quantity is still a challenge even though it is discovered in 2004. To move from the laboratory to commercial applications, it is high time to develop an industrially viable route to produce graphene in a large quantity with minimal defects. Fascinatingly, the carbonaceous materials with high surface area, high electrical conductivity, and suitable pore size distribution are the right candidate as electrode material for EDC (13-15). In comparison to others, utilization of solvent-phase exfoliation with co-solvent strategy to convert thick graphite

into low-dimensional sheets via multi-stage exfoliation of graphite makes our study unique and exclusive.

Though the graphene possesses high surface area, restacking nature of it restricted full utilization for electrochemistry. As a way out to increase surface area, the traditionally proven chemical activation is adopted. Additionally, the surface area could be increased by widely used surface modification through pyrogenic agents via activation (25). The chemical-assisted etching is a template-free effective method to produce carbonaceous (biomass-derived carbon, carbon nanotubes, aerogels, graphene and fibres) porous materials with the action of etching-away. Generally, the reagents such as NaOH, KOH, H<sub>3</sub>PO<sub>4</sub> and ZnCl<sub>2</sub> are used to create porosity in materials (25-33). Among all, KOH found to be effective to generate controlled-porosity with a selectively monitored pore size (25). As of today, most of the commercially available activated carbon materials are processed through KOH activation. However, the pore size and its distribution, oxygen content obviously depend on the activation processing parameters (mass ratio of KOH–carbon, activation temperature, heating rate, incubation duration, and the form of KOH, graphitization of carbon, and kind of carbon sources) to generate interconnected pores (25-33). Involvement of various processing factors and parameters makes the underlying mechanism very complex to understand clearly. However, phenomenon of formation of K<sub>2</sub>CO<sub>3</sub> as an intermediate product and then, it is transformed into carbon monoxide and metallic potassium is widely accepted (25). The chemical activation process could aid in significant surface area as well as yield in comparison to physical activation (CO<sub>2</sub> or steam) owing to lower processing temperature, and time. Activated porous carbon finds application in cosmetics, chemical warfare, hydrogen storage, energy storage/conversion and so on owing to its remarkable characteristics (25-33).

As of now, the theoretical high surface area of graphene sheets tempted the research community to extensively use it as electrode materials in the field of energy storage and conversion. Nevertheless, in reality, the restacking nature of sheet-like structured graphene due to van der Waal forces make them in agglomerate and hence, actual surface area reduces by multifold. In order to by-pass the restacking, the sheets with truncated shapes, irregular edges and porosity-rich structure are preferable. The activation process converts the smooth surfaces of the thin sheets into scabrous and bumpy to an extent, thus, could lay a feasible route to avoid restacking.

This study proposes the process of delamination of graphite to small-scaled graphene via liquid phase exfoliation in a scalable quantity by using multistage-exfoliation of graphite and

then, fragmentation in co-solvent. The phenomenon of complex fluid dynamics and shear mixing exist in this process dominates in separating graphene sheets from the bulk material. This process is most effective and feasible in generating thinner graphene nanoplatelets in bulk quantity. Herein, nanoscaled-graphene nanoplatelets (NGNS) were prepared from re-expanded graphite and fragmentation through the co-solvent mixture. A probable mechanism for delamination of layered-material into sheet-like structured NGNS is proposed. Then, the KOH-assisted thermochemical activation of NGNS route is deployed to create porosity and controlled pore-size distribution suitable for electrolyte ion-diffusion with minimal charge transfer resistance to enhance electrochemical characteristics.

## 5.2. Experimental

### 5.2.1 Materials and reagents

All the chemicals, reagents and solvents are of analytical grade and used without further purification. Ultrapure deionized water (18.2 MΩ.cm) produced by Milli-Q system used as solvent throughout the study. Natural graphite flakes (NGF, -60+72 BS mesh, Oxeeco Technologies Pvt. Ltd, India) were used as a precursor for the synthesis of exfoliated graphite. Sulphuric acid (Merck, India) and hydrogen peroxide (Merck, India), Dimethyl sulfoxide (DMSO), Dimethyl formamide (DMF) and N-methyl pyrrolidone (NMP, Finar Limited India) are used as a solvent for processing.

### 5.2.2 Preparation of NGNS and its surface modification

NGNS prepared via intercalation of NGF with oxidizing agents, and two-stage exfoliation process followed by high energy fragmentation with minor modifications to the process mentioned elsewhere (34). NGF was chemically treated to generate intercalation-induced expandable graphite (IIG). In brief, 20 g of NGF was mixed with H<sub>2</sub>SO<sub>4</sub> and H<sub>2</sub>O<sub>2</sub> (10:2 by volume) solution and chemically treated for 6 h using mechanical mixer, washed with copious amount of water to remove excess chemicals, and dried at 80 °C for 10 hours to form IIG. IIG was transformed into expanded graphite (EG) via microwave irradiation-assisted exfoliation at the power of 600 W for a few seconds. The solution-phase exfoliation (DMSO: water 8:2 v/v) of EG converted them into graphene nanoplatelets (GNP) by kitchen mixer. The mixed solvent strategy is adapted to minimize the enthalpy of mixing to disperse GNP, and produce them with ease (35). The same process was repeated for chemical treatment and re-exfoliation of GNP with microwave-assisted exfoliation (600 W) followed by kitchen-mixer fragmentation and ultrasonication fragmentation for 1 hour and 1 hour, respectively to obtain uniform NGNS dispersion. A co-solvent with DMF and water mixture (8:2 v/v) was used for fragmentation in

later stage. Density-assisted separation based on centrifugation was performed at 2000 rpm for 30 minutes as the finer and coarser were separated. NGNS was mixed with KOH (1:3 w/w), and thermochemical activation was performed at 400 °C for 1 hour and 750 °C for 1.5 hours. The heating rate of 3 °C/min was maintained during heating the furnace. Activated NGNS was designated as aNGNS.

### 5.2.3 Instrumentation and characterization

The morphology, and microstructure of NGNS and aNGNS at different stages were characterized using scanning electron microscope (SEM, Model Gemini-500, Zeiss, Germany), transmission electron microscope (TEM, Model FEI Technai G<sup>2</sup> S-Twin, USA), respectively. Raman spectroscopy (Lab Ram HR800 Raman spectrometer; 514.5 nm green line of Ar<sup>+</sup> ion laser was used as the excitation source) was used for knowing the crystallinity and number of layers in NGNS. Nitrogen adsorption/desorption at 77 K was carried out on an ASAP 2020 analyzer (Micrometrics, USA) to investigate the pore structures of the aNGNS. All electrochemical measurements were performed in a Swagelok-like 2-electrode configuration for practical application. The electrochemical cell containing 3 M KOH used as the electrolyte. The working electrodes were prepared by homogeneously mixing electroactive material (85 %), acetylene black (10 %) and polytetrafluoroethylene (5 %) in N-methyl pyrrolidone solvent. After thorough mixing, the slurry was uniformly casted onto a flexible graphite foil (10 mm x 10 mm) by doctor blade process, and then dried at 80 °C in a vacuum oven for 20 hours. The electrochemical cell was fabricated in sandwich-type configuration by inserting a Whatman separator in between the electrodes. Cyclic voltammetry (CV) and galvanostatic charge/discharge tests (GCD) and electrochemical impedance spectroscopy (EIS) were carried out at room temperature through electrochemical workstation (CHI 635A). The EIS analyses were measured at open circuit potential of 5 mV sinusoidal voltage in the frequency range of 0.01 Hz–10 kHz.

The electrochemical performance of the electrode material was estimated based on galvanostatic constant current charge-discharge profile. The following analytical formulae were employed to calculate the performance parameters of sandwich-type supercapacitor cell.

$$\text{Specific capacitance (F/g)} \quad C_g = 4. I. \Delta t / (\Delta V. m) \quad (1)$$

$$\text{Specific energy density (Wh/kg)} \quad E_g = \left(\frac{1}{2}\right) \cdot C_g \cdot \Delta V^2 \cdot (1000/3600) \quad (2)$$

$$\text{Specific power density (W/kg)} \quad P_g = E_g \cdot 3600 / \Delta t \quad (3)$$

where m, I,  $\Delta t$  and  $\Delta V$  stands for the total mass of the electroactive material, constant charging-discharging current, discharge current and voltage window during the discharging process,

respectively. The electrode was prepared with the mass loading of active material in each electrode is 2.93 mg/cm<sup>2</sup>.

### 5.3. Results and discussion

#### 5.3.1 Preparation of NGNS and aNGNS

A plausible mechanism to disintegrate the finest layers from the bulk via ‘insertion-rapid escape-exfoliation-fragmentation’ strategy was proposed. It is well known fact that the 3D graphite consists of flat planes, with the planes held together by Van der Waals forces (very weak). It is intercalated by exposing it to the intercalating agent which enters in between the carbon layers of the NGF. The effectiveness of the intercalation solely depends on what type of stage it forms in IIG. Furthermore, the stage-1 will give superior results to create isolated sheets of graphene. The exfoliation process is initiated at a particular weak interlayer spacing susceptible to rupture due to the gas pressure created by microwave-induced thermal shock. The sufficient pressure needed to overcome van der Waals binding force is given by  $P = A_{Ham}/6\pi l$ , where  $A_{Ham}$  is Hamaker coefficient ( $2.37 \times 10^{-21}$  J), and  $l$  is the interlayer distance between the stacks (36). During the exfoliation method, the layers in a graphite stack try to depart due to the pressure created by escaping gaseous molecules and disrupt layers by overcoming weak van der Waals forces at weak interlayer spacing susceptible to rupture. When the pressure exceeds 2.49 MPa, the gaseous molecules try to exert the pressure and escape to create accordion-structured graphite worms (36). The accordion-structured EG worms prone to disruption of the structure, and the d-spacing significantly reduce the attractive interactions between the layers, allowing this material to be easily dispersed in mixed solvents. EG particles split as a result of the considerable internal strain created by the high pressure applied to the grains by kitchen blender and then, ultrasonication. The tip of the ultrasonic sonotrode oscillates at a fixed frequency, and produces a conical field of high energy in the fluid. The solution within this conical area undergoes nucleate boiling, and bubble collapse that is the primary mechanism by which ultrasonic energy delaminate GNP into separated NGNS. When an ultrasonic wave passes through a liquid, acoustic cavitations takes place, and produces localized hot spots with high temperature and local pressure as high as  $\sim 400$ -500 atm, with heating and cooling rates more than 10<sup>9</sup> K/s (37). Acoustic cavitations near a solid surface create localized erosion, induce high-velocity interparticle collisions, cause fragmentation of brittle materials, and improve mass transport. In such a fashion, ‘insertion-rapid escape-exfoliation-fragmentation’ was attributed to intercalation, thermal shock, worm-like structure, and delamination, respectively. The typical procedure involved in the preparation of NGNS and aNGNS was depicted (schematic) in **Fig.5.1**.

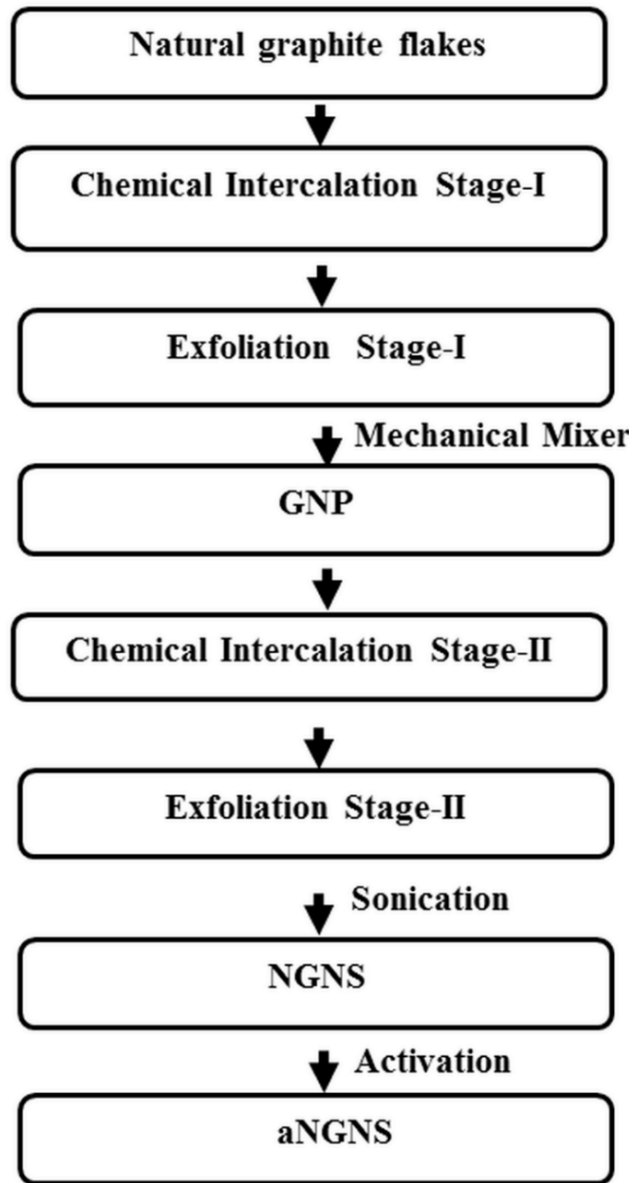


**Fig. 5.1** Schematic diagram indicating the flow-chart for the preparation of aNGNS.

**Fig.5.2. (a & b)** presents the high-resolution TEM images of GNP and NGNS, respectively. The opacity of NGNS shows that the electron beam quickly penetrates thin structures implies it contains minimal graphene layers. The GNP from stage-1 EG consists of 15-24 layers, whereas NGNS comprises  $\leq 7$  layers. The majority of NGNS consist layers in the range of 3-7 layers. It confirms that the highly efficient re-exfoliation technique could generate thin platelets with very minimal layers. Density-assisted separation based on centrifugation could able to separate NGNS depending upon their number of layers. The supernatant at the top and bottom in a vial are having low and more layers in a stack, respectively. The high degree of exfoliation

and delamination could reduce the number of layers in a stack. Well-ordered distinct layers are clearly observed implies the high graphitization degree with much better crystallinity.

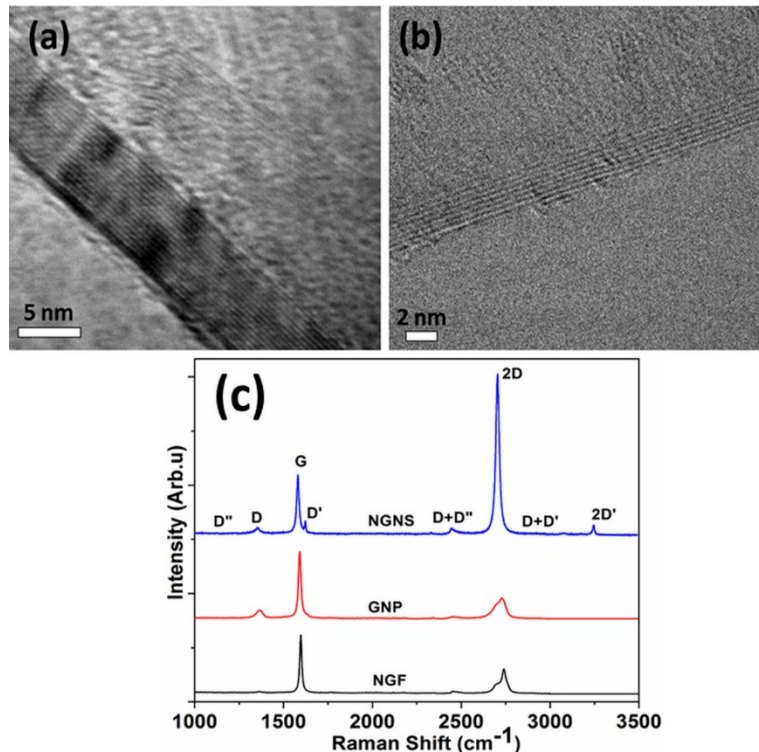


**Fig. 5.2** High-resolution TEM images of GNP (a), NGNS (b) and Raman signatures (c).

Raman spectroscopy is a versatile tool to analyze defect density, strain and crystallinity of carbonaceous materials (38). A typical Raman spectrum of a carbonaceous material consist of various bands such as D'', D, G, D', D+D'', 2D, D+D', 2D' at frequency around 1140.1, 1355.3, 1580.04, 1625.09, 2450.5, 2700.30, 2954.45 and 3245.73  $\text{cm}^{-1}$ , respectively (39-41). The main features such as D, G, D', and 2D bands, were analyzed thoroughly for knowing the changes in the number of layers in a stack. These bands were associated with defects, graphitization, strain and number of layers to D-band, G-band, D'-band and 2D band, respectively (42). **Fig.5.2c** presented the typical Raman spectrum for NGF, GNP and NGNS. The intensity of the D-band peak of NGNS was drastically increased as compared to NGF, indicating the increase in defects. A small hump at D'-band is an indication of the presence of strain-induced structural changes. The intense peak at D'-the band was noticed for NGNS as compared to NGF and GNP. Criteria mentioned above were ascribed to a large amount of strain-induced due to 2-stage exfoliation, mechanical mixer and ultrasonication. The position and shape of the 2D-band explain the number of layers present in a stack. 2D-band peak for NGNS was intense and quasi-symmetric in nature. Such a sharp peak with very less full-width half maxima is an indication for the formation of

few-layer graphene sheets. Two-stage exfoliation process (reexfoliation) could able to transform NGF into NGNS with minimal layers.

### 5.3.2 Porosity and electrochemical properties of aNGNS

**Fig.5.3 (a & b)** presents the surface morphology of NGNS and aNGNS. It is evident that the edges of aNGNS are altered due to pyrogenic activation whereas smooth surfaces are noticed for NGNS. The irregular structured edges of aNGNS confirms that the chemical activation leads to carbon etch-away reaction. The etch-away reaction created by KOH removes the material from a sheet and create the pores. Such pores are responsible for the transport of electrolyte ions during the electrochemical analysis.

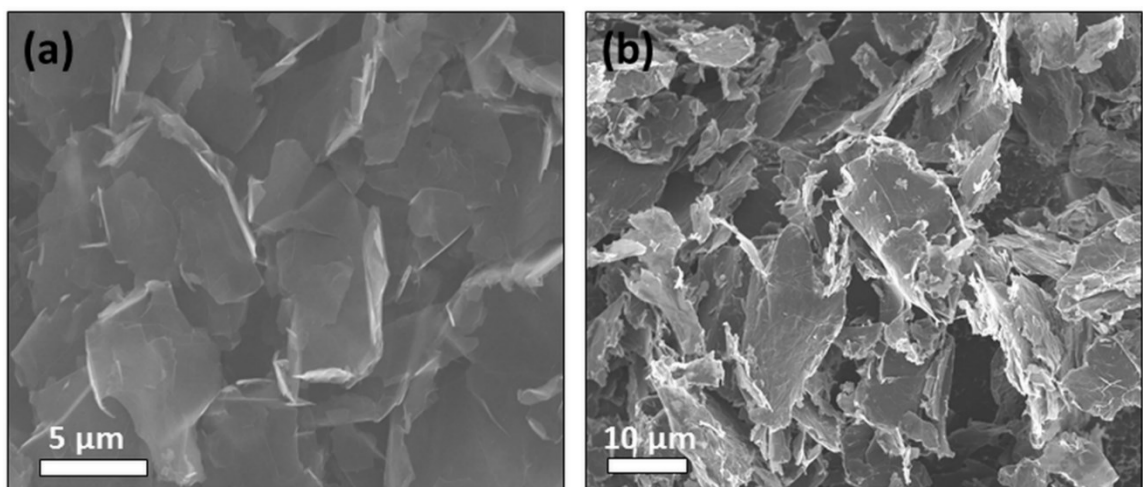


**Fig.5.3** SEM images of NGNS (a), and aNGNS (b) in powder form.

The pore structure of aNGNS was quantitatively investigated by using nitrogen adsorption/desorption analysis. **Fig.5.4** represents the nitrogen adsorption-desorption of aNGNS. From the isotherm, the adsorption capacity increases rapidly, which indicated that the surface of the material has micro and mesopores. The adsorption capacity of material continued to increases (nearly straight line in the low relative pressure) with an increase in relative pressure up to 1.00 and found that the adsorption-desorption curves do not coincident with each other. Such a hysteresis loop is mostly noticed in the case of micro/mesoporous structures (43). A typical graph to assess the surface area and porous structure exhibited type-IV characteristics with the presence of H4-type hysteresis loops at relative pressure in the range of 0.43 to 0.97 was illustrated in **Fig.5.4a**. It indicates that these systems contain micro/mesopores with mesopores are intensive dominant. This implies multilayer adsorption could occur within the wide pores of the mesoporous materials. **Fig.5.4b** shows that aNGNS exhibited pore size distribution in the range of 18-500 Å with dominant in the range of 18-40 Å which could accommodate OH<sup>-</sup> ions. aNGNS demonstrated pore volume of 0.58 cm<sup>3</sup>/g and it is quite rich in mesopores to support ions-

transport. NGNS and aNGNS presented surface area of 116 and 753 m<sup>2</sup>/g, respectively. The activation process resulted in tremendous increase in surface area.

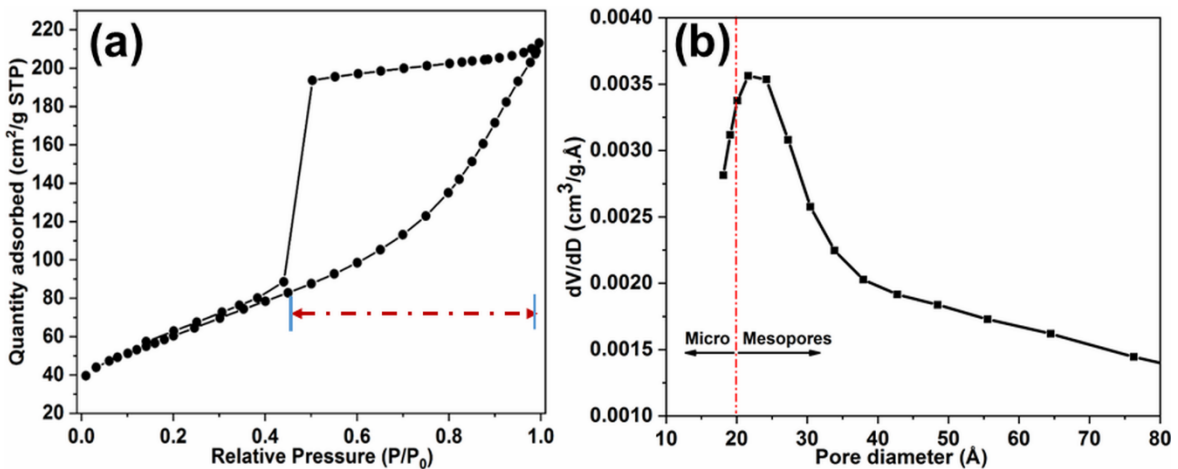


**Fig.5.4** Nitrogen adsorption–desorption isotherm (a) and pore size distribution (b) of aNGNS.

**Fig.5.5** presents the electrochemical properties of aNGNS. **Fig.5.5a** presents the near rectangular-shaped CV curves indicated that it is a typical characteristic of EDC, and does not consist of any redox reaction (44). The charging-discharging lines are straight, and indicated a very small initial voltage drop during discharging as illustrated in **Fig.5.5b**. The specific capacitance of aNGNS was illustrated in **Fig.5.5c**. aNGNS exhibited gravimetric specific capacitance of 242, 212, 178, 154, 119 F/g at the current density of 0.5, 1, 2, 3, 5 A/g, respectively. The capacity retention of the electrode material was quite good and was noticed to be 97.21 % after 1000 cycles performed at 0.5 A/g. The device shown an exceptionally outstanding energy density of 27.22 Wh/kg at a power density of 230.56 W/kg at constant current density of 0.5 A/g. **Fig.5.6** shows the Ragone plot comprising specific energy density (Wh/kg) versus specific power density.

The frequency response behavior of aNGNS was presented in **Fig.5.7**. The resultant Nyquist plot was composed of an arc (very small) in the high-frequency region, and a straight line in the lower frequency region, as shown in **Fig. 5.7a**. The EIS curve exhibited a nearly straight vertical line and semicircle at low frequency and high frequency, respectively similar to previous reports (45-48). The intercept to the x-axis ( $Z_{\text{real}}$ ) at higher frequency infers the electrode resistance ( $R_s$ ) value, and the diameter of the semicircle indicates the interfacial charge transfer resistance ( $R_{\text{ct}}$ ). The value of  $R_s$  was found to be 0.82 Ω indicates that the electrode material and electrolyte along with current collector had high electrical conductivity with exceptional electron transport. The semicircle established to be very small (~2.61 Ω) conveys the ion transport takes place at a fast rate due to lower resistance accompanied by multi-

channelled porous structure (49). The hierarchical pores comprising suitable micro/mesopores induced ion-transport with very short diffusion path are responsible for exceptional electrochemical characteristics in various kinds of porous carbonaceous materials (50, 51).

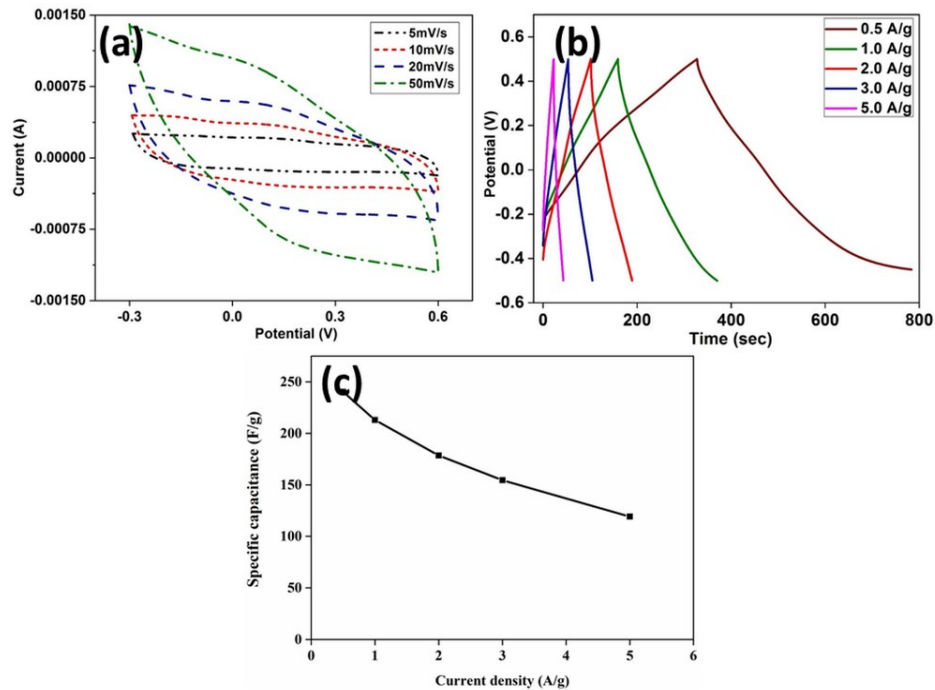


**Fig.5.5.** Electrochemical properties of aNGNS: Cyclic voltammetry (a), Charging-discharging curves (b), Specific capacitance (c).

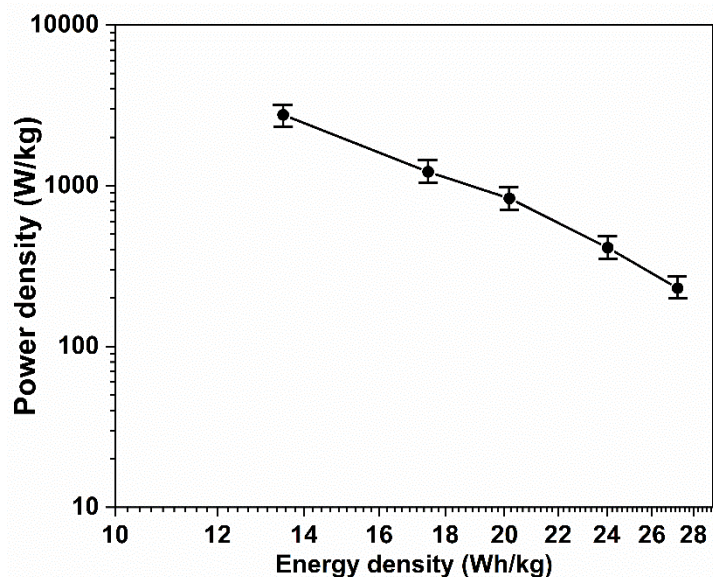


**Fig.5.6** Ragone plot of aNGNS based supercapacitor cell.

Interestingly, the mechanism of ion transport is relied on many factors such as electrolyte viscosity, cation/anion interaction, wettability of electrode with electrolyte and pore size along with their pore size distribution, and surface area.

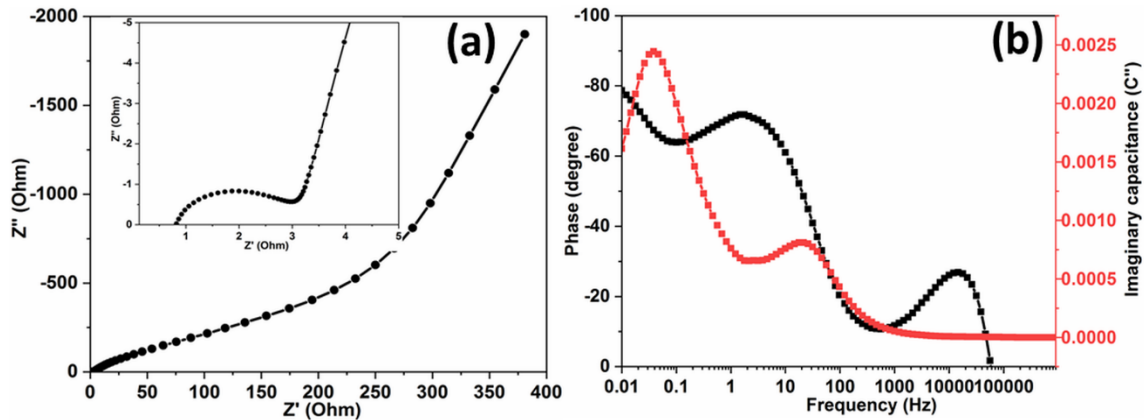


**Fig.5.7.** Frequency-response analysis by electrochemical impedance spectroscopy: Nyquist plot (a), and bode plot (phase vs. frequency) (b) and imaginary capacitance vs. frequency (b).

The ion size of the electrolyte and the pore size distribution of the electrode play crucial role in ion-transport flow such as the small pores blocks the ion and suitable pore aid in full utilization of porous structures through ion migration. The pores with smaller size do not allow ions migration and are of no use, as it does not participate in electrochemistry. The porosity along with the pore size distribution influences the specific capacitance significantly. Owing to the graphitized and porosity-rich structure of aNGNS resulted in exceptionally high specific capacitance. **Fig.5.7b** depicts the frequency response of aNGNS. In a Bode plot, the supercapacitor has shown maximum phase angle of 79.1 confirming the best suitability for EDC mechanism. However, aNGNS presented two dominant peaks in imaginary capacitance that arises due to interfacial charge transfer accounted to wide range distribution of pore sizes in bimodal distribution. The variable and sparse size distribution of pores lead to resistance for ion-diffusion creating two dominant peaks. The porosity-tuned material with suitable pore size distribution are of considerable interest to apply them for EDC. Similarly, various groups have explored a group of porous graphenaceous materials to exploit them to full extent for supercapacitors as indicated in **Table.5.1**. aNGNS performed exceptionally well in comparison to other porous materials (52-58).

**Table 5.1:** Comparison of supercapacitor performance of graphene-based porous materials

<b>Materials</b>	<b>Electrolyte</b>	<b>current density</b>	<b>Capacitance</b>	<b>Ref.</b>
		(A/g)	(F/g)	
Activated N-MEGO	1M KOH	0.1	132.4	52
Porous carbon sheets	6M KOH	1	166	53
	0.5 Na <sub>2</sub> SO <sub>4</sub>	0.5	73	53
Activated graphene	1M H <sub>2</sub> SO <sub>4</sub>	0.1	240 <sup>a</sup>	54
Porous graphene	2M KOH	1.5	189	55
Porous graphene	6M KOH	0.2	284	56
Activated microporous carbon nanoplatelets	1M H <sub>2</sub> SO <sub>4</sub>	0.1	264	57
CO <sub>2</sub> -activated graphene	1M H <sub>2</sub> SO <sub>4</sub>	1	278.5 <sup>a</sup>	58
aNGNS	3M KOH	0.5	242	This work

<sup>a</sup>values of specific capacitance for 3-electrode configuration

As per previous reports, the notable exceptional electrochemical properties are observed with different kinds of carbonaceous materials in comparison with our work such as porous carbon sheets (6 M KOH, 1 A/g, 166 F/g), activated graphene (1M H<sub>2</sub>SO<sub>4</sub>, 0.1 A/g, 240 F/g), porous graphene (6M KOH, 0.2 A/g, 284 F/g), carbon nanoplatelets (1M H<sub>2</sub>SO<sub>4</sub>, 0.1 A/g, 264 F/g), CO<sub>2</sub>-activated graphene (1M H<sub>2</sub>SO<sub>4</sub>, 1 A/g, 278.5 F/g) reported by Chen et al. (53), Seredych et al. (54), Wang et al. (56), Yun et al. (57), and Yun et al. (58), respectively. In contrast, our material aNGNS exhibited (3M KOH, 242 F/g) at 0.5 A/g with 3M KOH electrolyte. It confirms that aNGNS has shown remarkable electrochemical properties on par with previously reported studies.

#### 5.4. Conclusions

To conclude, the facile route was formulated to prepare NGNS and aNGNS via re-exfoliation and fragmentation process of expanded graphite, and pyrogen-assisted activation process, respectively. The meso-porosity dominated aNGNS exhibited specific capacitance of

242 F/g at the current density of 0.5 A/g with energy density of 27.22 Wh/kg at a power density of 230.56 W/kg in an alkaline electrolyte.

## 5.5 References

1. M. Hook, X. Tang, Depletion of fossil fuels and anthropogenic climate change-A review, *Energy Policy* 52 (2013) 797-809.
2. Y. Lu, J. Yuan, X. Lu, C. Su, Y. Zhang, C. Wang, X. Cao, Q. Li, J. Su, V. Ittekot, R. A. Garbutt, S. Bush, S. Fletcher, T. Wagey, A. Kachur, N. Sweijd, Major threats of pollution and climate change to global coastal ecosystems and enhanced management for sustainability, *Environ. Pollut.* 239 (2018) 670-680.
3. H. Galbraith, R. Jones, R. Park, J. Clough, S. Herrod-Julius, B. Harrington, G. Page, Global climate change and sea level rise: potential losses of intertidal habitat for shorebirds, *Waterbirds* 25 (2) (2002) 173-183.
4. W.W.L. Cheung, R. Watson, D. Pauly, Signature of ocean warming in global fisheries catch, *Nature* 497 (7449) (2013) 365-368.
5. P. Simon, Y. Gogotsi, Materials for electrochemical capacitors, *Nat. Mater.* 7 (2008) 845–854.
6. J. Hassoun, F. Bonaccorso, M. Agostini, Marco Angelucci, M.G. Betti, R. Cingolani, M. Gemmi, C. Mariani, S. Panero, V. Pellegrini, B. Scrosati, An advanced Lithium-ion battery based on a graphene anode and a Lithium iron phosphate cathode, *Nano Lett.* 14 (2014) 4901–4906.
7. H. Nazir, M. Batool, F. J. B. Osorio, M. Isaza-Ruiz, X. Xu, K. Vignarooban, P. Phelan, Inamuddin, A. M. Kannan, Recent developments in phase change materials for energy storage applications: A review, *Int. J. Heat Mass Transf.*, 129 (2019) 491–523.
8. B.E. Conway, *Electrochemical capacitors: scientific fundamentals and technological applications*, Kluwer, Dordrecht, the Netherland, (1999).
9. E. E. Miller, Y. Hua, F. H. Tezel, Materials for energy storage: review of electrode materials and methods of increasing capacitance for supercapacitors, *J. Energy Storage*, 20 (2018) 30–40.
10. A. Pandolfo, A. Hollenkamp, Carbon properties and their role in supercapacitors, *J. Power Sources* 157 (2006) 11–27.
11. Y. Zhang, Q. Wan, N. Yang, Recent advances of porous graphene: synthesis, functionalization, and electrochemical applications, *Small* 15 (2019) 1903780 (1-37).
12. A. Burke, R&D considerations for the performance and application of electrochemical capacitors, *Electrochim. Acta* 53 (3) (2007) 1083–1091.

13. R. Raccichini, A. Varzi, S. Passerini, B. Scrosati, The role of graphene for electrochemical energy storage, *Nat. Mater.* 14 (2015) 271–279.
14. Z.Y. Lin, Y. Liu, Y.G. Yao, O.J. Hildreth, Z. Li, K. Moon, C.P. Wong, Superior capacitance of functionalized graphene, *J. Phys. Chem. C* 115 (2011) 7120–7125.
15. R. Raccichini, A. Varzi, S. Passerini, B. Scrosati, The role of graphene for electrochemical energy storage, *Nat. Mater.* 14 (2015) 271–279.
16. K.S. Novoselov, A.K. Geim, S.V. Morozov, D. Jiang, Y. Zhang, S.V. Dubonos, I.V. Grigorieva, A.A. Firsov, Electric field effect in atomically thin carbon films. *Science* 306 (2004) 666-669.
17. M. Choucir, P. Thordarson, J.A. Stride, Gram-scale production of graphene based on solvothermal synthesis and sonication, *Nat. Nanotechnol.* 4 (2009) 30-33. X. Li, W. Cai, J. An, S. Kim, J. Nah, D. Yang, R. Piner, A. Velamakanni, I. Jung, E. Tutuc, S.K. Banerjee, L. Colombo, R.S. Ruoff, Large-area synthesis of high-quality and uniform graphene films on copper foils, *Science* 324 (2009) 1312 -1314.
18. C. Wu, G. Dong, L. Guan, Production of graphene sheets by a simple helium arc-discharge, *Physica E Low Dimens. Syst. Nanostruct.* 42 (2010) 1267-1271.
19. J.L. Qi, W.T. Zheng, X.H. Zhenga, X. Wang, H.W. Tian, Relatively low temperature synthesis of graphene by radio frequency plasma enhanced chemical vapor deposition, *Appl. Surf. Sci.* 257 (2011) 6531-6535.
20. W. Wang, B. Wang, J. Park, Y. Wang, B. Sun, J. Yao, Highly efficient and large-scale synthesis of graphene by electrolytic exfoliation, *Carbon* 47 (2009) 3242-3246.
21. H.C. Schniepp, J.L. Li, M.J. McAllister, H. Sai, M. Herrera-Alonso, D.H. Adamson, R.H. Prud'homme, R. Car, D.A. Saville, I.A. Aksay, Functionalized single graphene sheets derived from splitting graphite oxide, *J. Mater. Chem. B* 110 (2006) 8535- 8539.
22. S.R. Dhakate, N. Chauhan, S. Sharma, J. Taale, S. Singh, P.D. Sahare, R.B. Mathur An approach to produce single and double layer graphene from re-exfoliation of expanded graphite, *Carbon* 49 (2011) 1946-1954.
23. C. Berger, Z. Song, T. Li, X. Li, A.Y. Ogbazghi, R. Feng, Z. Dai, A.N. Marchenkov, E.H. Conrad, N. Philip, Ultrathin epitaxial graphite: 2D electron gas properties and a route toward graphene-based nanoelectronics, *J. Phys. Chem. B* 108 (2004) 19912-19916.
24. J. Wang, S. Kaskel, KOH activation of carbon-based materials for energy storage, *J. Mater. Chem.*, 2012, 22, 23710–23725.

25. S. Murali, J. R. Potts, S. Stoller, J. Park, M. D. Stoller, L. L. Zhang, Y. Zhu, R. S. Ruoff, Preparation of activated graphene and effect of activation parameters on electrochemical capacitance, *Carbon* 50 (2012) 3482-3485.
26. M. Molina-Sabio, F. Rodríguez-Reinoso, Role of chemical activation in the development of carbon porosity, *Colloids Surf. Physicochem. Eng. Asp.* 241 (2004) 15–25.
27. M.A. Lillo-Ro'denas, D. Cazorla-Amoro's, A. Linares-Solano, Understanding chemical reactions between carbons and NaOH and KOH: an insight into the chemical activation mechanism, *Carbon* 41(2) (2003) 267–275.
28. E. Raymundo-Pinero, P. Azais, T. Cacciaguerra, D. Cazorla-Amoros, A. Linares-Solano, F. Beguin, KOH and NaOH activation mechanisms of multiwalled carbon nanotubes with different structural organisation, *Carbon* 43 (4) (2005) 786–795.
29. J. Saleem, U.B. Shahid, M. Hijab, H. Mackey, G. McKay, Production and applications of activated carbon as adsorbents from olive stones, *Biomass Conv. Bioref.* 9 (2019) 775-802.
30. Y.S. Yun, M.H. Park, S.J. Hong, M.E. Lee, Y.W. Park, H.J. Jin, Hierarchically porous carbon nanosheets from waste coffee grounds for supercapacitors, *ACS Appl. Mater. Interfaces* 7 (2015) 3684–3690.
31. X. Liu, J. Li, Y. Wen, C. Ma, X. Chen, X. Wen, T. Tang, E. Mijowsk, Three-dimensional porous carbon with big cavities and hierarchical pores derived from leek for superior electrochemical capacitive energy storage, *Diam. Relat. Mater.* 98 (2019) 107522 (1-10).
32. Y.L. Zhang, C. Sun, Z.S. Tang, High specific capacitance and high energy density supercapacitor electrodes enabled by porous carbon with multilevel pores and self-doped heteroatoms derived from Chinese date, *Diam. Relat. Mater.* 97 (2019) 107455 (1-12).
33. B. Padya, N. Narasaiah, P.K. Jain, T.N. Rao, A facile co-solvent strategy for preparation of graphene nanoplatelet powder: An industrially viable innovative approach, *Ceram. Int.* 45 (2019) 13409–13413.
34. Y. Hernandez, V. Nicolosi, M. Lotya, F.M. Blighe, Z. Sun Z, S. De, I.T. McGovern, B. Holland, M. Byrne, Y.K. Gun'ko, J.J. Boland, P. Niraj, G. Duesberg, S. Krishnamurthy, R. Goodhue, J. Hutchison, V. Scardaci, A.C. Ferrari, J.N. Coleman, High-yield production of graphene by liquid-phase exfoliation of graphite, *Nat. Nanotechnol.* 3 (2008) 563-568.

35. M.J.Mcallister, J.L. Li, D.H. Adamson, H.C. Schniepp, A.A. Abdala, J. Liu, M. Herrera-Alonso, D.L. Milius, R. Car, R.K. Prud'homme, I.A. Aksay, Single sheet functionalized graphene by oxidation and thermal expansion of graphite, *Chem.Mater.* 19 (2007) 4396-4404.

36. K. Suslick, L. Crum, Encyclopedia of acoustics, Crocker MJ: John wiley & Sons. (1997) 271-282.

37. J.B. Wu, M.L. Lin, X. Cong, H.N. Liu, P.H. Tan, Raman spectroscopy of graphene-based materials and its applications in related devices, *Chem. Soc. Rev.*, 47 (2018)1822-1873.

38. A.C. Ferrari, D.M. Basko, Raman spectroscopy as a versatile tool for studying the properties of graphene, *Nat. Nanotechnol.* 8 (2013) 235–246.

39. S.Ghosh, T. Mathews, B. Gupta, A. Das, N.G. Krishna, M. Kamruddin, Supercapacitive vertical graphene nanosheets in aqueous electrolytes, *Nano Struct. Nano Obj.*10 (2017) 42–50.

40. A.C.Ferrari, J.C. Meyer, V. Scardaci, C. Casiraghi, M. Lazzeri, F. Mauri, S. Piscanec, D. Jiang, K.S. Novoselov, S. Roth, A.K. Geim, Raman spectrum of graphene and graphene layers, *Phys, Rev. Lett.* 97 (2006) 187401 (1- 4).

41. M.S.Dresselhaus, A. Jorio, M. Hofmann, D. Dresselhaus, R. Saito, Perspectives on carbon nanotubes and graphene Raman spectroscopy, *Nano Lett.* 10 (2010) 751–758.

42. M. Liu, J. Qian, Y. Zhao, D. Zhu, L. Gan, L. Chen, Core–shell ultramicroporous @microporous carbon nanospheres as advanced supercapacitor electrodes, *J. Mater. Chem. A* 3 (2015)11517-11526.

43. P. Simon, Y. Gogotsi, Capacitive energy storage in nanostructured carbon–electrolyte systems, *Acc. Chem. Res.* 46 (2012) 1094-1103.

44. Y. Mun, C. Jo, T. Hyeon, J. Lee, K.S. Ha, K.W. Jun, S.H. Lee, S.W. Hong, H.I. Lee, S.Yoon, Simple synthesis of hierarchically structured partially graphitized carbon by emulsion/block-copolymer co-template method for high power supercapacitors, *Carbon* 64 (2013) 391-402.

45. H.D.Yoo, J.H. Jang, J.H. Ryu, Y. Park, S.M. Oh, Impedance analysis of porous carbon electrodes to predict rate capability of electric double-layer capacitors, *J. Power Sources* 267 (2014) 411-420.

46. D.P.Dubal, S.H. Lee, J.G. Kim, W.B. Kim, C.D. Lokhande, Porous polypyrrole clusters prepared by electropolymerization for a high performance supercapacitor, *J. Mater. Chem.* 22 (2012) 3044-3052.

47. K.J.Samdani, S.H. Kim, J.H. Park, S.H. Hong, K.T. Lee, Morphology-controlled synthesis of  $\text{Co}_3\text{O}_4$  composites with bio-inspired carbons as high-performance supercapacitor electrode materials. *J. Ind. and Eng. Chem.* 74 (2019) 96–102.

48. R.W.Fu, Z.H. Li, Y.R. Liang, F. Li, F. Xu, D.C. Wu, Hierarchical porous carbons: design, preparation, and performance in energy storage, *New Carbon Mater.*, 26(3) (2011) 171–179.

49. T. Liu, F. Zhang, Y. Song, Y. Li, Revitalizing carbon supercapacitor electrodes with hierarchical porous structures, *J. Mater. Chem. A* 5 (2017) 17705–17733.

50. S.H.Song, J.S. Park, J.H. Song, C.S. Lee, J. Bae, Multi-dimensional nanocarbons hybridized with silicon oxides and their application for electrochemical capacitors, *Carbon Lett.* 29 (2019) 123–131.

51. B. Zheng, T. W. Chen, F. N. Xiao, W. J. Bao, X. H. Xia, KOH-activated nitrogen-doped graphene by means of thermal annealing for supercapacitor, *J. Solid State Electrochem.*, 17 (2013) 1809–1814.

52. M. Chen, X. Zheng, Y. Ma, X. Dong, Oxygen-rich porous carbon sheets: facile one-step synthesis and enhanced electrochemical performance, *Diam. Relat. Mater.* 85 (2018) 89–97.

53. M. Seredych, M. Koscinski, M. Sliwinska-Bartkowiak, T.J. Bandosz, Charge storage accessibility factor as a parameter determining the capacitive performance of nanoporous carbon-based supercapacitors, *ACS Sustain. Chem. Eng.*, 1 (2013) 1024–1032.

54. M. Sethi, H. Bantawal, U. S. Shenoy, D. K. Bhat, Eco-friendly synthesis of porous graphene and its utilization as high performance supercapacitor electrode material, *J. Alloy. Compd.* 799 (2019) 256–266.

55. L. Wang, H. Tan, J. Chen, H. Zhang, Z. Li, H. Qiu, Porous graphene synthesized by partial combustion for high-performance supercapacitors, *Mater. Lett.* 252 (2019) 345–348.

56. Y.S.Yun , S.Y. Cho , J. Shim , B. H. Kim , S.J. Chang , S. J. Baek , Y. S. Huh , Y. Tak, Y. W. Park , S. Park , H.J. Jin, Microporous carbon nanoplates from regenerated silk proteins for supercapacitors, *Adv. Mater.*, 2013, 25 (2013) 1993–1998.

57. S.Yun, S.O. Kang, S. Park, H.S. Park,  $\text{CO}_2$ -activated, hierarchical trimodal porous graphene frameworks for ultrahigh and ultrafast capacitive behaviour, *Nanoscale*, 6 (2014) 5296–5302.

## CHAPTER-6

---

### Graphene-coupled nitrogen-doped carbon-based hybrid for supercapbattery

---

The technical content described in chapter-6 is based on the work published in Journal of Alloys and Compounds 872 (2021) 159660.

#### 6.1. Introduction

The world's energy production is usually reliant on fossil fuel-derived sources for centuries. Almost all the automobile vehicles are widely exploiting petroleum-derived fuels causing massive air pollution and global warming. The long-term exposure to the alarming environmental conditions could hamper the biodiversity and flora and fauna [1,2]. Coincidentally, the research community inclining to explore renewable sources to alleviate the environmental-related vital issues to mitigate global warming. However, the renewable sources' intermittent characteristics enforces for energy storage to bridge the discontinuity between demand and supply of energy. Presently, prodigious attention being paid to develop advanced energy storage devices (AESD) for electric vehicles (EV) in the field of automobiles for transportation and other applications [3].

Currently, in the regime of AESD, the outstanding scientific attempts have been devoted to exploring Li-ion battery system (LIBS) and electrochemical double-layer based capacitor (EDC) for energy storage. Furthermore, the precarious limitations in the area of specific energy density, and the specific power density of EDC and LIBS, respectively, laid a constructive pathway to integrate them to develop AESD [4,5]. Although, the LIBS system deliver remarkable energy density (200 Wh/kg), lack in offering sufficient power density (<1 kW/ kg) (6-8). On the other hand, EDC offers extraordinary power density (5–10 kW/kg), and it flops to meet the desired specific energy density (<10 Wh/kg) [9,10]. Therefore, it is of strategic interest to hybridize LIBS and EDC to overcome individuals' limitations to achieve superior energy and power density to suit for EV. Interestingly, a concept of integrating LIBS and EDC as hybridized technology called hybrid Li-ion supercapbattery (HLS) gained vital interest to maintain the continuity between the energy delivered by LIBS and EDC. In light of the limitations of EDC and LIBS, substantial efforts have been dedicated in combining the best potential capabilities of LIBS (high energy density), and EDC (exceptional power density) to develop an efficient AESD.

Usually, HLS consists of an insertion-type anode (high capacity battery-type) combined with the hierarchically porous cathode (high rate capacitive-type). Although, carbonaceous materials (carbon nanotubes, graphene, activated carbon, carbon onion, activated carbon, hard

carbon, soft carbon, defected carbon) are widely explored to apply into LIB and EDC, most importantly, the porous carbon is widely exploited as the cathode in HLS (4,5). Owing to the insufficient specific capacity (<50 mAh/g) of commercially available activated carbon, researchers have paid vigorous attention to design and exploit alternative carbonaceous materials as the cathode [4,11,12]. In this scenario, the development of novel carbonaceous porous carbon with the hierarchical-structured network, heteroatom doping, good conductivity and appropriate pore size distribution is desirable. Hence, creating a porous structure with suitable porosity and pore size distribution, which suits as cathode for HLS, is on top-priority to meet the rapidly growing market, other than conventional activated carbonaceous materials. To generate such physicochemical properties, much scientific efforts are attempted to tailor the structure, doping and rational design of carbonaceous materials. Interestingly, a process of making carbon material with a porous network with heteroatom-doped redox-material gained wide publicity to use them as cathode for HLS [4, 13-15].

Although, graphene possesses high surface area, restacking of the sheets inhibit its practical application as electrode material [16]. In this connection, an attempt was made to develop a nitrogen-rich thin layer of amorphous carbon coated on graphene to avoid restacking of graphene sheets, and to induce redox-coupled electrochemical characteristics. The higher electronegativity of nitrogen attracts the cation ( $\text{Li}^+$ ) of Li-ion and increases the electrochemical properties via bulk storage, surface storage and vacancy storage [17].

This work demonstrates an exciting process of preparing a hierarchically porous nanoscaled-graphene (NG) hybridized nitrogen-enriched amorphous carbon network (PNCG) rich with nitrogen and suitable porosity to deploy them as appropriate cathode material for HLS. PNCG exhibited an exceptional capacity (discharge) of 156.9 mAh/g at a current density (discharge) of 1.0 A/g. The surface-driven Li-ion diffusion dynamics and key factors responsible for the outstanding performance of PNCG are discussed.

## 6.2. Materials and Methods

### 6.2.1 Preparation of PNCG

In this work, various chemicals, solvents and reagents (analytical grade) were used in their original form without any further modification. N, N-dimethyl pyrrolidone (NMP), polyvinylidene fluoride (PVDF) (binder), N, N-Dimethyl formamide (NDMF) and ammonium persulfate (APS) are purchased from Sigma-Aldrich. Ultrapure deionized water (high grade) with

high electrical resistivity around  $13.8 \text{ M}\Omega\text{.cm}$  produced by Milli-Q system (Integral-5 model) was used as solvent to prepare co-solvent and washing purpose.

The nanoscaled-graphene (NG) with minimal layers ( $\leq 5$  layers) was prepared by fragmentation of microwave-assisted expanded graphite (MAEG) in a co-solvent mixture with minor modification to the procedure described elsewhere [18]. In brief, 10 grams of MAEG were homogeneously distributed in a co-solvent with NDMF: water (8:2 v/v) to match nanoparticles' surface energy to the solvent. The MAEG contained solution was taken in a kitchen mixer bowl (Preeti, Diamond, 750 W), and agitated for 4 h with on/off mode to avoid overheating of the solvent and the mixer unit. The complex fluid dynamics created in a blade-assisted mixer bowl ensure the easy fragmentation and delamination of sheets. The as-produced NG was filtered out, and thoroughly washed with copious amount of water to take out the solvent's traces and dried for overnight. NG with 1.5 wt. % to aniline was added to the 1M HCl containing water solution and oxidized with APS's help to form a thin layer of polyaniline on NG (PCNG hybrid) via in-situ redox polymerization process. The PCNG converted into N-doped carbon coated on NG by annealing at  $600 \text{ }^{\circ}\text{C}$  for 4 h in a nitrogen atmosphere. As annealed PCNG hybrid was mixed with KOH powder (1:3 w/w) and pyrogenic agent-assisted activation was executed at  $400 \text{ }^{\circ}\text{C}$  (for 2 h) and  $750 \text{ }^{\circ}\text{C}$  (for 1 h), sequentially. The temperature of the electric furnace was raised with a ramp rate of  $3.0 \text{ }^{\circ}\text{C}/\text{min}$  during heating. For simplicity, the surface modified PCNG hybrid through activation was labelled as hierarchically porous nitrogen-enriched carbon with nanoscaled graphene network (PNCG). PNCG is collected for further characterization and electrochemical performance.

### 6.2.2 Characterization-related instruments

Field emission scanning electron microscope (SEM, Carl-Zeiss, Gemini-500 model, Germany), Nitrogen adsorption/desorption (Micromeritics, ASAP 2020 model, USA), X-ray photoelectron spectroscopy (XPS, Omicron model, USA) to examine morphology, BET surface area and N-functional moieties in PNCG, respectively. For surface area measurements, the PNCG powder was degassed at  $250 \text{ }^{\circ}\text{C}$ . The integrated simultaneous thermal analyser (STA, 449 Jupiter model, Netzsch, Germany) consisting of thermo-gravimetric technique (TG), differential thermo-gravimetric technique (DTG) and differential thermal-analysis technique (DTA) was used to study thermal stability of PNCG. STA was executed in a constant airflow (75 ml/min) with the help of lid-containing ceramic pan at ramp rate of  $10 \text{ }^{\circ}\text{C}/\text{min}$ . The data was collected for the temperature range of  $30\text{--}800 \text{ }^{\circ}\text{C}$ . Transmission electron microscope (TEM, Model FEI Technai G<sup>2</sup> S-Twin, USA), Raman spectroscopy (Lab Ram HR800 Raman spectrometer; 514.5

nm green line of Ar<sup>+</sup> ion laser was used as the excitation source), and X-ray diffraction (XRD, Bruker's AXS Model D8 Advance System) was used for microstructure, crystallinity and phase composition of the material, respectively.

### 6.2.3 Electrode preparation and fabrication of electrochemical cell

The Li-storage characteristics of PNCG powder was evaluated by 2-electrode coin-cell with sandwich-structured configuration. The electroactive working electrode was fabricated by adding PNCG, acetylene black, PVDF (8:1:1 wt. %) to NMP and then, uniformly coated on aluminium foil. The organic electrolyte consisting of 1M LiPF<sub>6</sub> dissolved in dimethyl carbonate (DEC), and ethylene carbonate (EC) with ratio of 1:1 (v/v) was used for electrochemistry. The 2032-type coin cells (sandwich-type) were tightly fastened in an argon (inert) containing glove box. By considering Li-metal foil (as counter and reference electrode), and glass-microfiber thin filters (M/s Whatman make) as the separator, the sandwich-structured cell was designed. Cyclic voltammetry (CV) was examined in the potential range of 2.0-4.5 V (vs Li/Li<sup>+</sup>) with variable scan rate in a domain of 5-200 mV/s. Based on input (potential) from the CV measurements, the galvanostatic cycling for charge/discharge measurements (GCD) were evaluated in the potential (voltage) from 2.0 to 4.5 V. Electrochemical impedance spectroscopy for Nyquist plot (EIS) was measured in a frequency range of 10 MHz to 0.01Hz with voltage amplitude of 10 mV. Electrochemical characteristics of PNCG was measured using Biologic make workstation (BioLogic Make, BCS-805 Model, France).

## 6.3. Results and discussion

### 6.3.1 Morphology and physicochemical characterization

**Fig.6.1** illustrates the morphology of NG, PNCG without NG and PNCG. **Fig.6.1a** shows micron-sized NG are having corrugated edges. PNCG without NG and PNCG consist of surface-etched morphology rich in pores as illustrated in **Fig.6.1b** and **Fig.6.1c,d**, respectively. KOH-activation process converted the amorphous carbon into rough and uneven surfaces owing to the creation of porosity-rich surfaces. At a few spots, the presence of NG in PNCG was noticed as depicted in **Fig.6.1c and 1d** (yellow circles). Additionally, the presence of NG in PNCG was confirmed by performing TEM imaging as showed in **Fig.6.2**. It contains NG in PNCG (for spot 1 in 2a) and corresponding selected area diffraction pattern (SAED) was depicted in **Fig.6.2c**. It contains rings consist of bright spots in a regular fashion indicating presence of crystalline NG. Also, presence of NG was noticed as indicated in Fig.6.2b where it consist of distinguishable layers. Similarly, the amorphous carbon (for spot 2 in 2a) in PNCG presented diffused rings infer the poor crystallinity as illustrated in **Fig.6.2d**. Actually, NG consist of minimal layers with  $\leq 5$

layers and it was confirmed by TEM imaging as depicted in **Fig. 6.2e** and **6.2f**. **Fig.6.3** presents the thermal stability of PNCG. DTA and DTG graphs consist of multiple peaks located at 87 °C (Peak-I), 275 °C (Peak-II) and 512 °C (Peak-II) corresponding to moisture removal, amorphous carbon oxidation and degradation of backbone units of PNCG and NG. TG presented weight loss in three regimes with weight loss of 5.72 % (up to Peak-I), 23.28 % (up to Peak-II) and 64.91 % (up to Peak-III).

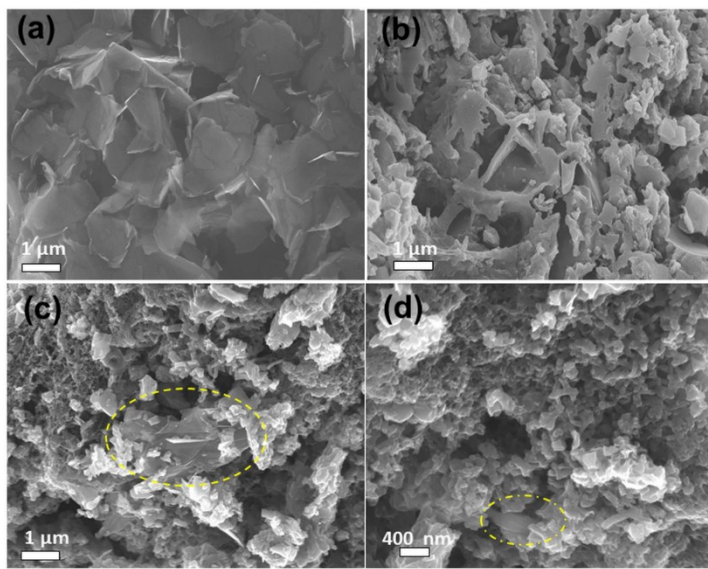


**Fig.6.1** Morphology of (a) NG, (b) PNCG without NG, and PNCG at (c) low magnification, and (d) high magnification.

The surface area and porosity are essential parameters that affect porous materials' utility for electrochemical energy storage in supercapacitors. For this reason, presence of suitable pore size with appropriate pore-size distribution in PNCG with controllable porosity for ion ( $\text{Li}^+$  and  $\text{PF}_6^-$ ) diffusion is desirable. **Fig.6.4** depicts the nitrogen adsorption-desorption hysteresis (as inset) and pore-size distribution. It demonstrates that PNCG exhibit typical type- II isotherm with large H3-type hysteresis (flat adsorption-desorption) loops, indicating slit-type channels owing to presence of a plate-like structured powder. Interestingly, the hysteresis loop (closed) ranging from 0.5 to 0.98 (ratio  $P/P_0$ ) is an indication for the presence of mesopores. PNCG presented exceptionally good porosity with surface area of  $2430 \text{ m}^2/\text{g}$ . It is quite distinguishable with excellent porosity. It exhibited pores in the range of 1.73-100 nm with pore size dominates at 2.7 nm, as indicated in **Fig.6.4**. The resistance-free ion penetration with fast ion-diffusion could be achieved with interconnected hierarchical structures and mesopores present in PNCG.

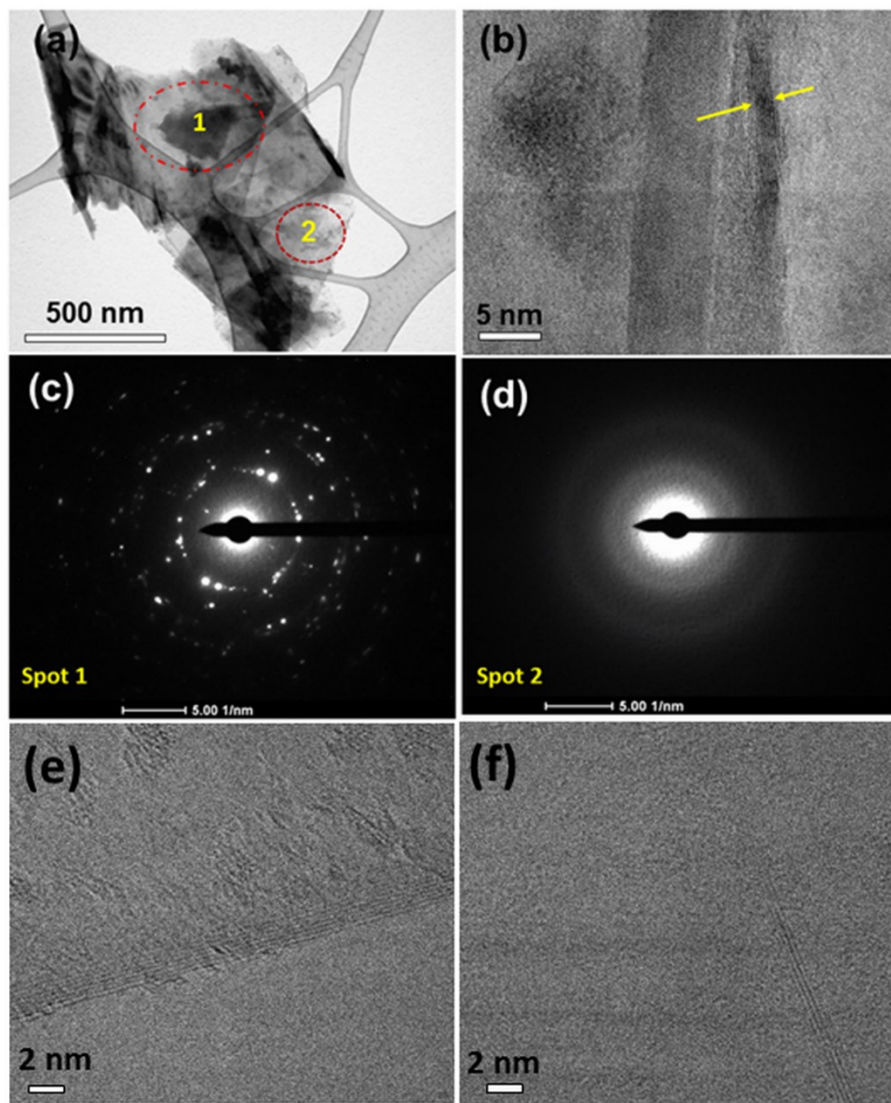


**Fig.6.2** TEM micrographs of PNCG at (a) low magnification, (b) high magnification and SAED pattern of (c) spot 1 and (d) spot 2 present in 2a along with TEM images of NG with minimal layers (e and f).

The functional moieties and elemental composition of PNCG were determined using XPS analysis based on binding energy as showed in **Fig.6.5**. **Fig.6.5a** shows the wide scan of XPS depicting the presence of C, N and O corresponding to the peaks at 284.5, 400.5 and 531.5 eV with amount of 89.42, 4.32 and 6.26 at.%, respectively. Based on the area under the curve ( $N_A/(C_A+N_A+O_A)$ ) in XPS wide scan, PNCG exhibited 4.32 at.% of nitrogen. To further investigate and identify the type of functional N-moieties present in PNCG, N1s peak was de-convoluted into three peaks as illustrated in **Fig.6.5b**. The intense peak at 397.68, 399.40, and 400.92 eV for pyridine-type nitrogen (N6), pyrrolic-type nitrogen (N5), and quaternary-type nitrogen (NQ), respectively. They exist in a quantity of 54.41, 20.09 and 25.50 % area for NQ, N5 and N6,

respectively. The de-convoluted C1s narrow scan consist of four major peaks at 284.18, 285.06, 287.31 and 292.30 eV corresponding to C1 ( $sp^2$  C, 45.57 % area), C2 ( $sp^3$  C, 36.93 % area), C3 (N- $sp^2$  C, 15.01 % area) and C4 (N- $sp^3$  C, 2.49 % area), respectively is depicted in **Fig.6.5c**. In Fig.6.5d, O1s narrow scan showed two major peaks at 530.64 and 532.77 eV corresponding to O1 (C=O/O-C=O, 42.23 % area) and O2 (C-O/C-O-C, 57.77 % area), respectively. Presence of NQ, N5, and N6 along with  $sp^3$ -hybridized carbon creates large amount of defects. Especially, existence of  $sp^3$ -C indicates the presence of defect sites in PNCG. The presence of N-moieties in PNCG are rich in defected-sites with high electronegativity are the source of  $Li^+$  adsorption.

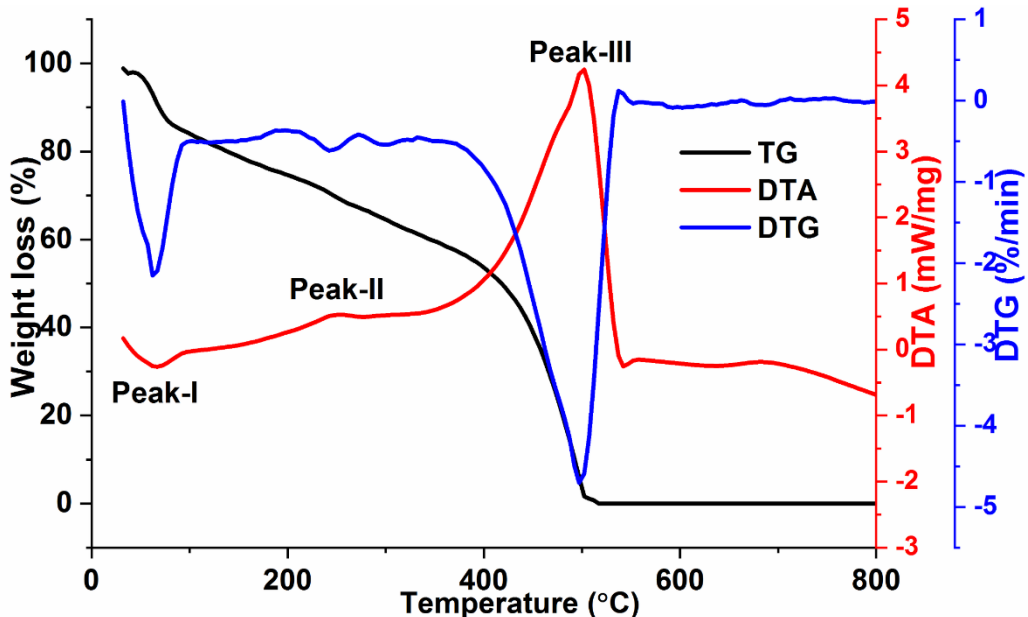


**Fig.6.3** Thermal stability (TG, DTA and DTG) of PNCG.

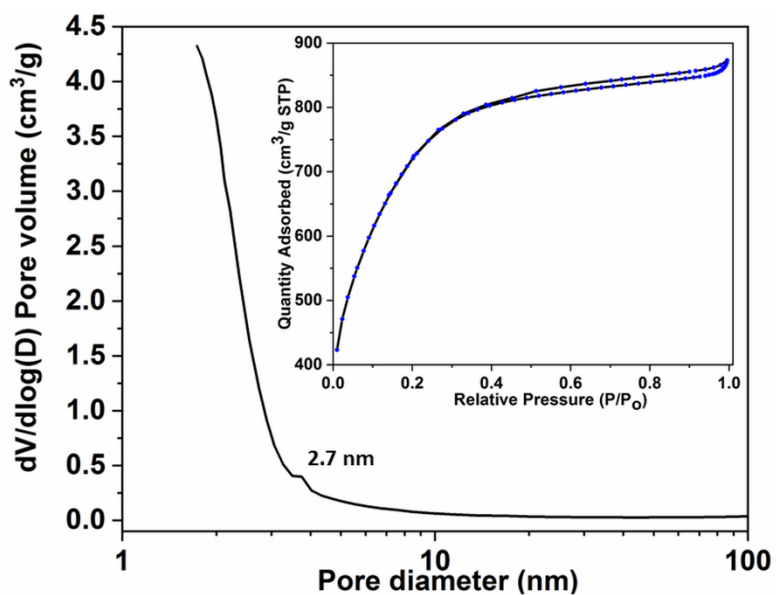


**Fig.6.4** Nitrogen adsorption/desorption with pore-size distribution of PNCG .

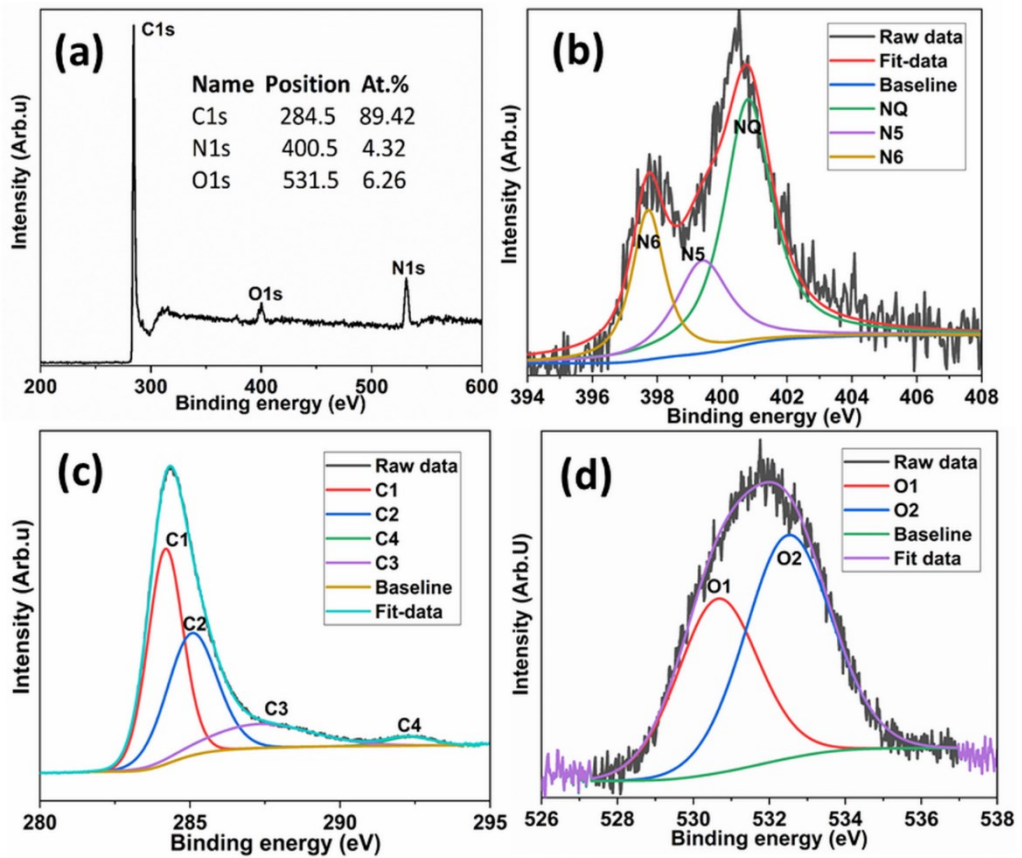


**Fig. 6.5** Elemental functionality present in PNCG: (a) XPS wide scan, (b) N1s narrow scan, (c) C1s narrow scan, and (d) O1s narrow scan.

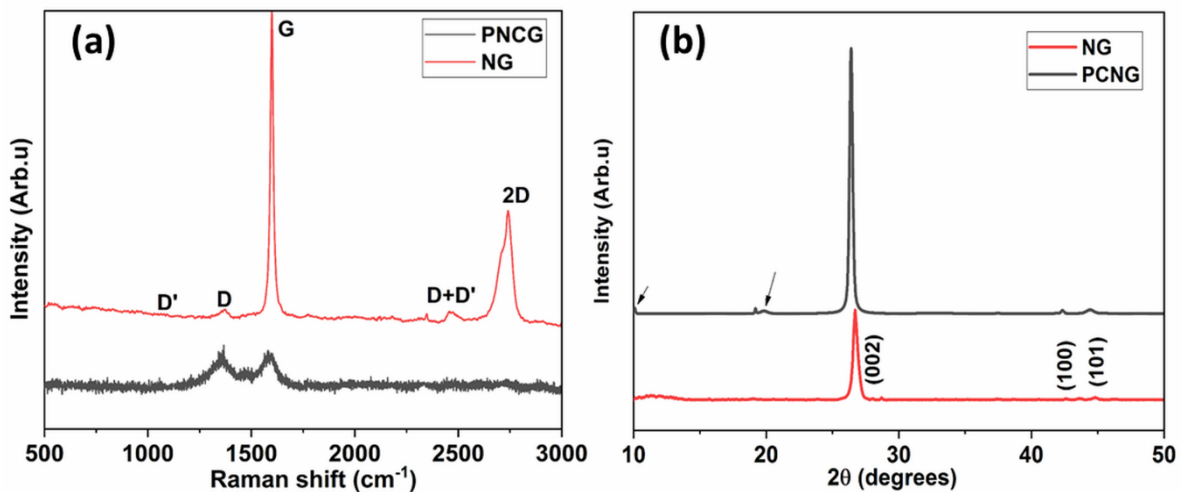


**Fig.6.6** (a) Raman spectra, and (b) XRD pattern of NG and PNCG.

The degree of structural defects in carbon-based materials can be studied by Raman spectroscopy (Fig.6.6a), which consist of four major peaks at 13.63.7, 1598.3, 2459.5, and

2743.1 cm<sup>-1</sup> for D-band, G-band, D+D'-band and 2D-band, respectively (19,20). The intensity ratio of the D- to G-band ( $I_D/I_G$ ) provides a qualitative evidence for the degree of defects. A higher ratio of  $I_D/I_G$  demonstrates presence of quite more defects and lower degree of graphitization. NG and PCNG presented  $I_D/I_G$  ratio of 0.21 and 0.98, respectively. Upon activation with KOH, the surface etch-away process (for PNCG) modified the surface with pores and defects. Along with this, N-content (4.32 at.% from XPS) incorporated in PNCG is also responsible for increase in intensity of  $I_D/I_G$ . Fig.6b presents the XRD pattern for NG and PNCG. For NG, it consist of three major peaks at 26.7°, 42.34° and 44.48° corresponding to (002), (100) and (101), respectively. Whereas, PNCG having five peaks at 10.08°, 19.21°, 26.4°, 42.35°, and 44.48°. The peak at 10.08°, and 19.21° (indicated with arrows pointing them) are corresponding to presence of abundant pore structure, and N-doped carbon from polyaniline-derivatives, respectively (21). The slight change in position of (002) for 0.03° is accounted for defected carbon with more d-spacing in comparison to NG confirms the formation of PNCG with defected carbon.

### 6.3.2 Li-storage properties of PNCG

Owing to N-enriched carbon and hierarchical porosity, PNCG was employed as a cathode for HLS. The cathode's capacitive characteristics in a sandwich-structured module with half-cell configuration were assessed using CV and GCD techniques measured from 2.0 to 4.5 V. Fig.6.7a illustrates CV curves of PNCG performed with variable scan rates (from 5 to 200 mV). PNCG cathode exhibited quasi-rectangular shaped CV curves, indicating typical capacitive-type behaviour. Small humps in a CV curve performed at 5mV scan rates (clearly) infers the presence of pseudocapacitive contribution, could be ascribed to the presence of N-functionality. The peaks (humps) in CV curves are gradually disappeared with an increase in scan rate. The deviation from the ideal rectangular (for EDC) shaped CV curves could be owing to the existence of O, and N-related functionalities in PNCG. The nitrogen-incorporated in carbon hexagonal structure possesses a high degree of electronegativity as compared to the carbon atom. Therefore, the positively charged Li<sup>+</sup> ions are swiftly attracted towards the defective-sites created due to N-doping. PNCG exhibited an identical shape of the CV profile consistently, even at greater scan rates (200 mV/s) demonstrating an outstanding rate capability. The quasirectangular-type CV profiles suggest that PNCG is rich in capacitive behaviour with very weak polarization and excellent reversibility. Considering the criteria as mentioned above, the GCD test was executed to evaluate the Li-ion storage/diffusion kinetics in a process of charging as well as discharging.

The capacitive behaviour of PNCG was evaluated beyond the open-circuit potential (vs Li) is critically attributed to adsorption/desorption kinetics of anion contained in an organic electrolyte and Helmholtz double-layer (HDL) created at vicinity of electrolyte-electrode interface. **Fig.6.7b** illustrates GCD profile of PNCG performed at a discharge current-density in the regime of 0.2-2.0 A/g. The non-linear profiles during charging and discharging are an excellent agreement to the EDC characteristics with redox reactions. The GCD curves are nearly-straight in nature with linear dependency, and remained unchanged (shape) with an increase in current density. During discharging, IR drop was detected at all the discharging current density could be attributed to the traces of over-oxidized defected-carbon (with less electrical conductivity) coated over NG. In a process of ion storage (charging/discharging), PNCG cathode creates HDL at the interface of electrode-electrolyte in a charging process, and then, the stated mechanism is reversed in subsequent discharge cycle to create ion swapping. PNCG displayed the specific capacity of 188.8, 172.9, 156.9 and 135.4 mAh/g at the discharge current-density of 0.2, 0.5, 1.0 and 2.0 A/g, respectively as depicted in Fig.7c. Moreover, PNCG without NG (**Fig.6.7c**) displayed a specific capacity of 99.0, 83.9, 66.9 and 43.7 mAh/g at 0.2, 0.5, 1.0 and 2.0 A/g, respectively. Furthermore, it presented a discharge capacity of 147.9 mAh/g after 500 cycles at a current density of 1.0 A/g with a retention of 94.2 % capacity demonstrating exceptional cycle stability as depicted in **Fig.6.7d**.

Further, the analysis of a cathode's specific capacity is crucial to apply in HLS as it is deployed in an asymmetric-structured configuration; the two electrodes undergo dissimilar charge-storage phenomena. Furthermore, the supplied voltage is disseminated between anode and cathode unequally (proportionately) depending on individual electrodes' mass and capacity. PNCG exhibited excellent capacity (135.4 mAh/g) even at high current density of 2.0 A/g is an excellent suggestion to apply them in practical application.

The electrochemical behaviour and adsorption/desorption-kinetics of PNCG were analyzed through the EIS technique with frequency from 10 mHz to 10 kHz at the discharge current density of 0.1 A/g. Nyquist impedance plot (before and after 500 cycles) in 2.0-4.5 V is clearly illustrated in **Fig.6.7e**. Typically, it comprises of a semicircle in high frequency regime, Warburg impedance in mid frequency regime and capacitive characteristics in low frequency regime. Existence of a semicircle in the high frequency regime relates to the charge transfer resistance ( $R_{ct}$ ) at the interfaces of electrode (active material)-electrolyte. It significantly increased (from  $39.3 \Omega$  to  $89.5 \Omega$ ) after 500 cycles could be due to the build-up of impedance. Build-up of impedance is generated because of surface kinetics, structural changes, irreversible

reactions and ageing of material as explained by Jung et. al. (22). Having a close look on Warburg impedance (medium-frequency regime) for PNCG after 500 cycles, it was dominant significantly could be ascribed to (i) surface-diffusion of adsorbed (anion and cation) ions and (ii) ion-diffusion within complex and intricate narrow pores [23].

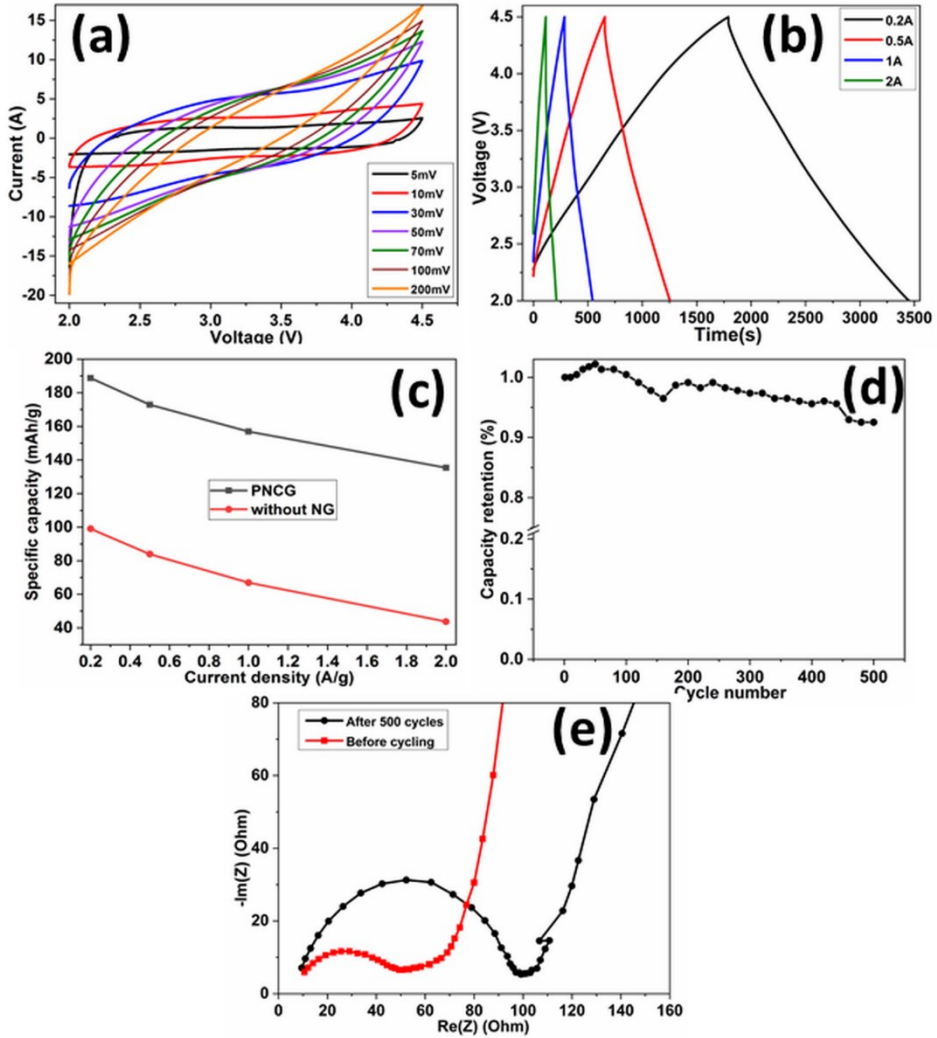


**Fig.6.7** Electrochemical properties of PNCG: (a) CV, (b) CD, (c) capacity vs current density, (d) cyclic stability, and (e) Nyquist plot.

A strategy of measuring voltage hysteresis shed light on the mechanism of the build-up of impedance during cyclic stability and rate capability. To have an eye on rate capability of the PNCG, ‘charge-averaged’ charge /discharge voltage study was performed by adopting a procedure described by Harlow et al. [24]. The ‘charge-averaged’ discharge voltage (CADV,  $V_{\text{dis}}$ ) and ‘charge-averaged’ charge voltage (CACV,  $V_{\text{charg}}$ ) were estimated from the following relations:

$$\text{CADV} = (\int V_{\text{dis}} \times dq_{\text{dis}}) / \int dq_{\text{dis}} \quad (1)$$

$$\text{CACV} = (\int V_{\text{charg}} \times dq_{\text{charg}}) / \int dq_{\text{charg}} \quad (2)$$

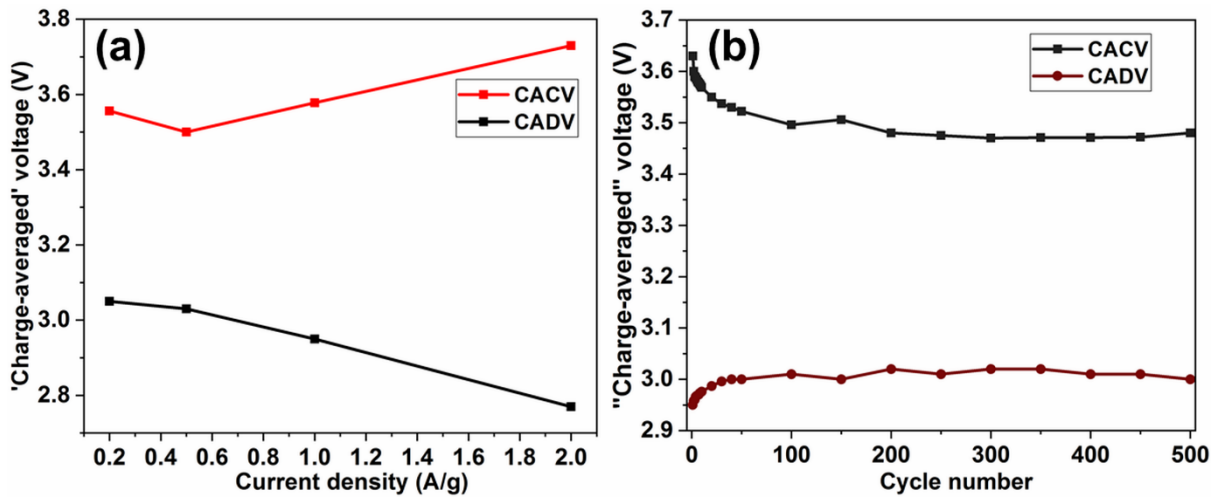


**Fig.6.8** 'Charge-averaged' charge/discharge voltages: (a) for rate capability, and (b) for cyclic stability.

Usually, the minimum (converging narrow) or maximum (wider) voltage hysteresis indicates the build-up of impedance. Now, voltage hysteresis indicates the difference between CACV and CADV at the corresponding current density. **Fig. 6.8a** depicts the effect of discharge current density (rate capability) on the build-up of impedance. Compared to initial voltage hysteresis, the hysteresis at 0.5 A/g reduced marginally and then, it was widened significantly at 2 A/g. At the higher rate, the diffusion of ions will not get sufficient time to diffuse within narrow and intricate pores, leading to widened voltage hysteresis, which indicates the formation of the build-up of impedance. Fig.6.8 b illustrates the variation in hysteresis of CACV and CADV with the cumulative cycles. Up to 100 GCD cycles, the hysteresis was getting narrow in comparison to the initial condition. However, it was maintained constant in the range of 100 to 450 cycles. Later (after 450 cycles), the hysteresis was started widened due to build-up of impedance. Overall, the build-up of impedance arises from initial barrier (interfacial charge transfer) and diffusion within narrow and irregular complex pores. The exceptional Li-storage properties of various kinds of smallscaled-carbon are compared to this work is presented in **Table 6.1**. It confirms that PNCG exhibited remarkable Li-storage characteristics on par with previously reported studies [25-36].

PNCG exhibited the exceptional capacity to be suitable as cathode for HLS. The superior performance of PNCG could be ascribed to the contribution from (a) graphitic graphene nanoplatelets (b) porous structures, and (c) N-doping. The defect-free graphene nanoplatelets could able to enhance electron transport, and such fast electrons movements can reduce the

electrical resistance. The controlled-porosity with suitable pore size distribution could allow electrolyte ion swiftly and reduce charge transfer resistance. The electronegativity of nitrogen in defected amorphous carbon could act as a defect site to attach with the positively charged Li-ion. The vacancies (NQ, N5, N6 and  $sp^3$ -hybridized carbon) created due to the defect sites are the significant contributors to the ion adsorption/desorption. The disordered carbonaceous material coated on NG possesses nanopores, cavities, and other defects, leading to an excess of Li-ion storage compared to the bulk graphite (insertion-type) [17]. Moreover, surface modification can further advance carbonaceous materials' capacitive-type performance since N-doping can drive for reduction/oxidation kinetics, fast electron-donor capability, or/and electrode-wettability with the organic electrolytes. Consequently, it might participate in pseudocapacitance owing to electronic transfer ( $-C=NH+2\bar{e} \leftrightarrow -CH-NH_2$ ) via electron donating capacity of nitrogen (37). In PNCG, the NG, N-doping, and porosity play a critical role in enhancing electrical conductivity, redox-coupled reaction with good wettability, and ion diffusion, respectively.

The presence of two lone pair electrons in nitrogen makes it more electron-rich (electronegativity for N and C is 3.0 and 2.6, respectively) than the carbon atom with high electron density, leading to a stronger interaction with positively charged Li-ion. The remarkable electrochemical properties of PNCG is attributed to the presence of electrically conductive NG and N-doped carbon, which has inferior  $Li^+$  intercalation or adsorption potential than crystalline graphite.

#### 6.4 Conclusions

In summary, a high-performance cathode material for HLS was prepared through a facile strategy by integrating the conductive NG with polymer-derived N-doped carbon to fulfil the urgent requirement for electroactive electrode material applied in EV. PNCG delivered 156.9 mAh/g at the current density of 1.0 A/g, suggesting an exceptionally worthy Li-ion storage capability comparable to the current state-of-the-art LIHS system. Consequently, functional porous carbon with tailored physicochemical properties could provide advent opportunities to explore PNCG for AESD which find application in modern EV system.

**Table 6.1**

Literature comparison showing the specific capacity of various porous carbon materials

Materials	Electrolyte	Current density (A/g)	Window (V)	Capacity (mAh/g)	Ref.
ERGO	1 M LiPF <sub>6</sub>	1.0	2.0-4.5	133	21
NHCN-2	1M LiPF <sub>6</sub>	1.0	2.0-4.5	123	22
NPC	1M LiPF <sub>6</sub>	0.1	2.0-4.5	83	23
URGO	1M LiPF <sub>6</sub>	0.028	2.0-4.0	35	24
HDMPC	1M LiPF <sub>6</sub>	0.1	2.0-4.5	109	25
PRGO	1M LiPF <sub>6</sub>	0.17	1.5-4.5	171	26
CPAC-5	1M LiPF <sub>6</sub>	0.3	2.0-4.5	135	27
a-NGA	1M LiPF <sub>6</sub>	1.5	2.0 -4.0	52	28
Coconut AC	1M LiPF6	0.1	3.0-4.6	63	29
Corncob-NAC	-	0.4	2.0-4.5	129	30
Egg-carbon	1M LiPF6	0.4	2.0-4.5	128	31
CDC	1M LiPF6	0.1	2.0-4.0	101	32
<b>PNCG</b>	<b>1M LiPF<sub>6</sub></b>	<b>1.0</b>	<b>2.0-4.5</b>	<b>156.9</b>	<b>This work</b>

## 6.5 References

1. M. Takahashi, Z. Feng, T.A. Mikhailova, O.V. Kalugina, O.V. Shergina, L.V. Afansieva, R.K.J. Heng, N.M.A Majid, H. Sase, Air pollution monitoring and tree and forest decline in east Asia: a review, *Sci. Total Environ.* 742 (2020) 140258 (20pp).
2. K. Maarten, M.I.V. Margret, B. Pieter, Effects of climate change on biodiversity: a review and identification of key research issues, *Biodivers. Conserv.* 8 (1999) 1383-1397.
3. A. Burke, Ultracapacitor technologies and application in hybrid and electric vehicles, *Int. J. Energy. Res.* 34 (2) (2010) 133-151.
4. X. Wang, L. Liu, Z. Niu, Carbon-based materials for lithium-ion capacitors *Mater. Chem. Front.* 3 (2019) 1265-1279.
5. C. Li, X. Zhang, C. Sun, K. Wang, X. Sun, Y. Ma, Recent progress of graphene-based materials in lithium-ion capacitors, *J. Phys. D: Appl. Phys.* 52 (2019) 143001 (19pp).
6. J. Ding, W. Hu, E. Paek, D. Mitlin, Review of hybrid ion capacitors: from aqueous to lithium to sodium, *Chem. Rev.* 118 (2018) 6457-6498.
7. J.B. Goodenough, K.S. Park, The Li-ion rechargeable battery: a perspective, *J. Am. Chem. Soc.* 135 (2013) 1167-1176.
8. T. Kim, W. Song, D.Y. Son, L.K. Ono, Lithium-ion batteries: outlook on present, future, and hybridized technologies, *J. Mater. Chem. A* 7 (2019) 2942-2964.
9. Y. Wang, Y. Song, Y. Xia, Electrochemical capacitors: mechanism, materials, systems, characterization and applications, *Chem. Soc. Rev.* 45 (2016) 5925-5950.
10. G. Wang, L. Zhang, J. Zhang, A review of electrode materials for electrochemical supercapacitors, *Chem. Soc. Rev.* 41 (2012) 797-828.
11. A. Banerjee, K.K. Upadhyay, D. Puthusseri, V. Aravindan, S. Madhavi, S. Ogale, MOF-derived crumpled-sheet-assembled perforated carbon cuboids as highly effective cathode active materials for ultra-high energy density Li-ion hybrid electrochemical capacitors (Li-HECs), *Nanoscale* 6 (8) (2014) 4387-4394.
12. X. Xu, Y. Cui, J. Shi, W. Liu, S. Chen, X. Wang, H. Wang, Sorghum core-derived carbon sheets as electrodes for a lithium-ion capacitor, *RSC Adv.* 7 (28) (2017) 17178-17183.
13. Y.H. Wang, B. Ding, D. Guo, X.L. Wu, A novel way to synthesize nitrogen and oxygen codoped porous carbon for high performance supercapacitors, *Microporous Mesoporous Mater.* 282 (2019) 114-120.

14. M.D.Stoller, S. Murali, N. Quarles, Y. Zhu, J.R. Potts, X. Zhu, H.W. Ha, R.S. Ruoff, Activated graphene as a cathode material for Li-ion hybrid supercapacitors, *Phys. Chem. Chem. Phys.* 14 (10) (2012) 3388-3391.
15. H.M. Jeong, J.W. Lee, W.H. Shin, Y.J. Choi, H.J. Shin, J.K. Kang, J.W. Choi, Nitrogen-doped graphene for high-performance ultracapacitors and the importance of nitrogen-doped sites at basal planes, *Nano Lett.* 11 (2011) 2472-2477.
16. J. Li, M. Ostling, Prevention of graphene restacking for performance boost of supercapacitors-a review, *Crystals* 3 (2013) 163-190.
17. N.A. Kashedikar, J. Maier, Lithium storage in carbon nanostructures, *Adv. Mater.* 21 (2009) 2664-2680.
18. B. Padya, N. Narasaiah, P.K. Jain, T.N. Rao, A facile co-solvent strategy for preparation of graphene nanoplatelet powder: An industrially viable innovative approach, *Ceram. Int.* 45 (2019) 13409-13413.
19. J.B. Wu, M.L. Lin, X. Cong, H. N. Liu, P. H. Tan, Raman spectroscopy of graphene-based materials and its applications in related devices, *Chem. Soc. Rev.*, 2018, 47 (2018) 1822-1873.
20. R. Beams, L.G. Cancado, L. Novotny, Raman characterization of defects and dopants in graphene, *J. Phys.: Condens. Matter* 27 (2015) 083002 (26pp)
21. X. Huang, X. Yin, X. Yu, J. Tian, W. Wu, Preparation of nitrogen-doped carbon materials based on polyaniline fiber and their oxygen reduction properties, *Colloids Surf. A Physicochem. Eng. Asp.* 539 (2018) 163-170.
22. R. Jung, M. Metzger, F. Maglia, C. Stinner, H.A. Gasteiger, Oxygen release and its effect on the cycling stability of  $\text{LiNixMnyCozO}_2$  (NMC) cathode materials for Li-ion batteries, *J. Electrochem. Soc.* 164 (2017) A1361-A1377.
23. A. Eftekhari, The mechanism of ultrafast supercapacitors, *J Mater. Chem. A* 6 (2018) 2866-2876.
24. J. E. Harlow, S. L. Glazier, J. Li, J. R. Dahn, Use of asymmetric average charge- and average discharge-voltages as an indicator of the onset of unwanted lithium deposition in lithium-ion cells, *J. Electrochem. Soc.* 165 (16) (2018) A3595-A3601.
25. F. Tu, S. Liu, T. Wu, G. Jin, C. Pan, Porous graphene as cathode material for lithium ion capacitor with high electrochemical performance, *Powder Technol.* 253 (2014) 580-583.

26. C. Li, X. Zhang, K. Wang, X. Sun, Y. Ma, High-power and long-life lithium-ion capacitors constructed from N-doped hierarchical carbon nanolayer cathode and mesoporous graphene anode, *Carbon* 140 (2018) 237-248.

27. Y. Cui, W. Liu, Y. Lyu, Y. Zhang, H. Wang, Y. Liu, D. Li, All-carbon lithium capacitor based on salt crystal-tempered, N-doped porous carbon electrodes with superior energy storage, *J. Mater. Chem. A* 6 (2018) 18276-18285.

28. M.H. Ryou, J.K Jin, J. Kim, J.W. Choi, Functionaized graphene for high performance lithium ion capacitor, *Chem. Sus. Chem.* 5 (2012) 2328-2333.

29. J. Niu, R. Shao, M. Liu, J. Liang, Z. Zhang, M. Dou, Y. Huang, F. Wang, Porous carbon electrodes with battery-capacitive storage features for high performance Li-ion capacitor, *Energy Stor. Mater.* 12 (2018) 145-152.

30. D. P. Dubal, G. R. Pedro, All nanocarbon Li-ion capacitor with high energy and high power density, *Mater. Today Energy* 8 (2018) 109-117.

31. Q. Lu, B. Lu, M. Chen, X. Wang, T. Xing, M. Liu, X. Wang, Porous activated carbon derived from Chinese-chive for high energy hybrid lithium-ion capacitor, *J Power Sources* 398 (2018) 128-136.

32. Q. Fan, M. Yang, Q. Meng, B. Cao, Y. Yu, Activated-nitrogen -doped graphene-based aerogel composites as cathode materials for high energy density lithium-ion supercapacitor, *J. Electrochem. Soc.* 163 (8) (2016) A1736-A1742.

33. A. Jain, V. Aravindan, S. Jayaraman, P.S. Kumar, R. Balasubramanian, S. Ramakrishna, S. Madhavi, M.P. Srinivasan, Activated carbons derived from coconut shells as high energy density cathode material for Li-ion capacitors, *Sci. Rep.* 3 (2013) 3002 (6pp).

34. B. Li, F. Dai, Q.F. Xiao, L. Yang, J.M. Shen, C.M. Zhang, et al., Nitrogen-doped activated carbon for a high energy hybrid supercapacitor, *Energy Environ. Sci.* 9 (1) (2016) 102-106.

35. B. Li, F. Dai, Q.F. Xiao, L. Yang, J.M. Shen, C.M. Zhang, et al., Activated carbon from biomass transfer for high-energy density lithium-ion supercapacitors, *Adv. Energy Mater.* 6 (18) (2016) 1600802.

36. H. Li, J. Chen, B. Yang, K. Wang, X. Zhang, T. Zhang, L. Zhang, W. Liu, X. Yan, Constructing surface-driven lithium ion storage structure for high performance hybrid capacitor, *Electrochim. Acta* 299 (2019) 163-172.

37. E. Frackowiak, F. Beguin, Carbon materials for the electrochemical storage of energy in capacitors, *Carbon* 39 (2001) 937-950.

## CHAPTER 7

---

### **Nanocarbon-loaded PCM for thermal energy storage**

---

The technical content described in chapter-7 is based on the work published in Energy Storage 2 (6) (2020) 199 (8pp) and Composites Science and Technology (communicated).

#### **7.1. Introduction**

Since the industrial revolution, fossil fuels are enormously exploited to meet the energy required for the population explosion that resulted in deteriorated environmental and ecological conditions [1-3]. Accounting for these critical challenges, humankind is forced to seek clean and green technology for sustainable development. Consequently, modern transportation is shifting to zero-emission electric vehicles (EV) [4-9].

For EV, an electrochemical system (batteries and supercapacitors) is the primary source for providing high energy density and power density. Owing to exceptionally good energy density and other advantages, Li-ion battery systems (LIBS) are immensely attracted to apply for EV [6-9]. Temperature, charging/discharging rate, ambient climatic conditions, and internal heat generation significantly influence the diffusion-controlled ion-transport in LIBS [10-12]. Seriously, the temperature rises beyond the normal operating range; adversely affects the LIBS performance. However, the LIBS undergoes charging/discharging continuously to meet operational requirements, generates a tremendous amount of heat inside the cells. Overheating may have resulted if the as-generated heat is not dissipated instantaneously at a higher heat transfer rate. Otherwise, it accumulates inside the cell and damages the cell assembly. Notably, many cells are connected (series and parallel) in a LIBS pack to generate huge energy density. The temperature difference between the cells may result in cell rupture and even explosion. Then, overheating, explosion, thermal abuse and safety risk become severe as they lead to abrupt rupture of LIBS cell.

Especially, the temperature has a catastrophic impact on the LIBS's capacity fade. A sustainable environment with isothermal temperature (below 50 °C) must be maintained to achieve high energy density and more life cycles. Otherwise, the burst in temperature could lead to a thermal runaway phenomenon (TRP) by generating mechanical, electrical and thermal abuse [13-23]. Therefore, a material, which can trap as-generated heat and maintain isothermal uniformity, is essential to pause TRP. Subsequently, a novel thermal management system-battery (TMSB) is looked for to avert LIBS from TRP caused by excess heat generation [19-23].

To suppress the abrupt increase in LIBS temperature during operation, the processes of active and passive cooling systems are adopted [22, 23]. Nevertheless, an efficient and suitable thermal management system is instantly essential to overcome the traditional cooling system's disadvantages. Among all, a passive cooling system using phase change materials (PCM) has drawn prodigious interest owing to their advantages over other approaches [13-23]. To intensify the effective means of storing heat, a PCM composition with appropriate phase transition is essential. The PCM will absorb and release heat during melting and cooling, respectively. The existing PCM materials may not handle the heat dissipation solely as they possess significantly less thermal conductivity [24-27]. The low thermal conductivity of fatty acids is a significant concern in applying them for practical applications. In such cases, additives are included in the PCM to ameliorate heat conduction ability. The inclusion of nanofillers to the PCM could be an appropriate option to improve thermal conductivity as they can assist in rapid thermal transport [28-31].

Out of the nanomaterials that the material most widely exploited to ameliorate the PCM's thermal conductivity includes nanoscaled-carbon fillers (graphene, carbon nanotubes, expanded graphite (E-G), carbon onion and carbon nanofibers (CF)), which have drawn attention tremendously owing to their exceptional thermal conductivity, chemically inertness, relatively low density and their suitability with a wide range of PCMs [28]. In a study, RT44HC was used, an organic PCM with exfoliated graphite (Ex-G), to develop a blend that would undergo a phase transition at 44 °C and 200 kJ/kg of latent heat value [32]. The sample variants consisted of Ex-G in 25% and 35% mass fractions. From the experimental results obtained, it is found that mass fraction of filler and the packing density are detrimental in deciding the thermal conductivity. With maintaining equal density, PCM-35% Ex-G showed 30 % greater thermal conductivity than PCM-25 % Ex-G. Also, it was observed that by maintaining the same mass fraction and increasing density, the thermal conductivity also exhibited increasing values. Consequently, thermal conductivity was improved by 20-60 times in comparison to pure PCM having lower density. Tang et al. mixed PA (palmitic acid) and CA (capric acid) to develop a PCM of eutectic nature and used diatomite as a filling substance and E-G to enhance the PCM's heat-conducting capacity [33]. The thermal conductivity of the PCM without E-G is found to be 0.119, and 0.190 W/m. K for solid-form and liquid-form, respectively. The thermal conductivity values of the PCM with varying concentrations of 3 wt. % and 5 wt. % of E-G as filler showed enhancements by 15.1% and 25.2% in solid-form and by 26.3% and 53.7% in the liquid-form. Nomura et al. prepared CF-loaded erythritol-based PCM through dispersion of fillers in molten PCM and

subsequent innovative hot-press to measure the thermal conductivity using the laser flash method [34]. In another study, Tian et al. reported PCM containing E-G and CF in different mass concentrations for thermal conductivity enhancement [35]. The additives (E-G and CF) and ethylene-vinyl acetate (EVA) were uniformly dispersed into the paraffin for conducting filler and supporting material, respectively. The synergistic effect with the addition of E-G and CF resulted in improved thermal conductivity. Graphene-loaded Beeswax-based PCM for building application was also reported, which related well with practical application of the PCM methodology in real-life applications [36]. Experimental studies conducted showed significant improvements in both thermal transport and latent heat of fusion values. PCM's thermal conductivity was enhanced with increase in graphene loading, implying that the improvement of conductivity and mass fraction of graphene have a linear relationship. However, after reaching a threshold limit, the agglomeration of nanoparticles begins, and the linear relationship gets disturbed. The PCM exhibited thermal conductivity of 2.89 W/m. K for 0.3 wt.% loading with an improvement of 1100 %. Consequently, carbon nanoadditives play a vital role in improving thermal transport [32-36].

In the case of LIBS, maintaining temperature distribution below 50 °C is very crucial to suppress TRP. LIBS exhibits maximum cycle life and superior capacity in the temperature regime of 25-40 °C and 15-24 °C, respectively [37]. Therefore, a PCM system with phase transition below 50 °C with suitable latent heat is considered as a promising candidate to apply for temperature controlling in TMSB. To design a PCM system with requisite transition temperature, which matches accurately, could be developed by forming a eutectic system [38-40].

This study focused on developing the suitable composition of eutectic PCM to derive at a phase transition temperature below 50 °C, which is ideal for TMSB. For the figure of merit, the influence of the addition of few-layer graphene platelets (FGP), nitrogen-doped tubular carbon (NTC) and deoxygenated graphene oxide (DGO) on thermal conductivity with underlying mechanism was studied.

## 7.2. Materials and methods

FGP was prepared through a process described elsewhere [41]. In brief, 2-stage EG was prone to complex fluid-dynamics assisted liquid-phase exfoliation in converting it into FGP via exfoliation and fragmentation. The sharp blades in a blender could delaminate EG into fewer layers in FGP. The bubbler-assisted chemical vapour deposition process was adopted to grow

NTC through a procedure described elsewhere with major modification using acetonitrile-ethanol precursor [42]. Briefly, the precursor was allowed to cross the furnace's hot zone (850 °C), where the precursor decomposes, and deposit over the catalyst containing ceramic boat to form NTC. FGP was intensely oxidized using a strong oxidizer to prepare graphene oxide (GO). GO was collected by washing and vacuum-assisted filtration process. Then, GO was converted into DGO via the hydrothermal-assisted partial deoxygenation technique. Later, the GO solution (containing ascorbic acid and ammonia solution) was sealed in a Teflon-lined autoclave system maintained at 210 °C for 5 h. The solid was then filtered with a vacuum-assisted filtration, thoroughly washed with water, and acetone. Finally, it was dried at 70 °C for overnight to form DGO.

To generate a eutectic system, the PCM consisting of myristic (M) and stearic (S) acid (with variable composition, wt. %) was prepared to deduce the eutectic point. The composition was varied from 0 to 100 wt. % (in multiples of 10). After confirmation of the eutectic point (MS system)), the composite material with adding FGP, NTC, and DGO was prepared to evaluate the figure-of-merit (FOM). Nanoadditives (FGP or NTC or DGO) are homogeneously dispersed in a liquid MS PCM system while maintaining the isothermal temperature of 70 °C for 24 h. The as-prepared mixture was transferred to a suitable mould with controlled-cooling to attain the solid phase uniformly. For simplicity, the PCM composites are designated as MS-FGP, MS-NTC and MS-DGO for MS added with FGP, NTC and DGO, respectively. After ascertaining the figure-of-merit, MS with variable FGP loading was developed. For MS-FGP, composites with a variable quantity of FGP was added to evaluate their effect on thermal properties, and it was designated as MS-xFGP where, x denotes the weight fraction of FGP.

Scanning electron microscope (SEM, Gemini-500) was used to determine the surface morphology study of FGP, NTC, DGO, PNCG, PNCT and PNCD. Microstructure and defects in FGP, NTC and DGO were examined using a transmission electron microscope (TEM, FEI Technai G<sup>2</sup> S-Twin). The degree of defects and crystallinity was determined using Raman spectroscopy (Lab Ram HR800 Raman spectrometer) with a 514.5 nm green line. The phase composition and crystallinity of FGO, NCT, and DGO were confirmed using X-ray diffraction (XRD, Bruker's AXS Model D8 Advance System). The thermogravimetric technique (TG), differential thermogravimetric technique (DTG), and differential scanning calorimetry technique (DSC) containing in simultaneous thermal analyser (STA 449 Jupiter, Netzsch) was utilized to study thermal stability, maximum weight loss, and latent heat of fusion, respectively. TG/DTG was performed in the air atmosphere with airflow of 75 sccm (standard cubic centimetre) with

the help of alumina crucible at 10 °C/min. DSC experiments were carried out at 2 °C/min with argon flow rate of 75 sccm to measure phase transition, latent heat and cyclic stability (10 cycles) of MS PCM material. A laser flash system (Netzsch, LFA 427) was deployed to measure MS PCM's thermal conductivity. The average of three readings of thermal conductivity was reported for consistent results.

### 7.3. Results and discussion

#### 7.3.1 Morphological and structural properties of nanocarbon: FGP, NTC and DGO

**Fig.7.1** depicts the surface morphology and microstructure of FGP, NTC and DGO. In **Fig.7.1 (a, b and c)**, it is evident that FGP, NTC and DGO possess micron-sized 2D sheet-like structure, 1D tubular-structure and 2D corrugated sheet-like structure, respectively. FGP consist of few layers of graphene, typically  $\leq 5$  layers with distinguishable edges and quite defect-free, as indicated in **Fig.7.1d**. In **Fig.1e**, NTC exhibited a bamboo culm-like and compartmentalized structure with much-strained graphene layers. Graphene layers in NTC walls are straight, but graphene layers forming a compartment are highly strained and corrugated due to N-doping [43, 44]. DGO has distinguishable layers with many defects, as the hydrothermal deoxygenation process could not reduce it completely (partially), as indicated in Fig.7.1f.

**Fig. 7.2** shows the Raman spectrum, and XRD pattern of FGP, NTC and DGO. In **Fig.7.2a**, the spectrum consists of three major peaks corresponding to D-band, G-band and 2D-band located at 1355, 1590 and 2705  $\text{cm}^{-1}$ , respectively [45]. In the G-band position, a significant shift was noticed for NTC and DGO as compared to FGP, which are accounted for predominant material's strain. FGP, NTC and DGO exhibited the  $I_D/I_G$  ratio of 0.22, 0.95 and 0.96, respectively. It infers that FGP is highly crystalline with fewer defective graphene layers, whereas NTC and DGO are rich in structural defects [45]. The XRD pattern presented major peaks at around 26.7, 44.4 and 54.80 for (002), (100) and (004) planes, respectively, as illustrated in Fig.7.2b. For all the three materials, an intense peak was diagnosed for the (002) plane. For FGP, NTC and DGO, the (002) plane was located at 26.7°, 26.56° and 24.72°, which accounts for d-spacing of 0.33, 0.34 and 0.36, respectively. A very high d-spacing value was noticed for DGO concludes that the oxygen-related moieties have still existed in it.

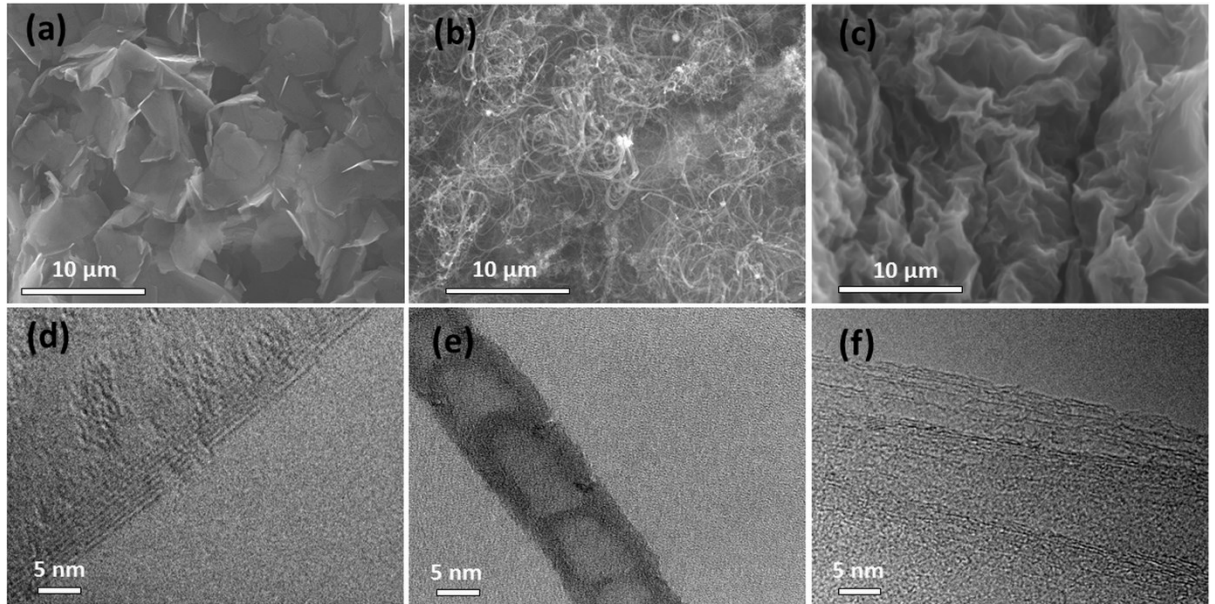


**Fig. 7.1.** SEM images of (a) FGP, (b) NTC, and (c) DGO; TEM images of (d) FGP, (e) NTC and (f) DGO.

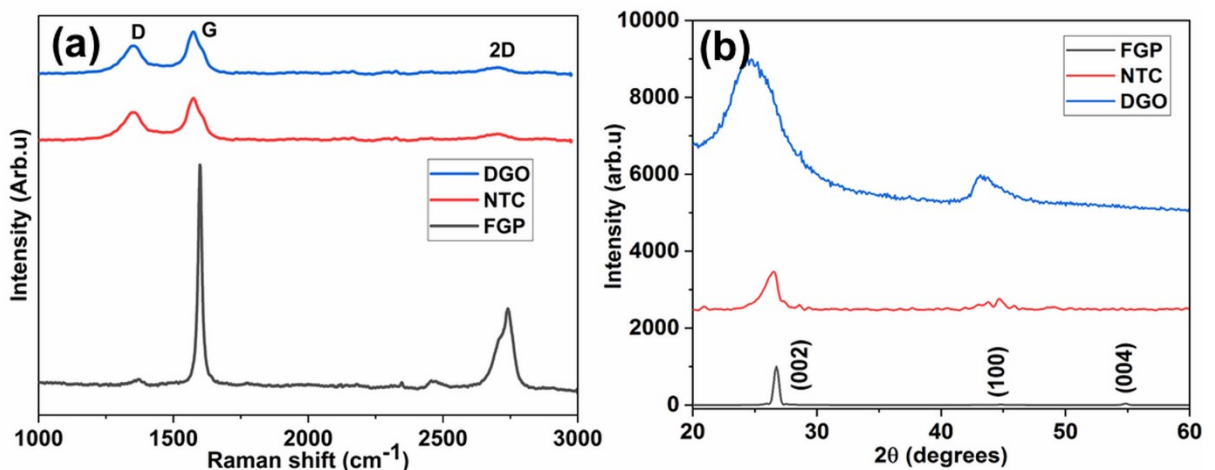


**Fig. 7.2.** (a) Raman spectrum and (b) XRD pattern of FGP, NTC and DGO.

The oxidative thermal stability of FGP, NTC and DGO was illustrated in **Fig.7.3**. In **Fig.7.3a**, the onset temperature for material degradation is stated from 593, 395 and 261 °C for FGP, NTC and DGO, respectively. Furthermore, they possess intense mass loss at 701, 495 and 317 °C for FGP, NTC, and DGO, respectively, as indicated in **Fig.7.3b**. Interestingly, DGO has severe mass loss at 317 and 422 °C, which are accounting for the loss of highly-oxidized carbon and partially-reduced carbon, respectively. The order of oxidative thermal stability is in the order of FGP>NTC>DGO. Considering all the characterization techniques (SEM, TEM, Raman

spectroscopy, XRD and TG/DTG), it is confirmed that they possess structural quality (crystallinity) in the order of FGP>NTC>DGO.

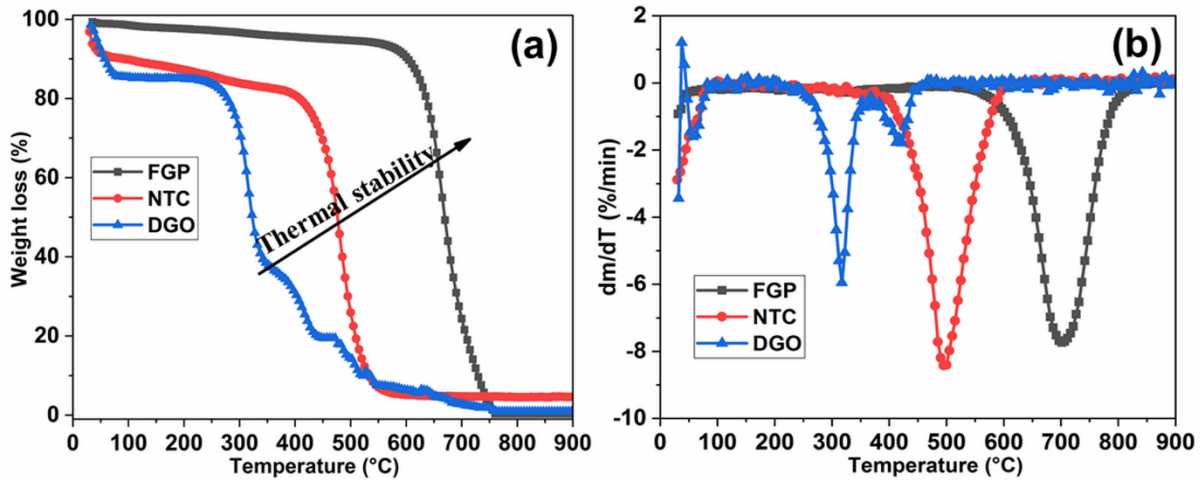


Fig. 7.3. (a) TG and (b) DTG curves of FGP, NTC and DGO.

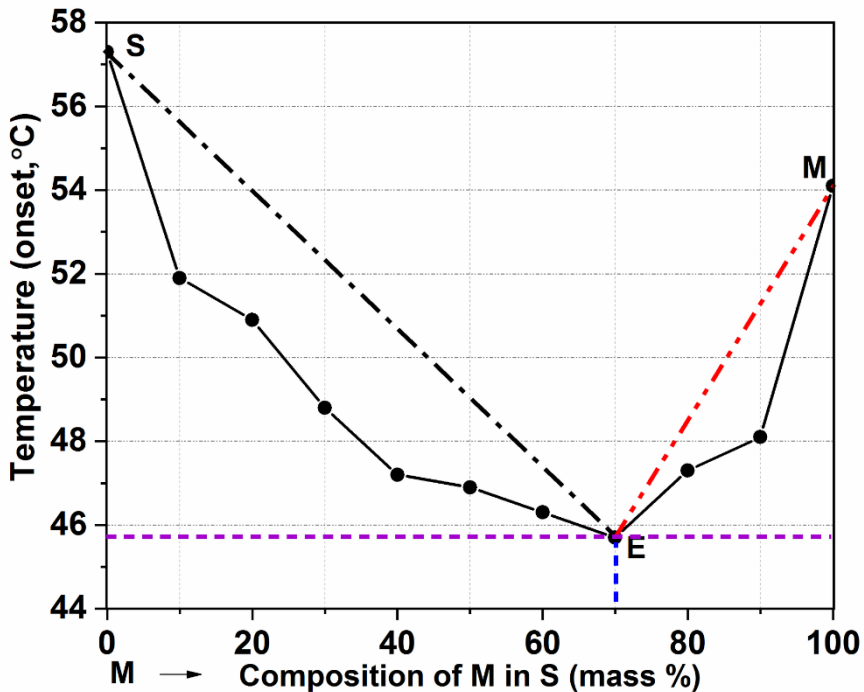
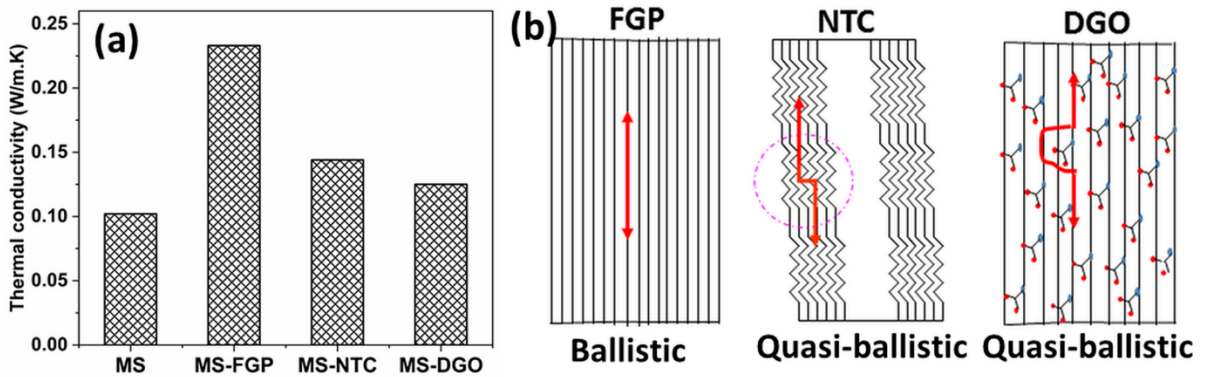


Fig. 7.4. Phase diagram of MS system.

### 7.3.2 Thermal conductivity and thermophysical properties of MS PCM system

To derive the eutectic point, a combination of the M and S system with variable composition was experimentally determined. With varying M in S (with wt.%), the composition based on 1:9, 2:8, 3:7, 4:6, 5:5, 6:4, 7:3, 8:2, 9:1 was formed. Fig.7.4 depicts the phase diagram generated based on the on-set temperature for melting (from DSC). They possesses the onset

transition (starting of melting) of 51.9, 50.9, 48.8, 42.2, 48.9, 46.3, 45.7, 47.3, 48.1 and 54.1°C for 1:9, 2:8, 3:7, 4:6, 5:5, 6:4, 7:3, 8:2, 9:1, respectively. Besides, pure M and S exhibited an onset transition temperature of 54.1 and 57.3°C, respectively. The MS system's melting point gets a lower phase transition temperature than its pure form (M or S). From the phase diagram, the eutectic system was generated at a composition of 7:3=M:S with the eutectic temperature (onset) of 45.78 °C. In **Fig.7.4**, The points M, S and E correspond to the on-set transition temperature of myristic acid, stearic acid and eutectic point, respectively. The achieved eutectic transition temperature is considered most suitable for EV application as it is below 50 °C.



**Fig. 7.5.** (a) thermal conductivity of MS, MS-FGP, MS-NTC and MS-DGO and (b) thermal transport mechanism in FGP, NTC and DGO.

After attaining a eutectic system, three kinds of carbon nanoadditives with varying structural quality are loaded to generate MS-FGP, MS-NTC and MS-DGO with the addition of 1 wt.% of FGP, NTC and DGO, respectively, to observe their influence on thermal transport. MS, MS-FGP, MS-NTC and MS-DGO demonstrated thermal conductivity of 0.102, 0.233, 0.144, and 0.125 W/m.K , respectively, as illustrated in **Fig.7.5a**. MS-FGP, MS-NTC and MS-DGO showed thermal conductivity enhancement of 128, 41 and 22 %, respectively. It is clearly demonstrated that the additives with more defects lead to a significant decrease in thermal transport. The defects in a material could act as a phonon-scattering site via phonon-imperfection scattering mode, phonon-boundary scattering mode, phonon-grain boundary scattering mode, and phonon-impurity scattering mode[46]. The nanoadditives loaded MS system followed the rapid thermal transport in the order of MS-FGP> MS-NTC>MS-DGO as indicated in **Fig.7.5b**. The material with a higher degree of crystallinity supports ballistic transport (FGP), while quasi-ballistic transport is prominent in additives that are more defective. In the case of NTC, the compartmentalized structure possesses N-doped graphene layers, which consists of various defects such as pyridinic-type nitrogen, pyrrolic-type nitrogen, and quaternary-type nitrogen

[43]. These defects act as scattering sites and promote diffuse scattering. Similarly, DGO possesses oxygen-rich moieties, which could serve as a catalysing agent in phonon-scattering. Consequently, the material with a higher degree of crystallinity (FGP>NTC>DGO) drives for faster thermal transport as it is reflected in MS PCM in the order of MS-FGP> MS-NTC>MS-DGO. FGP (1 wt.%) based composite presented faster thermal transport than other additives (NTC or DGO) based composites due to structural degree variation. Importantly, 2-D planar structure with less defects of FGP is the primary reason accounted for the better thermal conductivity. Consequently, the mean free path for the phonon movement is comparatively shorter in minimally defected materials.

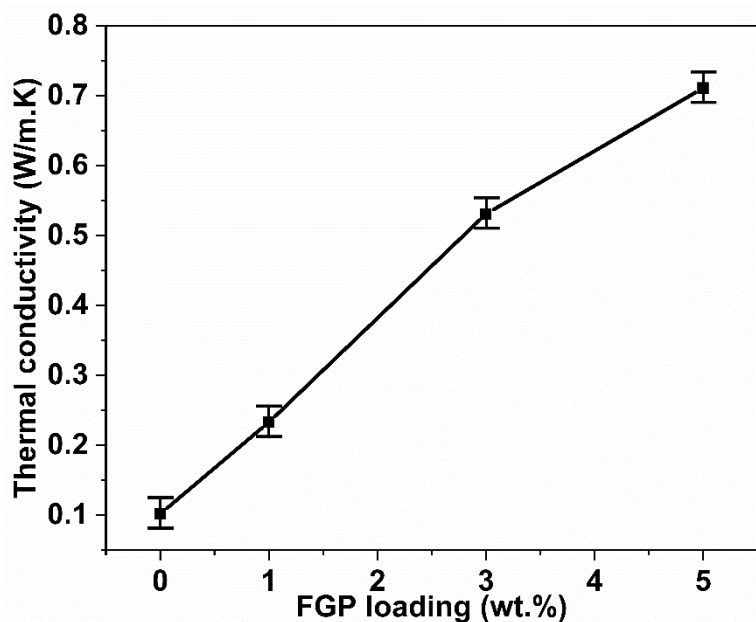


**Fig. 7.6.** Variation in thermal conductivity of MS-xFGP as a function of FGP loading.

To have an eye on variation in thermal transport of MS-FGP system with the quantity of their inclusion, the variable quantity of FGP (1, 3 and 5 wt.%) based system was developed. The composites exhibited thermal conductivity (based on three samples) of 0.102, 0.233, 0.531 and 0.711 W/m.K, for MS, MS-1FGP, MS-3FGP and MS-5FGP, respectively, as illustrated in **Fig.7.6**. They displayed an escalation in thermal conductivity by 128, 420, and 597 % for MS-1FGP, MS-3FGP and MS-5FGP, respectively. A substantial rise in thermal conductivity with increased FGP loading was noticed. Especially, FGP loading of 5 wt. % presented a remarkable rapid increase (597 %) in thermal conductivity. The synergistic effect of crystalline FGP in MS leads to a substantial augmentation in thermal conductivity. MS-5FGP presented a pretty remarkable enhancement in thermal conductivity on par with previous reports [28]. As per previous literature reports, the notable thermal conductivity increase was noticed with various

nanoscaled-carbon additives in comparison with our work such as E-G, CNT, CNF, x-GNP, and NPC, as delineated in **Table 7.1** [47-57]. Interestingly, MS-FGP exhibited remarkably improved thermal conductivity (597 %) on par with the previous reports with appropriate phase transition, which exactly suitable for EV application.

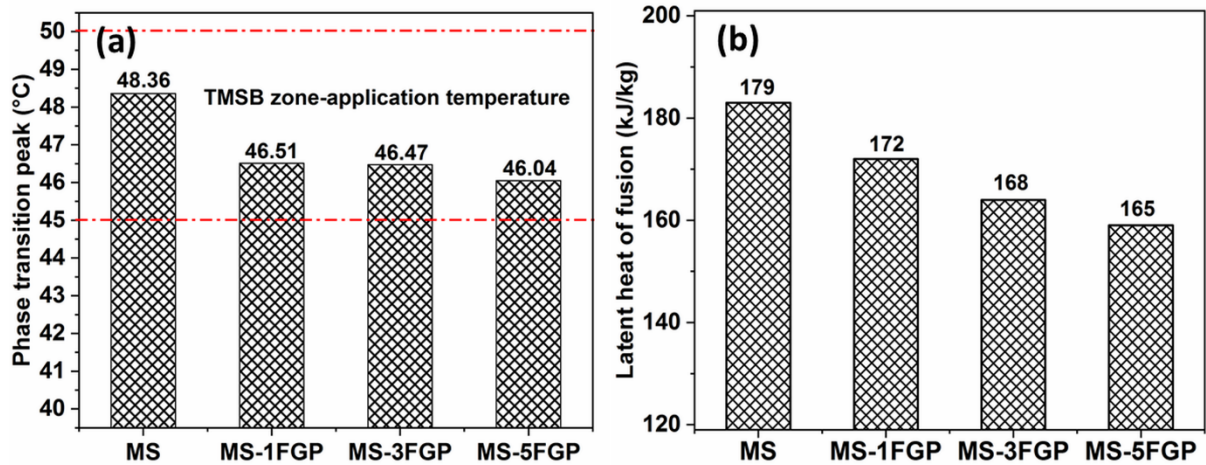


**Fig. 7.7** (a) Phase transition peak characteristics and (b) latent heat of fusion of MS-xFGP system.

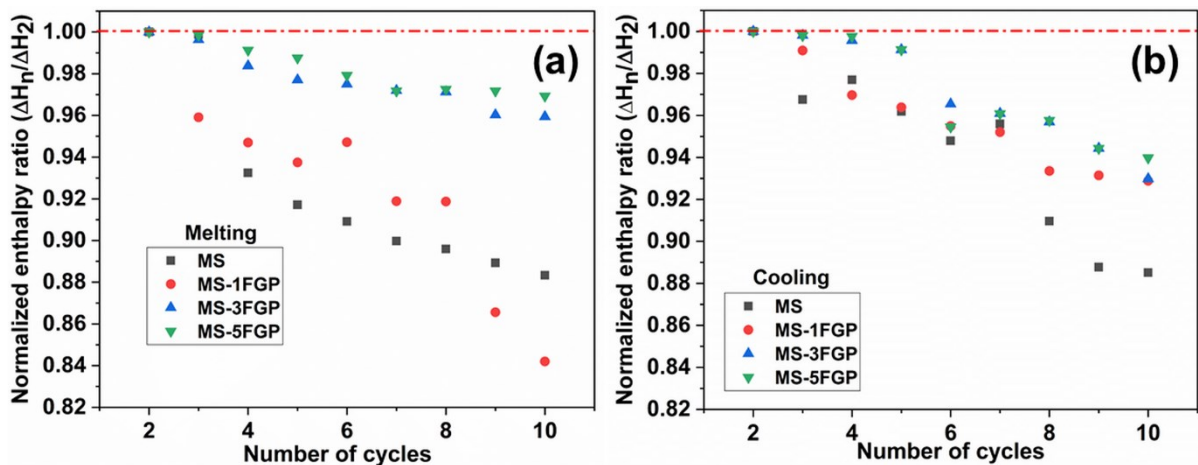


**Fig. 7.8** Normalized enthalpy ratio during (a) melting and (b) cooling.

Phase transition and energy storage (thermal) characteristics of FGP-loaded MS-based PCM composites was evaluated by the DSC technique at a slow ramp rate. The phase transition peak characteristics of MS-FGP was illustrated in **Fig.7.7a**. They exhibited a phase transition temperature peak of 48.36, 46.51, 46.47 and 46.04 °C for MS, MS-1FGP, MS-3FGP and MS-5FGP, respectively. It infers that by adding the FGP leads to a reduction in phase transition peak. On contrary, as-developed FGP-loaded myristic acid (pure) exhibited phase transition higher than 50 °C (relatively high) and considerable improvement in thermal conductivity (four fold). It

confirms that a eutectic can be made to tailor phase transition, which suits the EV application. The addition of thermally conductive fillers readily accelerates the thermal transport of the MS-FGP system to improve heat transfer that resulted in lowering the phase transition peak. The composites exhibited a phase transition peak in the range of 45-50 °C (TMSB zone within two dotted red lines) that perfectly suitable for the TMSB system, as indicated in **Fig.7.7a**. **Fig.7.7b** shows the latent heat of fusion (after 10 cycles) of the MS-FGP system with the influence of varying FGP content. The MS-FGP system presented latent heat of fusion (area under the DSC curve, after 10 cycles) of 179, 172, 168 and 165 kJ/kg for MS, MS-1FGP, MS-3FGP, and MS-5FGP, respectively. Importantly, the addition of FGP decreased the latent heat of fusion, as it does not get into phase transition or melting. The 5 wt.% of FGP contributed to the loss of latent heat of fusion by 8 % (after 10 cycles).

The value obtained in the first cycle was neglected, as it possesses tremendous thermal strain. By considering the latent heat of fusion in the second cycle ( $\Delta H_2$ ) as the base, a normalized enthalpy ratio ( $\Delta H_n/\Delta H_2$ ) was calculated. The normalized enthalpy ratio for 10 cycles during melting and cooling was illustrated in **Fig.7.8 (a & b)**. It infers that higher FGP loading exhibited a lower normalized enthalpy ratio than lower FGP loading for the same thermal cycles. It is ascribed to enhanced thermal transport with higher FGP content. Upon increasing thermal cycles, the normalized enthalpy ratio slightly reduced is an indication for thermal degradation in energy storage. With the increase in thermal cycles, the slope's increase confirms the loss in thermal energy storage capacity.

#### 7.4 Conclusion

M and S based eutectic PCM with suitable phase transition for TMSB was established. Severe alteration in thermal transport is noticed with the varied structural degree, and most crystalline material favours ballistic transport, resulting in increased thermal conductivity. Overall, the MS system's figure-of merit based on thermal conductivity follows the tendency; MS-FGP>MS-NTC>MS-DGO. The significant increase in thermal conductivity (597 %) and appropriate phase transition peak (46.04 °C) were achieved with 5 wt.% FGP loading, which could find a suitable way for TMSB applied in electric vehicles.

**Table 7.1:** A comparison of increase in thermal conductivity of carbon-loaded various PCMs

<b>Material</b>	<b>Melting point</b> (°C)	<b>Thermal conductivity</b>	<b>Ref.</b>
			<b>increase (%)</b>
EG+75% RT-50	50.0	576.0	47
MWCNTs+ 75 % RT-50	50.0	224.0	47
Paraffin/GNP	57.9	116.1	48
Palmitic acid/N-doped graphene	66.5	517.8	49
Paraffin/xGNP	54.9	805.6	50
Paraffin wax/CNF	50.0	40.6	51
Octadecanoic acid/graphene aerogel	57.0	1332.0	52
Lauric acid/ activated carbon	44.0	12.5	53
Paraffin/Cu <sub>2</sub> O-Cu-MWCNTs	52.3	17.2	54
Palmitic/stearic acid-CNTs	53.5	29.7	55
PEG6000/SiO <sub>2</sub> /CNTs	53.3	51.3	56
Myristic/stearic acid-NPC	46.8	117.6	57
Myristic/stearic acid-FGP	46.0	597	This work

## 7.5 References

1. D.A. Lashof, D.R. Ahuja, Relative contributions of greenhouse gas emissions to global warming, *Nature* 344 (1990) 529-531.
2. S. Chu, A. Majumdar, Opportunities and challenges for a sustainable energy future, *Nature* 488 (2012) 294–303.
3. D.G. Nocera, Living healthy on a dying planet, *Chem. Soc. Rev.* 38 (2009) 13-15.
4. S. Amjad, S. Neelakrishnan, R. Rudramoorthy, Review of design considerations and technological challenges for successful development and deployment of plug-in hybrid electric vehicles, *Renew. Sustain. Energy Rev.* 14 (2010) 1104-1110.
5. M. Wada, Research and development of electric vehicles for clean transportation, *J. Environ. Sci.* 21 (2009) 745-749.
6. S.J. Skerlos, J.J. Winebrake, Targeting plug-in hybrid electric vehicle policies to increase social benefits, *Energy Policy* 38 (2010) 705-708.
7. P. Baptista, M. Tomás, C. Silva. Plug-in hybrid fuel cell vehicles market penetration scenarios, *Int. J. Hydrogen Energy* 35 (2010) 10024-10030.
8. J. Dong, C. Liu, Z. Lin, Charging infrastructure planning for promoting battery electric vehicles: an activity-based approach using multiday travel data, *Transport. Res. Part C: Emerg. Technol.* 38 (2014) 44-55.
9. A. Barré, B. Deguilhem, S. Grolleau, M. Gérard, F. Suard, D. Riu, A review on lithium-ion battery ageing mechanisms and estimations for automotive applications, *J. Power Sources* 241 (2013) 680-689.
10. P. Ramadass, B. Haran, R. White, B.N. Popov, Capacity fade of Sony 18650 cells cycled at elevated temperatures: Part I. cycling performance, *J. Power Sources* 112 (2002) 606-613.
11. T.M. Bandhauer, S. Garimella, T.F. Fuller, A critical review of thermal issues in lithium-ion batteries, *J. Electrochem. Soc.* 158 (2011) R1-R25.
12. X.M. Xu, R. He, Review on the heat dissipation performance of battery pack with different structures and operation conditions, *Renew. Sustain. Energy Rev.* 29 (2014) 301-315.
13. J. Jaguemont, N. Omar, P.V. Bossche, J. Mierlo, Phase-change materials (PCM) for automotive applications: A review, *Appl. Therm. Eng.* 132 (2018) 308-320.

14. R. Zhao, S. Zhang, J. Liu, J. Gu, A review of thermal performance improving methods of lithium ion battery: electrode modification and thermal management system, *J. Power Sources* 299 (2015) 557-577.
15. M. Malik, I. Dincer, M.A. Rosen, Review on use of phase change materials in battery thermal management for electric and hybrid electric vehicles, *Int. J. Energy Res.* (2016) 1011-1031.
16. X. Feng, M.Ouyang, X.Liu, L. Lu, Y.Xia, X.He, Thermal runaway mechanism of lithium ion battery for electric vehicles: A review, *Energy Storage Mater.* 10 (2018) 246-267.
17. J. Jaguemont, L. Boulon, Y. Dubé, A comprehensive review of lithium-ion batteries used in hybrid and electric vehicles at cold temperatures, *Appl. Energy* 164 (2016) 99-114.
18. Q. Wang, B. Jiang, B. Li, Y. Yan, A critical review of thermal management models and solutions of lithium-ion batteries for the development of pure electric vehicles, *Renew. Sustain. Energy Rev.* 64 (2016) 106-128.
19. N.R. Jankowski, F.P. McCluskey, A review of phase change materials for vehicle component thermal buffering, *Appl. Energy* 113 (2014) 1525-1561.
20. I. Dincer, H.S. Hamut, J. Nader, *Thermal management of electric vehicle battery systems*, Wiley Edition, 2017.
21. P. Lyu, X. Liu, J. Qu, J. Zhao, Y. Huo, Z. Qu, Z. Rao, Recent advances of thermal safety of lithium ion battery for energy storage, *Energy Storage Mater.* 31 (2020) 195-220.
22. D. Chen, J. Jiang, G.H. Kim, C. Yang, A. Pesaran, Comparison of different cooling methods for lithium ion battery cells, *Appl. Therm. Eng.* 94 (2016) 846-854.
23. G. Xu, L. Huang, C. Lu, X. Zhou, G. Cui, Revealing the multilevel thermal safety of lithium batteries, *Energy Storage Mater.* 31 (2020) 72-86.
24. J. Jaguemont, N. Omar, P.V. Bossche, J. Mierlo, Phase-change materials (PCM) for automotive applications: A review, *Appl. Therm. Eng.* 132 (2018) 308-320.
25. M. Malik, I. Dincer, M.A. Rosen, Review on use of phase change materials in battery thermal management for electric and hybrid electric vehicles, *Int. J. Energy Res.* (2016) 1011-1031.
26. N.R. Jankowski, F.P. McCluskey, A review of phase change materials for vehicle component thermal buffering, *Appl. Energy* 113 (2014) 1525-1561.
27. L. Fan, J.M. Khodadadi. Thermal conductivity enhancement of phase change materials for thermal energy storage: A review, *Renew. Sustain. Energy Rev.* 15 (2011) 24-46.

28. G. Yang, Y. Yim, J. Lee, Y. J. Heo, S. J. Park, Carbon-filled organic phase-change materials for thermal energy storage: a review, *Molecules* 24 (2019) 2055 (17pp).
29. Y. Lin, Y. Jia, G. Alva, G. Fang. Review on thermal conductivity enhancement, thermal properties and applications of phase change materials in thermal energy storage, *Renew, Sustain. Energy Rev.* 82 (2018) 2730-2742.
30. S. Wu, T. Yan, Z. Kuai, W. Pan, Thermal conductivity enhancement on phase change materials for thermal energy storage: A review, *Energy Storage Mater.* 25 (2020) 251-295.
31. X. Cai, Y. Luo, B. Liu, H.M. Cheng, Preparation of 2D material dispersions and their applications, *Chem. Soc. Rev.* 47 (2018) 6224-6266.
32. Z. Ling, J. Chen, T. Xu, X. Fang, X. Gao, Z. Zhang, Thermal conductivity of an organic phase change material/expanded graphite composite across the phase change temperature range and a novel thermal conductivity model, *Energy Convers. Manag.* 102 (2015) 202-208.
33. F. Tang, D. Su, Y. Tang, G. Fang, Synthesis and thermal properties of fatty acid eutectics and diatomite composites as shape-stabilized phase change materials with enhanced thermal conductivity, *Sol. Energy Mater. Sol. Cells* 141 (2015) 218-224.
34. T. Nomura, K. Tabuchi, C. Zhu, N. Sheng, S. Wang, T. Akiyama, High thermal conductivity phase change composite with percolating carbon fiber network, *Appl. Energy* 154 (2015) 678-685.
35. B. Tian, W. Yang, L. Luo, J. Wang, K. Zhang, J. Fan, J. Wu, T. Xing, Synergistic enhancement of thermal conductivity for expanded graphite and carbon fiber in paraffin/EVA form-stable phase change materials, *Sol. Energy* 127 (2016) 48-55.
36. M. Amin, N. Putra, E.A. Kosasih, E. Prawiro, R. A. Luanto, T.M.I. Mahlia, Thermal properties of beeswax/graphene phase change material as energy storage for building applications. *Appl. Therm. Eng.* 112 (2017) 273-280.
37. S. Arora, Selection of thermal management system for modular battery packs of electric vehicles: A review of existing and emerging technologies, *J. Power Sources* 400 (2018) 621-640.
38. P. Singh, R.K. Sharma, A.K. Ansul, R. Goyal, A. Sarı, V.V. Tyagi, A comprehensive review on development of eutectic organic phase change materials and their composites for low and medium range thermal energy storage applications, *Sol. Energy Mater. Sol. Cells* 223 (2021) 110955 (25pp).

39. H. Ke, Phase diagrams, eutectic mass ratios and thermal energy storage properties of multiple fatty acid eutectics as novel solid-liquid phase change materials for storage and retrieval of thermal energy, *Appl. Therm. Eng.* 113 (2017) 1319-1331.
40. S. Kahwaji, M.A. White, Prediction of the properties of eutectic fatty acid phase change materials, *Thermochim. Acta* 660 (2018) 94-100.
41. B. Padya, N. Ravikiran, R. Kali, N. Narasaiah, P.K. Jain, High thermal energy storage and thermal conductivity of few-layer graphene platelets loaded phase change materials: A thermally conductive additive for thermal energy harvesting, *Energy Storage* 2 (6) (2020) 199 (8pp).
42. B. Padya, K. V. P. Prabhakar, P. K. Jain, Synthesis of vertically aligned carbon nanotube arrays by injection method in CVD, *J. Nanosci. Nanotechnol.* 10 (2010) 4960-4966.
43. B. Padya, D. Kalita, P. K. Jain, G. Padmanabham, M. Ravi, K. S. Bhat, Self-organized growth of bamboo-like carbon nanotube arrays for field emission properties, *Appl. Nanosci.* 2 (2012) 253-259.
44. J.W.Jang, C.E. Lee, S.C. Lyu, T.J. Lee, C.J. Lee, Structural study of nitrogen doping effects in bamboo shaped multiwalled carbon nanotubes, *Appl. Phys. Lett.* 84(15) (2004) 2877-2879.
45. K. Angoni, Remarks on the structure of carbon materials on the basis of Raman spectra, *Carbon* 31(4) (1993) 537-547.
46. M. Asheghi, K. Kurabayashi, R. Kasnavi, K.E. Goodson, Thermal conduction in doped single-crystal silicon films, *J. Appl. Phys.* 91 (2002) 5079-5088.
47. P. M. Gilart, A. Y. Martí'nez, M. G. Barriuso, C. M. Martí'nez, Development of PCM/carbon-based composite materials, *Sol. Energy Mater. Sol. Cells* 107 (2012) 205-211.
48. L.W.Fan, X.Fang, X.Wang, Y. Zeng, Y.Q.Xiao, Z.T. Yu, X. Xu, Y.C. Hu, K.F. Cen, Effects of various carbon nanofillers on the thermal conductivity and energy storage properties of paraffin-based nanocomposite phase change materials, *Appl. Energy* 110 (2013) 163-172.
49. Y. Li, Y.A. Samad, K. Polychronopoulou, S.M. Alhassan, K. Liao, From biomass to high performance solar-thermal and electric-thermal energy conversion and storage materials, *J. Mater. Chem. A* 2 (2014) 7759-7765.

50. J. Xiang, L. T. Drzal, Investigation of exfoliated graphite nanoplatelets (xGnP) in improving thermal conductivity of paraffin wax-based phase change material, *Sol. Energy Mater. Sol. Cells* 95 (2011)1811-1818.
51. Y. Cui, C. Liu, S. Hu, X. Yu, The experimental exploration of carbon nanofiber and carbon nanotube additives on thermal behavior of phase change materials, *Sol. Energy Mater. Sol. Cells* 95 (2011) 1208-1212.
52. S. Zhang, S. Wang, J. Zhang, Y. Jiang, Q. Ji, Z. Zhang, Z. Wang, Increasing phase change latent heat of stearic acid via nanocapsule interface confinement, *J. Phys. Chem. C* 117 (2013) 23412-23417.
53. Z. Chen, F. Shan, L. Cao, G. Fang, Synthesis and thermal properties of shape stabilized lauric acid/activated carbon composites as phase change materials for thermal energy storage, *Sol. Energy Mater. Sol. Cells* 102 (2012) 131-136.
54. B. Xu, B. Wang, C. Zhang, J. Zhou, Synthesis and light-heat conversion performance of hybrid particles decorated MWCNTs/paraffin phase change materials, *Thermochim. Acta* 652 (2017) 77-84.
55. N. Zhang, Y. Yuan, Y. Yuan, X. Cao, X. Yang, Effect of carbon nanotubes on the thermal behavior of palmitic-stearic acid eutectic mixtures as phase change materials for energy storage, *Sol. Energy* 110 (2014) 64-70.
56. B. Tang, H. Wei, D. Zhao, S. Zhang, Light-heat conversion and thermal conductivity enhancement of PEG/SiO<sub>2</sub> composite PCM by in situ Ti<sub>4</sub>O<sub>7</sub> doping, *Sol. Energy Mater. Sol. Cells* 161 (2017) 183-189.
57. D. G. Atinifu, W. Dong, X. Huang, H. Gao, G. Wang, Introduction of organic-organic eutectic PCM in mesoporous N-doped carbons for enhanced thermal conductivity and energy storage capacity, *Appl. Energy* 211 (2018) 1203-1215.

## CHAPTER-8

---

### Conclusion and Scope for Future works

---

This study exclusively emphasized on advancing material technology to develop functional nanocomposite materials to improve the thermal and capacitive energy storage characteristics of high-performance energy storage devices which are applied in automotive sector.

#### 8.1 Conclusions

The following conclusions were drawn from this study:

- A facile process was demonstrated for scalable preparation of FGP via solution-phase exfoliation of expanded graphite, for which a solvent with minimum enthalpy of mixing is desirable. Intensifying process parameters (800, 850 and 900 °C) for NTC synthesis was carried out. Based on N-content and yield, NTC-850 found to be optimum. DGO was prepared at 120, 150, 180 and 210 °C for 5 h via temperature-assisted de-oxygenation technique. Based on the extent of de-oxygenation (C/O ratio), the DGO-210 (processed at 210 °C) found to be optimum.
- PNCG, PNCT, PNCD and YP-50 exhibited a specific capacitance of 188, 147, 121, and 114 F/g (at 0.5 A/g) and capacity retention of 96.82, 93.26, 90.50 and 96.43 % (for 1000 cycles), respectively. PNCG//PNCG (FGP loaded) exhibited a maximum energy density of 28.17 Wh/kg with the maximum power density of 4160 W/kg, superior to commercially applied YP-50 ( 16.32 Wh/kg and 2977 W/kg) using compressed expanded graphite foil based current collector. Considering the contribution from all the physicochemical aspects and electrochemical properties of the porous carbon for carbon/carbon symmetric supercapacitor was found in the order: PNCG >PNCT>YP-50>PNCD.
- aNGNS (activated FGP) based symmetric supercapacitor demonstrated excellent specific capacitance of 242 F/g at the current density of 0.5 A/g with a capacity retention of 97.21 % after 1000 cycles. The device shown remarkable energy density of 27.22 Wh/kg at a power density of 230.56 W/kg at constant current density of 0.5 A/g.
- A high-performance cathode material for Li-ion asymmetric supercapacitor (1M LiPF<sub>6</sub> and graphite foil) was prepared through a facile strategy by integrating the conductive FGP with polymer-derived N-doped carbon. PNCG presented a capacity of 188.8, 172.9, 156.9 and 135.4 mAh/g at the discharge current density of 0.2, 0.5, 1.0 and 2.0 A/g,

respectively. Furthermore, it presented a discharge capacity of 147.9 mAh/g after 500 cycles at a current density of 1.0 A/g with retention of 94.2 % capacity demonstrating exceptional cycle stability.

- Severe alteration in thermal transport is noticed with the varied structural degree of nanocarbon, and most crystalline material favours ballistic transport, resulting in increased thermal conductivity. Overall, the MS system's figure-of-merit based on thermal conductivity follows the tendency: MS-FGP>MS-NTC>MS-DGO. The significant increase in thermal conductivity (597 %) and appropriate phase transition peak (46.04 °C) were achieved with 5 wt.% FGP loading, which could find a suitable way for TMSB applied in electric vehicles. Whereas as-developed FGP-myristic acid based PCM exhibited phase transition higher than 50 °C, which hinder its application in TMSB. Thus, a eutectic with tailored phase transition (45-50 °C) is rightly applicable for thermal management.

## 8.2 Scope for further research

Although this study has successfully achieved superior properties in intensifying process parameters for scalability of nanocarbon materials and their hybrids for capacitive and thermal energy storage, a few areas were sprouted during the present study, which needs further investigation as suggested below:

- Generating a set of co-solvents for scalable preparation of graphene via high-shear mixer adapting a strategy of minimum enthalpy of mixing
- Preparation of nanomaterials-loaded porous carbon with high electrical conductivity, suitable porosity and pore-size distribution for capacitive energy.
- Preparation of expanded graphite-based shape-stabilized phase change materials with nanomaterials inclusion with excellent thermal transport and thermal energy storage
- Generating a set of eutectic PCM system with phase transition temperature suitable for thermal management system-battery adapting artificial intelligence techniques

## List of Publications (Journals and conferences)

This PhD thesis is based on the following journal publications.

### Contribution to Journal Publication

1. **Balaji Padya**, N. Narasaiah, P.K. Jain, T.N. Rao, A facile co-solvent strategy for preparation of graphene nanoplatelet powder: An industrially viable innovative approach, *Ceramics International* 45 (2019) 13409-13413. **(IF=4.52)**
2. **Balaji Padya**, Ravi Kali, P.K. Enaganti, N. Narasaiah, P.K. Jain, Facile synthesis and frequency-response behavior of supercapacitor electrode based on surface-etched nanoscaled-graphene platelets, *Colloids and Surfaces A* 609 (2021) 125587 (8pp) **(IF=4.54)**
3. **Balaji Padya**, N. Ravikiran, Ravi Kali, N. Narasaiah, P. K. Jain, High thermal energy storage and thermal conductivity of few-layer graphene platelets loaded phase change materials: A thermally conductive additive for thermal energy harvesting, *Energy Storage* 2 (6) (2020) 199 (8pp). **(IF=6.2)**
4. **Balaji Padya**, N. Ravikiran, Ravi Kali, N. Narasaiah, P.K. Jain, T.N. Rao, Multifunctional surface-modified ultrathin graphene flakes for thermal and electrochemical energy storage application, *Materials Today: Proceedings* 26 (2020) 52-57. **(IF=1.24)**
5. **Balaji Padya**, Ravi Kali, N. Ravikiran, N. Narasaiah, P.K. Jain, Constructing graphene-coupled nitrogen-doped carbon-based all-carbon hybrid for hybrid Li-ion supercapbattery: An investigation and insight into “charge-averaged” charge/discharge voltage analysis, *Journal of Alloys and Compounds* 872 (2021) 159660 (9pp). **(IF=5.32)**
6. **Balaji Padya**, Akshay, N. Ravikiran, Ravi Kali, B. Bollareddy, N. Narasaiah, P.K. Jain, Constructing nanocarbon-loaded precisely phase transition-tuned energy composite eutectics with enhanced thermal conductivity: Nanocarbon’s crystallinity-dependent thermal transport, *Materials Today Communication* (communicated) **(IF=3.3)**.
7. **Balaji Padya**, Ravi Kali, N. Ravikiran, N. Narasaiah, P.K. Jain, Preparation and electrochemical capacitive properties of multidimensional (1-D and 2-D) nanocarbon-hybridized nitrogen-containing porous carbon for carbon/carbon supercapacitor: Nanocarbon-aided capacitance boosting, *Colloids and Surfaces A* 627 (2021) 127225 **(IF=4.54)**

## **Journal publication not included in Thesis**

1. **Balaji Padya**, P.K. Enaganti, Ravi Kali, N. Ravikiran, N. Narasaiah, P.K. Jain, A controlled process of atomic-scale material design via temperature-mediated grain refinement of  $\text{NiCo}_2\text{O}_4$  rods for capacitive energy storage, *Journal of Science: Advanced Materials and Devices* 5 (2020) 173-179. (IF=5.46)

## **Contribution to Conference Publications**

1. **Balaji Padya**, N. Ravikiran, Ravi Kali, N. Narasaiah, P.K. Jain, T.N. Rao, Preparation of multifunctional graphene flakes via solution-phase exfoliation through wet-milling for energy storage application, Attended Int. Conf. on NanoScience and Engineering Applications (ICONSEA-2018) held during October 4-6, 2018 at Hyderabad.
2. **Balaji Padya**, E. Prashant Kumar, Ravi Kali, N. Ravikiran, N. Narasaiah, P.K. Jain, T.N. Rao, Insights into processing, and influence of calcination temperature on pseudocapacitance properties of 1-D spinel- $\text{NiCo}_2\text{O}_4$  rods, Int. Conf. on Advanced Functional Materials and Devices (ICAFMD-2019) held during February 26-28, 2019 at Warangal.
3. **Balaji Padya**, Ravi Kali, N. Narasaiah, P.K. Jain, T.N. Rao, A novel functionally-graded nitrogen-enriched carbon uniformly-coated on graphene based all-carbon hybrid for energy storage devices, Int. Conf. on Advanced Materials and Processes for Defence applications (ADMAT-2019) held during Sept.23-25, 2019 at Hyderabad.
4. **Balaji Padya**, Ravi Kali, N. Narasaiah, P.K. Jain, Platelet-like structured 2-D Carbon: solution-phase preparation and application for thermal and electrochemical energy storage, Int. Conf. on Advances in Minerals, Metals, Materials, Mfg. and Modelling (ICAM<sup>5</sup>) held during Sept.25-27, 2019 at Warangal.

## **CURRICULUM VITAE**

**1. Name** : Balaji Padya

**2. Date of Birth** : 23-01-1983

**3. Educational Qualification:**

B.Tech : Kakatiya University, Warangal

Specialization: Mechanical Engineering

Ph.D : Pursuing, National Institute of Technology, Warangal

**4. Research Interest** : Nanocarbon Technology, Porous carbon, Energy storage, Composites, Field emission, Nanolubrication

**5. Professional Experience** : 15 years (Research and Development)

**6. Present Position** : Senior Scientist,  
ARCI, Hyderabad-500005, INDIA

**7. Contact Address** : ARCI, RCI road, Balapur Post,  
Hyderabad-500005, INDIA

**Email** : balajipadya@gmail.com/balaji@arci.res.in

**Contact Number** : 040-24452438/9908898925